Fabrication and Characterization of Carbon Nanotube and Graphene Field-Effect Transistors

（カーボンナノチューブおよびグラフェン

電界効果トランジスタの制作と評価）

金　成眞

This thesis entitled "Fabrication and Characterization of Carbon Nanotube and Graphene Field-Effect Transistors," submitted by Sungjin Kim, is approved by the undersigned members of this committee:

Shigeo Maruyama, Professor
Thesis Advisor and Committee Chair
Department of Mechanical Engineering
The University of Tokyo

Jean-Jacques Delaunay, Associate Professor
Department of Mechanical Engineering
The University of Tokyo

Junichiro Shiomi, Associate Professor
Department of Mechanical Engineering
The University of Tokyo

Kosuke Nagashio, Associate Professor
Department of Material Engineering
The University of Tokyo

Shohei Chiashi, Lecturer
Department of Mechanical Engineering
The University of Tokyo

To my family.

Contents

List of Figures vii

List of Tables xii

Chapter 1 Introduction

1.1 Types of carbon materials 1

1.2 Properties of Graphene and SWNTs 3

1.2.1 Electronic band structure of graphene 4

1.2.2 Band structure of SWNT 9

1.2.3 Indexing of SWNTs 14

1.3 Characterization of Graphene and SWNT 15

1.3.1 Resonance Raman Spectroscopy 15

1.3.2 Kataura plots 17

1.4 Nanocarbon-based field-effect transistors (FETs) 17

1.4.1 Single-walled carbon nanotube FETs 18

1.4.2 Graphene-based field-effect transistors 20

1.5 Doping strategy for SWNT and graphene devices 22

1.5.1 Doping of SWNT-based field-effect transistors 23

1.5.2 Doping of Graphene-based field-effect transistors 27

1.6 Challenges of SWNTs and Graphene technology 39

1.7 Objective and organization of this thesis 41

Chapter 2 Highly stable n-doped graphene field-effect transistors with

polyvinyl alcohol films

2.1 Background and motivation 44

2.2 Experimental 46

2.1.1 Growth and Fabrication of graphene FETs 46

2.2.2 Electrode array formation 48

2.2.3 Characterization of graphene field-effect transistors 49

2.3 Result and discussion 49

2.3.1Properties of as-grown CVD graphene 49

2.4 Polymer-coated graphene devices 53

2.4.1 Fabrication of PVA-coated graphene FET 53

2.4.2 Transfer characteristics of PVA-doped graphene FETs 54

2.4.3 Temperature effect of PVA-doped graphene FETs 56

2.4.4 Electron-donating ability of PVA for GFET 58

2.4.5 Charge transfer evidence between PVA and graphene 59

2.4.6 Mobility before and after PVA doping of GFETs 61

2.4.7 Stability for PVA-coated graphene devices 62

2.5 Conclusion and originality of this chapter 65

Chapter 3 Transport characteristics of nitrogen-doped horizontally aligned SWNTs (N-HASWNTs)

3.1 Background and Motivation 69

3.2 Experiments 71

3.2.1 Growth of nitrogen-induced HASWNTs 71

3.2.2 Transfer process 72

3.2.3 Fabrication of N-HASWNT field-effect transistors 74
3.2.4 Characterization of N-HASWNT FETs 75
3.3 Result and discussion 76
3.3.1 HASWNTs and N-HASNWTs growth on quartz substrates 76
3.3.2 I-V characteristics (I_{ds}-V_{gs}) of HASWNT devices 85
3.3.3 I-V characteristics (I_{ds}-V_{gs}) of N-HASWNT devices 88
3.3.4 Transfer curves of N-HASWNT device after e-annealing 89
3.3.5 Threshold voltage shift as a function of acetonitrile ratio 90
3.3.6 Nitrogen configuration of N-HASWNT by EELS 91
3.3.7 HRTEM images of HASWNTs 95
3.3.8 Mobility vs on/off ratio of N-HASWNT transistors 98
3.3.9 Band diagram of N-HASWNT 99
3.4 Conclusion and originality of this chapter 99

Chapter4 Closing remarks
4.1 Summaries of this thesis 102
4.2 Future work of this thesis 103

References 105

Acknowledgement 121

Publication list in PhD course 124

List of Figures

1.1 Crystal structures of various carbon allotropes 2

1.2 The band structure of graphene 3

1.3 Energy dispersion of graphene 7

1.4 Surface and contour plot of the energy dispersion in graphene 8

1.5 Energy dispersion of graphene by first principle and tight-binding method 9

1.6 Representation of a SWNT by a chiral vector 10

1.7 Brillouin zone of graphene with conic energy dispersions 12

1.8 Indexing of SWNTs 14

1.9 Raman spectra from different type of sp^2 nanocarbons 15

1.10 Schematic of Raman scattering process 16

1.11 Kataura plots for SWNTs 17

1.12 Schematic of electrical transport measurements of SWNTs 18

1.13 Drain current (I_{ds}) as a function of the gate voltage (V_{gs}) 19

1.14 Schematic of back- and top-gated graphene FETs 22

1.15 Chemical doping of SWNTs 23

1.16 Non-chemical doping of SWNT 26

1.17 Device schematic and measured sensor responses 28

1.18 Carrier mobility versus dielectric constant 31

1.19 Atomic structure of graphene annealed in NH_3 33

1.20 Schematic of layer-doped graphene 34

1.21 Dirac point shift of doped graphene 36

1.22 Schematic of a graphene p-n junction and its transfer curve 38

2.1 Schematic diagram of ACCVD 46

2.2 Experimental procedures of as-grown FET 47

2.3 Optical microscope images of device array 48

2.4 Process steps for graphene FET fabrication 48

2.5 Schematic diagram of GFET measurement 49

2.6 SEM, scanning Raman spectroscopy of monolayer graphene 50

2.7 Raman spectra and SEM image for as-grown LPCVD graphene 51

2.8 Corresponding transfer characteristics of as-grown graphene 53

2.9 Process step for PVA-coated GFET 54

2.10 Electronic transport properties of GFET before/after 10 wt% PVA 55

2.11 Schematic illustration of carrier migration between PVA film and graphene 56

2.12 I-V characteristics of 10 wt% PVA-doped GFET as temperature 57

2.13 Transfer curves as a function of temperature and curing time 58

2.14 Transfer curves before and after 1 wt% PVA coating 59

2.15 Transfer curves before and after 20 wt% PVA coating 60

2.16 Raman spectra of graphene as a function of PVA consistency 61

2.17 Comparison of mobilities before and after 10 wt% PVA-doped GFETs 62

2.18 Drain current and transconductance as a function of gate voltage & hole and electron mobility as a function of channel width 63

2.19 Doping stability as a function of doping level with PVA 64

3.1 Growth procedures of horizontally aligned SWNTs 71

3.2 Optical images of the catalyst on a quartz 72

3.3 Transfer process and SEM images before/after transfer HASWNTs 73

3.4 Optical images of patterned SiO_2/Si and PET 74

3.5 Fabrication illustration for HASWNT FET 75

3.6 SEM images of ethanol-based HASWNTs by ACCVD 76

3.7 SEM images of HASWNTs by various nitrogen concentration 77

3.8 Raman spectra at various excitation energies of HASWNT and N-HASWNT on a quartz substrate 78

3.9 Raman spectra at various excitation energies of HASWNT and N-HASWNT on a SiO_2/Si substrate 80

3.10 Kataura plot with incident laser energies 81

3.11 G band peak shift with various acetonitrile contents 82

3.12 G band peak shift with nitrogen source flow rate 83

3.13 Intensity ratio of D band to G band as acetonitrile concentration increases 84

3.14 Typical electrical properties of HASWNT FET under air and vacuum condition & the possible origin of hysteresis of charge 85

3.15 Corresponding transfer curves in terms of HASWNT and N-HASWT FET in ambient air condition 86

3.16 Corresponding transfer curves in terms of HASWNT and N-HASWT FET in rough vacuum condition 87

3.17 Corresponding I_d-I_g characteristics of HASWNT FET before and after thermal annealing 89

3.18 Corresponding I_d-I_g characteristics of HASWNT FET before and after electrical

annealing in vacuum condition 90

3.19 Threshold voltage (V_{th}) shift as a function of nitrogen-induced various acetonitrile concentrations ratio in air and vacuum 91

3.20 V_{th} shift as a function of number of electrical annealing 92

3.21 Electron energy loss spectrum of HASWNT and N-HASWNT 93

3.22 HRTEM images of HASWNTs 94

3.23 HRTEM images of 50% N-HASWNTs 95

3.24 Diameter distribution between pristine and N-induced HASWNTs 96

3.25 I-V curves, on/off versus mobility, and statistical on/off result 97

3.26 Performance of HASWNT and N-HSWNT FETs 98

3.27 Electrical properties of 20 % N-HASWNT devices 99

List of Tables

1.1 Work function of various metal electrodes for CNTFET 24

1.2 Major challenges for device/circuit fabrication with SWNT 40

3.1 Comparison of growth conditions between pristine and nitrogen-based SWNTs 71

Chapter 1

Introduction

1.1 Types of carbon materials

Carbon is the fourth most abundant chemical element in the universe by mass after hydrogen, helium, and oxygen. It is a member of group 14 on the periodic table. It has six protons and neutrons inside nucleus and two electrons revolving around nucleus in the 1s orbital whereas four other electron rotating in the next energetic orbital (2s, 2p). Atomic carbon is a very short-lived species and, therefore carbon is stabilized in various multi-atomic structures with different molecular configurations as allotropes.[1] Carbon has a wide range of allotropes in different dimensions. At zero-dimension (0D) it forms fullerene was discovered by H.W. Kroto, J.R. Heath, S.C. O`Brien, R.F. curl, and Richard Smalley in 1985.[2] The fullerene is a fairly large molecule that consists of sixty carbon atoms completely bonded with icosahedron symmetry to form a sphere.[3] The fullerene molecule is a fundamental building block of the crystalline phase, and through doping and chemical reactions it forms a large family of materials, many of which have special, intriguing properties.[1,3]

In 1D structures, carbon atoms arrange themselves as single-walled carbon nanotubes

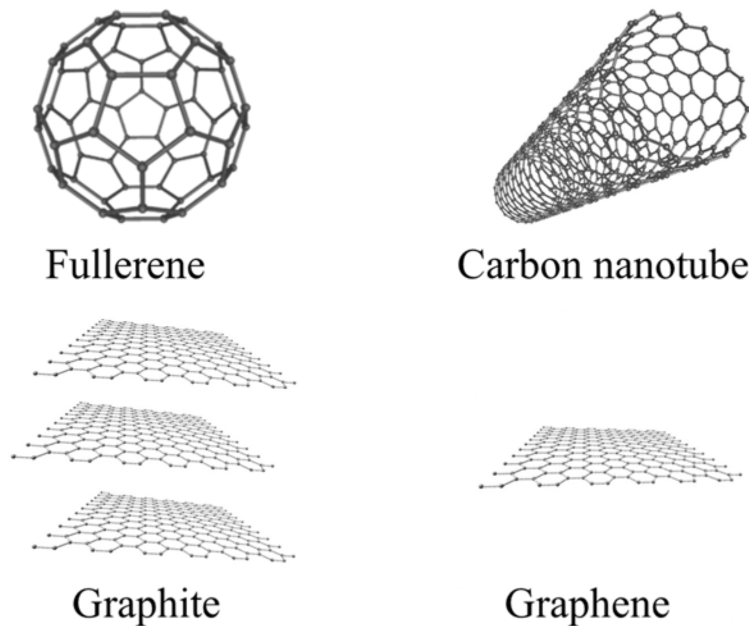

Figure 1.1. Crystal structures of various carbon allotropes. The carbon atoms form 0D fullerene (top left), 1D CNT (top right), 2D graphene (bottom right), and 3D graphite structures. The figure is reproduced from en.wikipedia.org.

(SWNTs), which consist of a piece of graphene sheet wrapped into a cylinder with a nanometer-size diameter.[4,5] Because of their very small diameters and relatively long lengths, SWNTs are prototype hollow cylindrical 1D quantum wires, is shown in Figure 1.1. Experimental observation proved that SWNTs are cylindrical forms of rolled graphene and are not spirally scrolled graphene sheet.[6] Depending on the atomic orientations along the tube axis, the carbon nanotube (CNT) shows unique electrical and mechanical properties. Carbon atoms also form a flat monolayer of atomic carbon, tightly packed in a 2D honeycomb lattice,[7] called graphene, was discovered by Andre Geim and Konstantin Novoselov. Graphene is an ideal building block to study the fundamentals of carbon structures. In three-dimensions (3D), carbon forms as graphite, diamond, and amorphous

carbon. Graphite consists of stacks of graphene layers that are weakly coupled by van der Waals forces.[1] The amorphous form is an assortment of carbon atoms in a non-crystalline, irregular manner, which essentially graphite but not held in a crystalline macrostructure. Depending on the atomic arrangements of 3D carbon atom, it forms mechanically weak, optically opaque, highly electrically conductive graphite as well as mechanically strong, optically transparent, insulating diamond. Carbon nanofoams, glassy carbons, and linear acetylenic carbon are the other forms of known 3D carbon allotropes.

1.2 Properties of Graphene and SWNTs

The electronic band structures of SWNTs along with their small size and low dimension are responsible for their unique electrical transport properties. The electronic band structures of

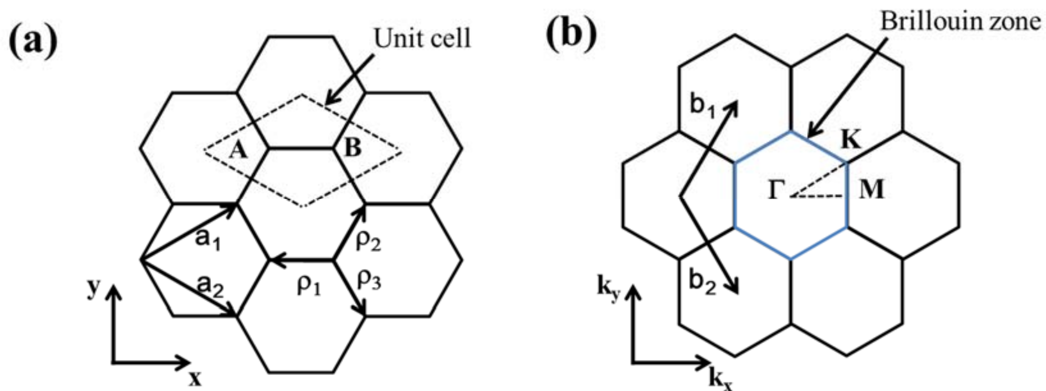

Figure 1.2. The band structure of graphene. (a) Real space representation of a graphene lattice. A unit cell is shown as a dashed rhombus with two carbon atoms (A and B). Unit vectors, $\mathbf{a_1}$ and $\mathbf{a_2}$, with length “a” are shown. Vectors ρ_j connect nearest neighbor carbon atoms. (b) Reciprocal (momentum) space representation of a graphene lattice with two unit vectors $\mathbf{b_1}$ and $\mathbf{b_2}$. High-symmetry point (Γ, K, M) in a Brillouin zone are also shown.[13]

one-dimensional SWNTs and the various electrical transport properties associated with them.

1.2.1 Electronic band structure of graphene

A SWNT cab be considered as a graphene sheet, rolled up to form a hollow cylinder. As we will see, understanding the band structure of graphene is essential for understating those of SWNTs. The lattice structure of graphene in real space consists of hexagonal arrangement of carbon atoms as shown in Figure 1.2(a). Isolated carbon atoms have four valence electrons in $2s$, $2p_x$, $2p_y$, and $2p_z$ atomic orbitals. As carbon atoms form graphene, three atomic orbitals, $2s$, $2p_x$, and $2p_y$, are hybridized into three sp^2 orbitals in the same plane while the $2p_z$ orbital remains perpendicular to other orbitals. The hybridized orbitals are responsible for σ bonds between the adjacent carbon atoms and the $2p_z$ orbital results in π bonds out of the plane of graphene. Generally, electrical transport properties are determined by the electrons (holes) near the Fermi level, since only these electrons (holes) have easy access to the unoccupied (occupied) states. Therefore, we only consider the band structure near the Fermi level. In graphene, the π orbitals, which lie near the Fermi level, are responsible for the electrical transport properties by forming delocalized states.

The band structure of graphene derived from p orbitals can be calculated by the tight-binding approximation.[8] Graphene has a unit cell with two nonequivalent carbon atoms, A and B (all other atoms can be translated back into either of the two by a suitable combination of two unit vectors, $\mathbf{a}_1$ and $\mathbf{a}_2$), as shown in Figure 1.2(a). The reciprocal lattice of graphene with unit vectors, b1 and b2, and high-symmetry points is shown in Figure 1.2(b).

In order to find the band structure of the graphene p orbitals, we need to find the solutions of the Schrödinger equation

$$H\Psi = E\Psi \tag{1.1}$$

where H is the Hamiltonian, Ψ is the total wave function, and E is the energy of electrons in the π orbitals of graphene. In a periodic system as in graphene, the total wave function can be constructed from a linear combination of Bloch functions u_i, which has a periodicity of the lattice. In the tight-binding approximation, u_i is represented by a linear combination of wave functions localized at each atom site, i.e., atomic wave function. Since only the π orbitals that originate from the $2p_z$ orbital of each carbon atom are considered, Bloch function u_i for each atom can be constructed from $2p_z$ orbitals of atoms A and B as

$$u_{\mathrm{A(B)}} = \frac{1}{\sqrt{N}} \sum_{\mathrm{A(B)}} \mathrm{e}^{\mathrm{i}\mathbf{k}\cdot\mathbf{r}_{\mathrm{A(B)}}} X(\mathbf{r} - \mathbf{r}_{\mathrm{A(B)}}) \tag{1.2}$$

where X(r) is the orbital $2p_z$ wave function for an isolated carbon atom. Then, Ψ in Eq. (1.1) can be written as follows:

$$\Psi = C_{\mathrm{A}}u_{\mathrm{A}} + C_{\mathrm{B}}u_{\mathrm{B}}. \tag{1.3}$$

By substituting Eq. (1.3) into (1.1), the Schrödinger equation can be solved in a matrix form as follows:

$$\begin{pmatrix} H_{\mathrm{AA}} & H_{\mathrm{AB}} \\ H_{\mathrm{BA}} & H_{\mathrm{BB}} \end{pmatrix} \begin{pmatrix} C_{\mathrm{A}} \\ C_{\mathrm{B}} \end{pmatrix} = E \begin{pmatrix} S_{\mathrm{AA}} & S_{\mathrm{AB}} \\ S_{\mathrm{BA}} & S_{\mathrm{BB}} \end{pmatrix} \begin{pmatrix} C_{\mathrm{A}} \\ C_{\mathrm{B}} \end{pmatrix} \tag{1.4}$$

Here,

$$H_{ij} = \langle u_i | H | u_j \rangle, S_{ij} = \langle u_i | u_j \rangle. \tag{1.5}$$

For simplicity, the overlap between $2p_z$ wave functions of different atoms are neglected, i.e., $S_{\mathrm{AB}} = S_{\mathrm{BA}} = 0$. We can also see that $S_{\mathrm{AA}} = S_{\mathrm{BB}} = 1$ (normalized), then Eq. (1.4) is simplified to

$$\begin{pmatrix} H_{\mathrm{AA}} - E & H_{\mathrm{AB}} \\ H_{\mathrm{BA}} & H_{\mathrm{BB}} - E \end{pmatrix} \begin{pmatrix} C_{\mathrm{A}} \\ C_{\mathrm{B}} \end{pmatrix} = \begin{pmatrix} 0 \\ 0 \end{pmatrix}. \tag{1.6}$$

This matrix equation has a nontrivial solution only when

$$\begin{vmatrix} H_{AA} - E & H_{AB} \\ H_{BA} & H_{BB} - E \end{vmatrix} = 0. \tag{1.7}$$

Further, we can see that $H_{AA} = H_{BB}$ by symmetry of the graphene lattice (atoms A and B are not distinguishable) and $H_{AB} = H_{BA}^*$. Then, Eq. (1.7) leads to the solution

$$E = H_{AA} \mp |H_{AB}|. \tag{1.8}$$

H_{AA} (= H_{BB}) can be calculated by inserting Eq. (1.2) into Eq. (1.5) as follows:

$$H_{AA} = \frac{1}{N} \sum_{A} \sum_{A^*} e^{i\mathbf{k}\cdot(\mathbf{r}_A - \mathbf{r}_{A^*})} \int X^*(\mathbf{r} - \mathbf{r}_A) H X(\mathbf{r} - \mathbf{r}_{A^*}) d\tau. \tag{1.9}$$

If we only consider the effects of the nearest neighbors, we need to evaluate Eq. (1.9) for each atom A (B) with three nearest neighbor B (A) atoms,

$$H_{AA} = \int X^*(\mathbf{r} - \mathbf{r}_A) H X(\mathbf{r} - \mathbf{r}_A) d\tau = E_0. \tag{1.10}$$

while

$$\begin{aligned} H_{AB} &= \frac{1}{N} \sum_{A} \sum_{B} e^{i\mathbf{k}\cdot(\mathbf{r}_A - \mathbf{r}_B)} \int X^*(\mathbf{r} - \mathbf{r}_A) H X(\mathbf{r} - \mathbf{r}_B) d\tau \\ &= \frac{1}{N} \sum_{i} e^{i\mathbf{k}\cdot\rho_i} \int X^*(\mathbf{r}) H X(\mathbf{r} - \rho_i) d\tau, \end{aligned} \tag{1.11}$$

where $\boldsymbol{\rho}_i$ is a vector connecting atom A to its three nearest neighbor B atoms (see Figure 1.2(a)). By referring to the coordinate system of the graphene in Figure 1.1(a),

$$\begin{aligned} H_{AB} &= \left(e^{i\mathbf{k}\cdot\rho_1} + e^{i\mathbf{k}\cdot\rho_2} + e^{i\mathbf{k}\cdot\rho_3}\right) \int X^*(r) H X(r - \rho_1) d\tau = E_0 \\ &= \gamma_0 \left(e^{-ik_x a/\sqrt{3}} + 2e^{ik_x a/2\sqrt{3}} \cos\left(\frac{k_y a}{2}\right) \right). \end{aligned} \tag{1.12}$$

γ_0 is often called as the tight-binding integral or transfer integral which measures the strength of exchange interaction between nearest neighbor atoms. Then, from Eqs. (1.10) and (1.12), the energy dispersion in Eq. (1.8) can be calculated as follows:

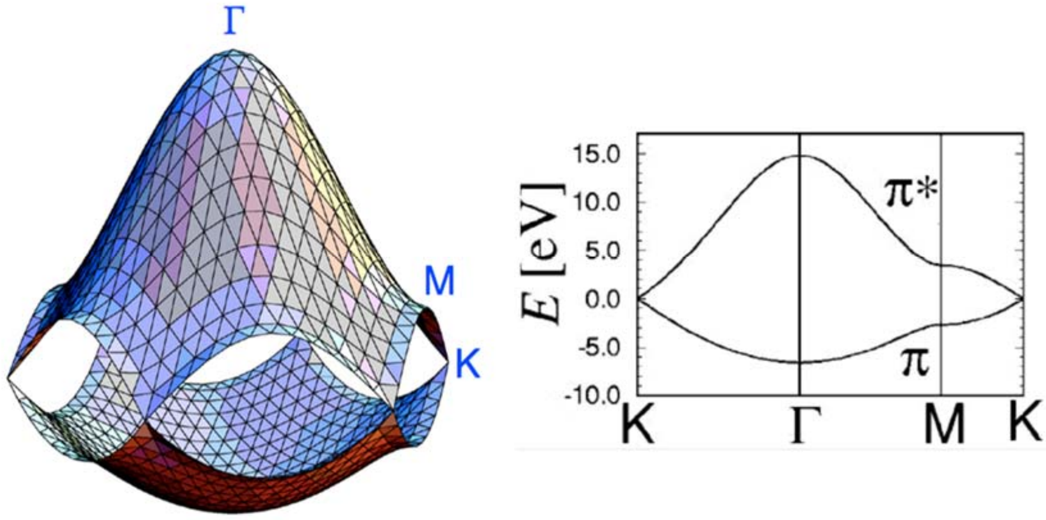

Figure 1.3. Energy dispersion of graphene along high-symmetry points as indicated in Figure 1.2(b). The figure is reproduced from http://flex.phys.tohoku.ac.jp/.

$$E = E_0 \mp \gamma_0 \left(1 + 4\cos(\frac{\sqrt{3}k_x a}{2})\cos(\frac{k_y a}{2}) + 4\cos^2(\frac{k_y a}{2}) \right)^{1/2}. \quad (1.13)$$

In Eq. (1.13), negative sign denotes valence bands of graphene formed by bonding π orbitals, while positive sign represents conduction bands forms by antibonding π^* orbitals. The dispersion relation in Eq. (1.13) is platted in Figure 1.3 along high-symmetry points in the reciprocal space with $E_0 = 0$. The surface and contour plots of the energy dispersion are also shown in Figure 1.4(a) and (b), respectively. The main feature of the energy dispersion of graphene is the six **K** points at the corners of the Brillouin zone, where the conduction and valence bands meet so that the bandgap is zero only at these points. Also note that the two **K** points ($\mathbf{K}_1$ and $\mathbf{K}_2$) are nonequivalent due to symmetry (they originated from two nonequivalent atoms in the real space unit cell). The circular contour around each **K** point in Figure 1.4(b) indicates the conic shape of dispersion near each **K** point.

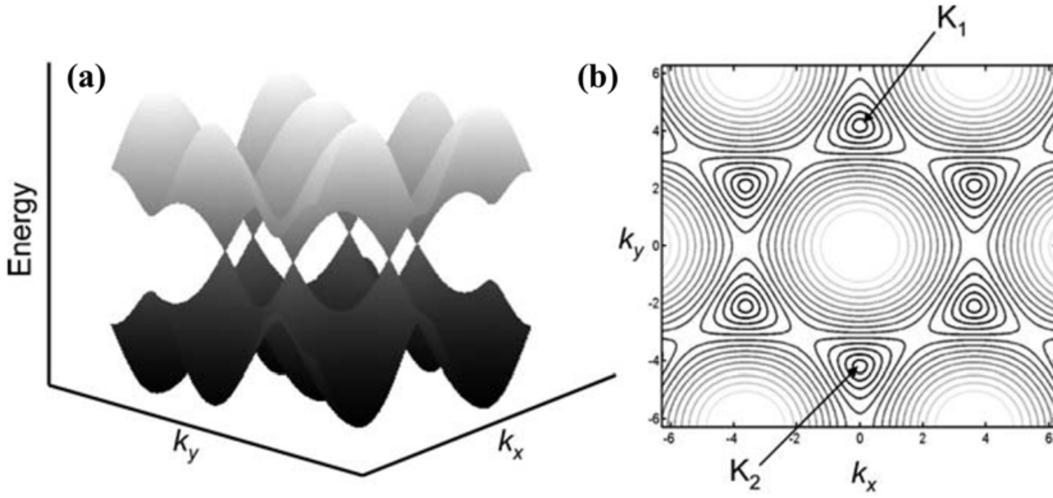

Figure 1.4. (a) Surface plot and (b) contour plot of the energy dispersion in graphene as given by Eq. (1.13). Note that there are six **K** points where the bandgap becomes zero. Of the six **K** points, only two are nonequivalent, denoted by $\mathbf{K}_1$ and $\mathbf{K}_2$.[6] Reproduced with permission. Copyright 2009, Springer.

The density of states (DOS) in graphene can be derived from the energy dispersion relation and it is found to be zero at the Fermi level.[9] Along with the zero bandgap, this is why graphene is a zero bandgap semiconductor. The slope of the conic shape dispersion near **K** points is proportional to the Fermi velocity of electrons in graphene, $v_F = 8 \times 10^5$ m/s,[10] as follows:

$$\left.\frac{\mathrm{d}E}{\mathrm{d}k}\right|_{\mathrm{K}} = \frac{\sqrt{3}}{2} a\gamma_0 = \hbar v_F. \tag{1.14}$$

Before moving on to the SWNT case, it is appropriate to check the validities of some approximations and simplifications made for the tight-binding approximation presented here. In deriving the energy dispersion in Eq. (1.13), two main assumptions were made. First, the overlap integrals S_{AB} and S_{BA} between carbon atoms A and B are neglected in Eq.

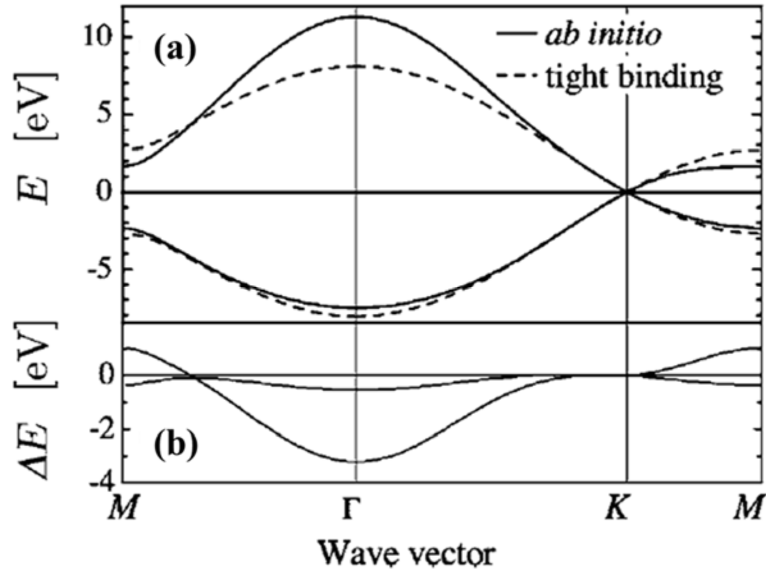

Figure 1.5. (a) Energy dispersion of graphene calculated by first principle (solid lines) and nearest neighbor tight-binding method as in this chapter (dashed lines). (b) Difference between the energy dispersions calculated in (a).[11] Reproduced with permission. Copyright 2002, American Physical Society.

(1.4). Second, only the nearest neighbor interactions are considered in evaluating Eq. (1.11). In the literature,[11] tight-binding calculations of graphene with more relaxed parameters were performed and compared to the *ab initio* calculations. As shown in Figure 1.5, the energy dispersion obtained in Eq. (1.13) tends to deviate further from the first principle result far away from **K** points. It is found that the inclusion of a small overlap integral ($S_{AB} < 0.1$) and the third nearest neighbor interactions are needed to obtain a better fit.[11] However, since we are only concerned with the energy dispersion near the **K** points, the results obtained here with some simplifications should still be a good approximation for the purpose of understanding electron transport properties.

1.2.2 Band structure of SWNT

A SWNT can be uniquely defined by a chiral vector, $\mathbf{C} = n_1\mathbf{a}_1 + n_2\mathbf{a}_2$, where n_1 and n_2 are integers and $\mathbf{a}_1$ and $\mathbf{a}_2$ are the unit vectors of the graphene lattice as shown in Figure 1.6. A SWNT is formed by rolling a graphene sheet in such a way that two carbon atoms pointed by **C** coincide. With wrapping indices, n_1 and n_2, SWNTs can be uniquely defined and described. SWNTs which are described by wrapping indices (n,n) and $(n,0)$, are called armchair and zigzag SWNTs, respectively.

Since a SWNT is a rolled-up sheet of graphene, the band structure can be constructed from that of graphene by imposing an appropriate boundary condition around the SWNT. If we consider a SWNT as an infinitely long cylinder, there are two wave vectors associated with it. The wave vector $\mathbf{k}_{\parallel}$, which is parallel to the SWNT axis, is continuous since the SWNT

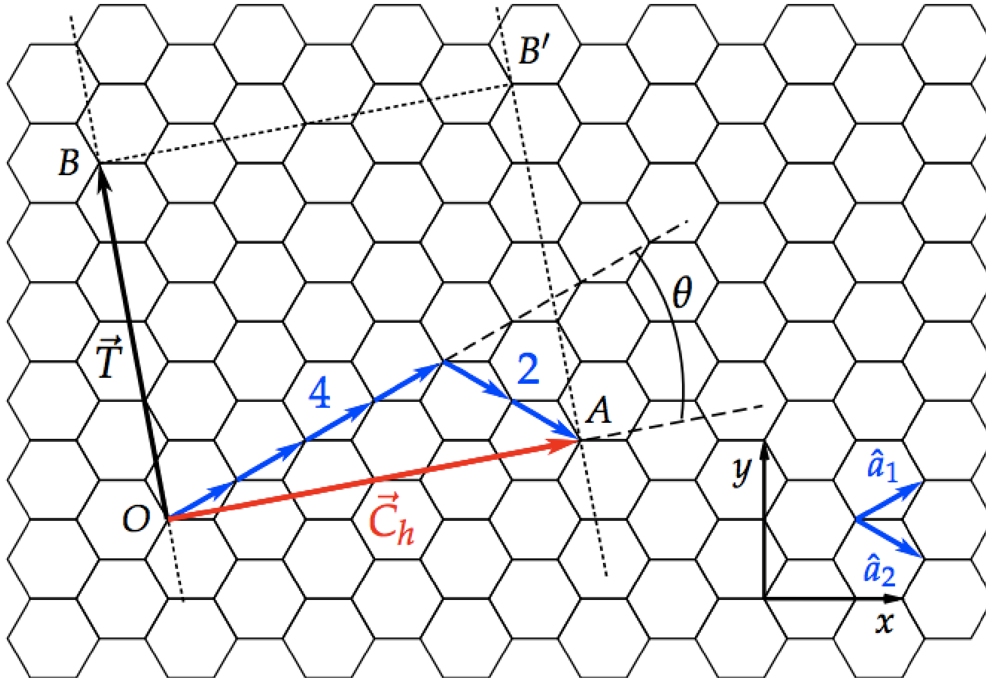

Figure 1.6. Representation of a SWNT by a chiral vector, $\mathbf{C} = n_1\mathbf{a}_1 + n_2\mathbf{a}_2$. In this figure, the wrapping index of the SWNT described by **C** is (4,2). $\mathbf{a}_1$and $\mathbf{a}_2$ are unit vectors of the underlying graphene lattice.

is assumed to be infinitely long, while the wave vector $\mathbf{k}_{\perp}$, which is along the circumference of a SWNT, should satisfy a periodic boundary condition (i.e., the wave function repeats itself as it rotates 2π around a SWNT),

$$\mathbf{k}_{\perp} \cdot \mathbf{C} = \pi d k_{\perp} = 2\pi m, \quad (1.15)$$

Where d is the diameter of a SWNT and m is an integer. This boundary condition leads to quantized values of allowed $k_{\perp}$ for SWNTs. Then, the 1D band structure of SWNTs can be obtained from cross-sectional cutting of the energy dispersion of 2D graphene with these allowed $k_{\perp}$ states as shown in Figure 1.7(a). This is called zone-folding scheme of obtaining the band structure of SWNTs. Each cross-sectional cutting gives rise to a 1D subband. Therefore, the 1D band structures of SWNTs are determined by the spacing between allowed $k_{\perp}$ states and their angles with respect to the surface Brillouin zone of graphene, which is set by the diameter and chirality of SWNTs, i.e., wrapping indices. Especially, the band structure near the Fermi level, most relevant for transport properties, is given by allowed $k_{\perp}$ states that are closest to the **K** points. When the allowed $k_{\perp}$ states pass directly through the **K** points as in Figure 1.7(b), the energy dispersion shows two linear bands crossing at the Fermi level without a bandgap. However, if the allowed $k_{\perp}$ states miss the **K** points as in Figure 1.7(c), then there are two parabolic 1D band with an energy bandgap. Therefore, we can expect two different kinds of SWNTs depending on the wrapping indices, metallic SWNTs without a bandgap as in Figure 1.7(b) and semiconducting SWNTs with a bandgap as in Figure 1.7(c). In this section, we will investigate the 1D subbands closest to the **K** points for zigzag SWNTs. You are referred to literatures for more general treatments of this subject. [5,12,13]

Zigzag SWNTs, represented by wrapping index (n,0), can be either metallic or semiconducting as will be shown below. Since the circumference is na ($\mathbf{C} = n\mathbf{a}_1$), the

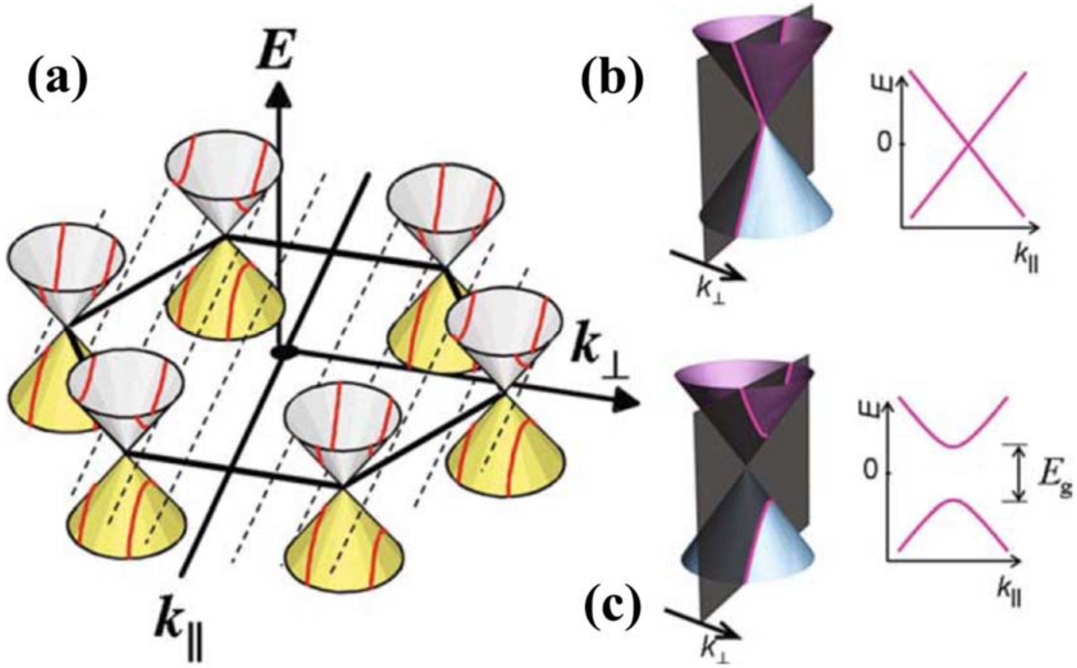

Figure 1.7. (a) A first Brillouin zone of graphene with conic energy dispersions at six **K** points. The allowed $k_{\perp}$ states in a SWNT are presented by dashed lines. The band structure of a SWNT is obtained by cross-sections as indicated. Zoom-ups of the energy dispersion near one of the **K** points are schematically shown along with the cross-sections by allowed $k_{\perp}$ states and resulting 1D energy dispersions for (b) a metallic SWNT and (c) a semiconducting SWNT.

boundary condition in Eq. (1.15) becomes

$$k_x na = 2\pi m. \tag{1.16}$$

When n is a multiple of 3 (n=3q, where q is an integer), there is an allowed k_x that coincides with a **K** point, which is at (0, 4π/3a). By substitution,

$$k_x = \frac{2\pi m}{na} = \frac{3Km}{2n} = \frac{Km}{2q}. \tag{1.17}$$

Then, there is always an integer m (= 2q) that makes k_x pass through K points so that these

kinds of SWNTs (with $n = 3q$) are always metallic without a bandgap as shown in Figure 1.7(b).

There are two cases when n is not multiple of 3. If $n = 3q + 1$, we can find k_x closest to **K** point at $m = 2q + 1$, as shown in Figure 1.7(c).

$$k_x = \frac{2\pi m}{na} = \frac{3Km}{2n} = \frac{3K(2q - 1)}{2(3q+1)} = K + \frac{K}{2}\frac{1}{3q+1}. \quad (1.18)$$

Similarly, for $n = 3q - 1$, the allowed k_x closest to **K** is when $m = 2q - 1$,

$$k_x = \frac{2\pi m}{na} = \frac{3Km}{2n} = \frac{3K(2q-1)}{2(3q-1)} = K - \frac{K}{2}\frac{1}{3q-1}. \quad (1.19)$$

In these two cases, allowed k_x misses K point by

$$\Delta k_x = \frac{K}{2}\frac{1}{3q \pm 1} = \frac{2\pi}{3na} = \frac{2\pi}{3\pi d} = \frac{2}{3d}. \quad (1.20)$$

Therefore, the smallest misalignment between an allowed k_x and a **K** point is inversely proportional to the diameter. Then, from the slope of a cone near **K** points, as shown in Eq. (1.14), the bandgap E_g is given by

$$E_g = 2 \times (\frac{\partial E}{\partial k}) \times \frac{2}{3d} = 2\hbar v_F(\frac{2}{3d}) \approx 0.7\text{eV}/d(\text{nm}). \quad (1.20)$$

Therefore, semiconducting SWNTs ($d = 0.8 \sim 3$ nm) have a bandgap in the order of 0.2 ~ 0.9 eV, inversely proportional to the diameter. Similar treatment for armchair SWNTs (n,n) leads to the conclusion that they are always metallic.

Extending the above results, SWNTs with wrapping indices (n_1,n_2) can be categorized into three different kinds based on p, which is the remainder when the difference between wrapping indices n_1 and n_2 is divided 3 (i.e., $n_1 - n_2 = 3q + p$):[physical pro][12]

(i) $p = 0$; metallic with linear subbands crossing at the K points.

(ii) $p = 1, 2$; semiconducting with a bandgap, $E_g \sim 0.7$ eV/d (nm).

In 1D metals, composed of chains of atoms or molecules, bond alternations (dimerizations) occur which open up a bandgap, a phenomenon known as Peierls

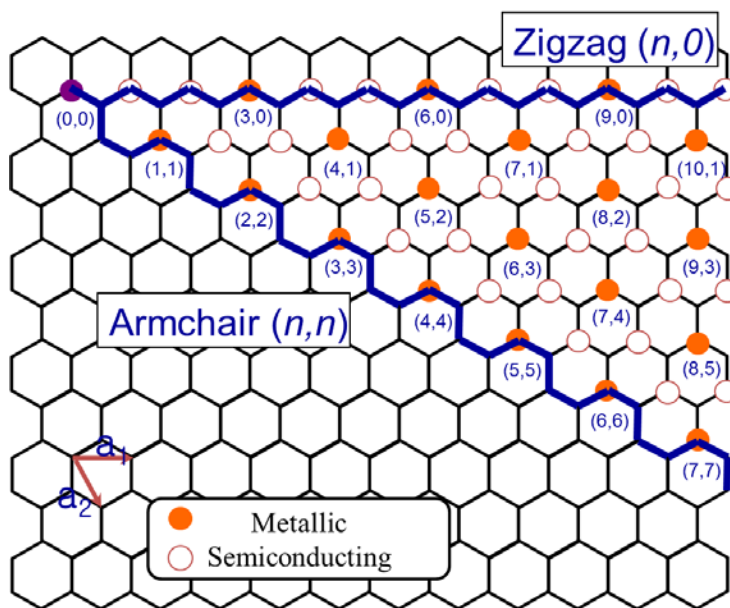

Figure 1.8. The carbon nanotubes (*n*,*m*) that are metallic and semiconducting, respectively, are denoted by open and solid circles on the map of chiral vector (*n*,*m*).

distortion.[14] This is why 1D conducting polymers are not metallic at room temperature without doping. Although metallic SWNTs are 1D metals, they consist of rigid interwoven carbon bonds which cannot be easily distorted to open a bandgap. Therefore, Peierls distortion in not expected in SWNTs.[5,6,10]

1.2.3 Indexing of SWNTs

Many electronic applications of carbon nanotubes crucially rely on selectively growing or separating either semiconducting or metallic nanotubes, preferably of certain chirality. Figure 1.8 shows which carbon nanotubes are metallic and which are semiconducting, denoted by open and solid circles, respectively. It follows that approximately one third of the carbon nanotubes are metallic and the other two thirds semiconducting. As-grown carbon nanotubes also are generally provided with 20 ~ 30 % in metallic CNT and 70 ~ 80 % in semiconducting CNT.

1.3 Characterization of Graphene and SWNT

1.3.1 Resonance Raman Spectroscopy

Raman spectroscopy has played an important role in the study and characterization of graphitic materials,[15] being specifically used to characterize fullerenes,[16] carbon nanotubes,[13,17,18] and graphene.[19] For sp^2 nanocarbons such as graphene and carbon nanotubes, Raman spectroscopy can give information about crystallite size, clustering of the sp^2 phase, the presence of sp^2-sp^3 hybridization and the introduction of chemical impurities, the magnitude of the mass density, the optical energy gap, elastic constants, doping, defects and other crystal disorder, edge structure, strain, number of graphene layers, nanotube diameter, chirality, curvature, and finally the metallic vs semiconducting behavior and the

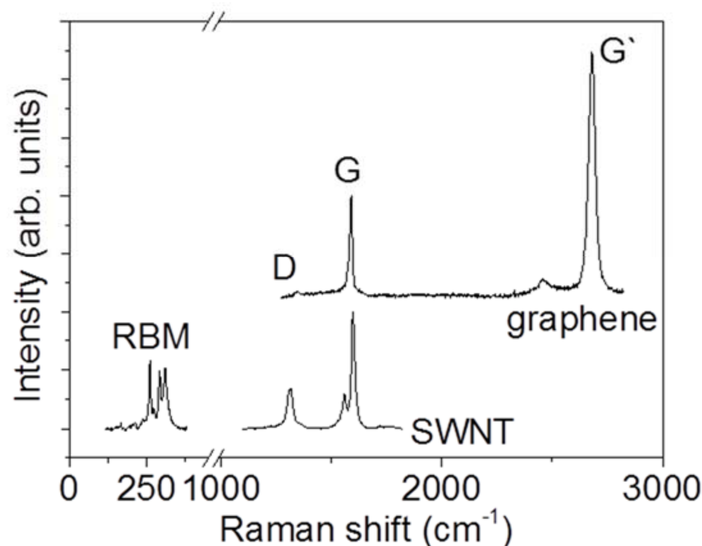

Figure 1.9. Raman spectra from different types of sp^2 nanocarbons, such as graphene and SWNT. The graphene-related structures are labeled next to their respective spectra. The detailed analysis of the frequency, line shape, and intensity for these features gives a great deal of information about each respective sp^2 carbon structure.

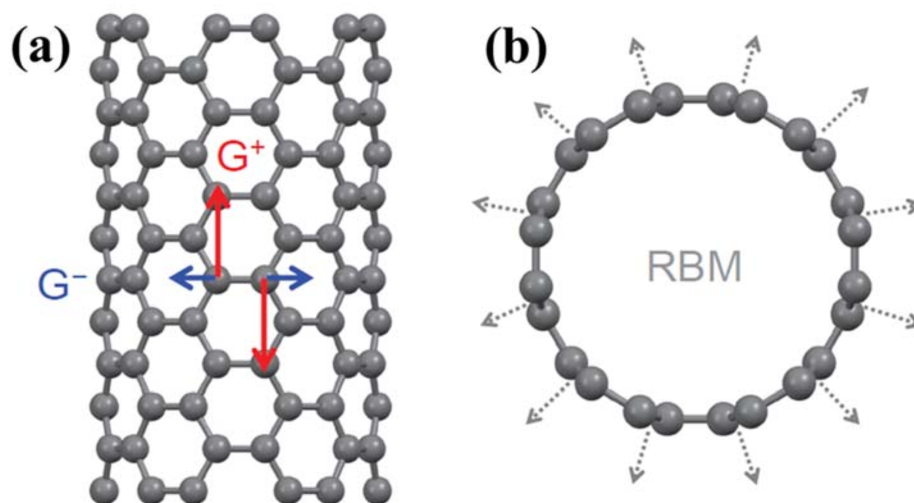

Figure 1.10. (a) The in-plane vibrational modes corresponding to the G-band Raman signal, and (b) the uniform out-of-plane vibration that gives rise to the radial breathing mode excitations.

science of excitons which make carbon nanotubes unique.[20] Various Raman features are discussed including the G-band at ~ 1582 cm^{-1}, which is common to all sp^2 carbon forms, the radial breathing mode (RBM) that makes the diameter and optical transition energy analysis of nanotubes possible, and the D- and G`-band that are significant in providing information about the electron and geometrical structure through the double resonance process as shown in Figure 1. 9.

The dominant peak at around 1582 cm^{-1} corresponds to a resonant excitation of in-plane optical phonons, reflecting the graphite nature of the SWNT.[17] Therefore, this peak is called the G-band, where G stands for graphite. However, the curvature of the SWNT causes the longitudinal and transverse in-plane vibrational modes to have a slight difference in energy, resulting in a split of G$^-$band into a lower energy G$^-$ peak and a higher energy G+ peak as shown in Figure 1.10(a). The RBM is also a resonant Raman mode, which is in resonance when the energy of the incident photon matches an energy gap E_{ii} in the SWNT electronic

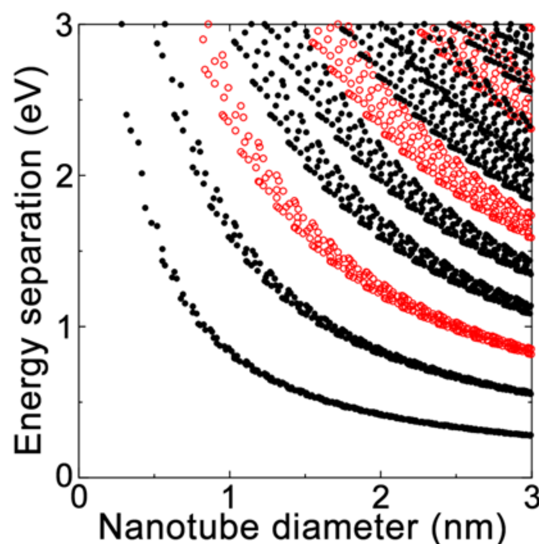

Figure 1.11. Calculation of the transition energy as a function of the diameter for all (*n,m*) SWNTs. Black and red dots indicate semiconducting and metallic SWNTs, respectively.[23] The figure is reproduced from http://www.photon.t.u-tokyo.ac.jp/index.htm

DOS. Each peak in the RBM feature corresponds to an SWNT with a certain diameter as shown in Figure 1.10(b).[17]

1.3.2 Kataura plots

The transition energies in SWNTs have systematic dependence on diameter when they are considered with certain approximations. The first approximation of transition energy as a function of both diameter and chirality is calculated using tight-binding theory,[21] and it is commonly referred to as Kataura plots.[22] Kataura *et al.* first showed how the $1/d$ average behavior splits into different values for different chiralities. An example of Kataura plots is shown in Figure 1.6.[23] Using Kataura plots the chirality and diameter of an SWNT can be determined from the optical spectroscopy information from its transition energies.

1.4 Nanocarbon-based field-effect transistors (FETs)

1.4.1 Single-walled carbon nanotube FETs

In order to perform electrical transport measurements of SWNTs, a three terminal device configuration is often used. Two electrodes directly contact an individual SWNT (Source and drain electrodes), and there is often a third electrode, capacitively coupled to the nanotube through an insulating dielectric layer (gate electrode, as in transistors). Figure 1.12 shows a schematic diagram of a back-gated SWNT device. Typical transport measurements involve source/drain current (I_{ds}) measurements as a function of either source/drain (V_{ds}) or gate (V_{gs}) voltage. This setup involves two junctions between the sample (SWNT) and the probes (source and drain), which makes it harder to associate the measurement result with simple physical quantities such as DOS.

The first electrical transport measurements of individual SWNTs were reported in the late 1990s for both metallic and semiconducting SWNT.[24-27] It was found that I_{ds}-V_{gs} characteristics of SWNTs depend strongly on whether they are semiconducting or metallic,

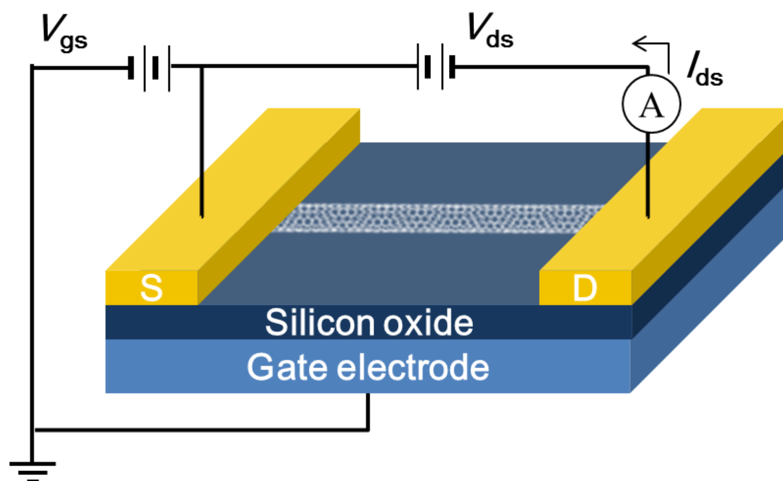

Figure 1.12. A schematic of typical setup for electrical transport measurements of SWNTs. Typically, I_{ds} as a function of V_{ds} or V_{gs} is measurement for transport experiments.

as depicted in Figure 1.13(a) and (b). The gate voltage (V_{gs}) shifts the Fermi level of the SWNTs while the quasi-Fermi levels of source and drain metal electrodes are fixed, since the DOS in a bulk metal electrode is much larger. For semiconducting SWNTs, this changes the relative positions of the SWNT band gap to the Fermi levels of the source and drain, which modulates I_{ds} significantly as shown in Figure 1.13(a). The current can be suppressed down to zero by V_{gs}. But for metallic SWNTs, there is no band gap and the DOS is finite (constant) up to the next 1D subbands so that there is almost no change in Ids as a function of V_{gs} as in Figure 1.13(b). The large modulation of the I_{ds} by V_{gs} in semiconducting SWNTs suggests that they can work as field effect transistors. Since its first demonstrations,[25,27] SWNT-based FETs have extensively been studied for possible applications in electronic devices. I_{ds}-V_{gs} characteristics as in Figure 1.13(c) are also often observed and they have been attributed to the metallic SWNTs with small band gaps (for instance, due to the curvature-induced σ-π mixing).[28] Note that due to much smaller band gaps, the current is modulated by gate voltage but it is not reduced to zero, unlike the semiconducting SWNTs. These three kinds of I_{ds}-V_{gs} characteristics in various SWNTs confirm the existence of different kinds of SWNTs. In most cases, the electrical transport measurements are limited to the first 1D subbands near the Fermi level, since the typical gate voltage range is not large enough to allow transport through higher 1D subbands. Therefore, the existence of higher 1D subbands with singularities are not easily seen in the transport measurements.

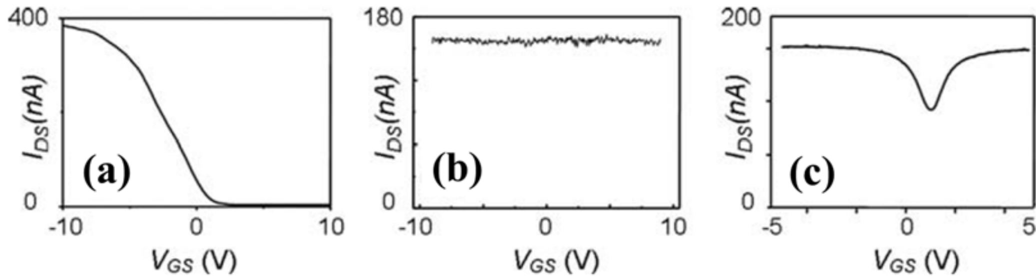

Figure 1.13. Drain current (I_{ds}) as a function of the gate voltage (V_{gs}) for a (a) semiconducting, (b) metallic, and (c) semiconducting with a small band gap SWNT. V_{ds} = 10 mV for all data.[6]

1.4.2 Graphene-based field-effect transistors

Semiconductor technology can be broadly classified into digital and analog electronics. Digital electronics mostly use silicon-based complementary MOSFETs as the unit of switching, are highly integrated (with billions of transistors per chip), and are made in fabs that cost at least USD 1B to build. In addition, the tremendous resources invested in the last four decades have given Si CMOS technology a huge performance advantage. Thus, any new technology that wants to compete with Si technology in digital electronics faces high barriers to entry-from investments required to replace existing fabs to technology development needed to outperform Si CMOS. Analog electronic circuits, on the other hand, are not highly integrated, and thus are more open to new technologies. Analog circuits are mostly used in the baseband and RF areas for telecom applications and can be implemented in COMS as well as non-silicon materials including SiGe, InP, and GaAs. Thus, graphene has the immediate potential to be applied in analog circuits.

While Si MOSFETs are usually top-gated, early graphene FETs (GFETs) were bottom gated. In fact, the optical visibility of single layer graphene (SLG) flakes on 300 nm of SiO_2

was one of the main reasons for back-gating graphene FETs.[29] The scotch-tape technique, first proposed by Geim and Novoselov, had wide appeal thanks to the simple tools needed to obtain SLG-repeated peeling of graphite yielded SLG that could then be transferred onto oxidized Si substrates and identified by optical microscopy. E-bean lithography was usually used to align to micron-sized flakes, and metallic contacts were patterned on the flake. One lithography step was thus sufficient to obtain a back gated FET. To pattern nanoribbons, additional lithography and etch steps are required. Top-gated FETs would require additional lithography and etch/deposition steps depending on the type of FET desired. A cross-section of back-gated and top-gated GFETs is show in Figure 1.14. Epitaxial graphene typically uses top-gated FETs to study device properties.[30] FETs with a combination and back- and top-gating have been used to study various device phenomena such as band gap opening in bilayer graphene.[31]

The term "GFET" could mean either large-area graphene FETs or graphene nanoribbon (GNR) FETs; GNRs can be formed either from large-area graphene (by lithography and etch) or chemically (from graphite or CNTs). In a GFETs, varying the gate potential changes the channel Fermi level; this in turn makes the graphene channel either n-type or p-type, and leads to a unique current-voltage curve. When $E_F \sim 0$, the conductivity is minimum; the intrinsic carrier density of graphene is predicted to be $n_i \sim 10^{11}$ cm^{-2}.[32] When $E_F > 0$ (i.e. $V_g < 0$), electrons are induced in the channel, leading to mostly electronic conduction. Similarly, when $E_F < 0$, the channel is in majority-hole conduction. The gate voltage at which conductivity a minimum (V_{gmin}) is zero for ideal graphene but for as-fabricated samples dependent on a number of parameters including impurity type and density, doping from various overlayers, and the work function difference between graphene and the substrate.

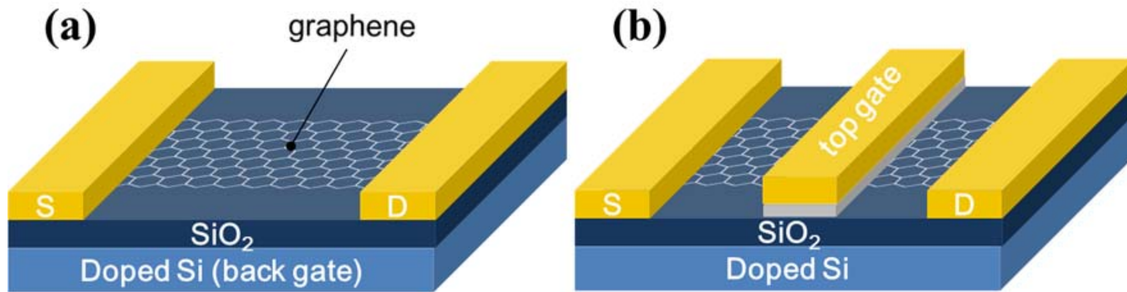

Figure 1.14. Back-gated and top-gated graphene FETs are shown in (a) and (b) respectively. Exfoliated and CVD graphene are usually on 300 nm or 90 nm SiO_2 substrate on doped Si. The doped Si allow for backgating.

Using simple gate electrostatics, the on-off ratio of 2D graphene FEETs can be estimated. For large-area back-gated GFETs on 300 nm SiO_2 with $V_g \sim 50$ V, the induced carrier density is $\sim 3 \times 10^{12}$ cm^{-2}; since $\sigma = en\mu$, the modulation of conductivity would be ~ 30 (= n_e/n_i), where n_e is the induced carrier density, assuming that mobility (μ) is constant as carrier density increases in the channel. In monolayer graphene, Coulomb-impurity limited mobility is found to be independent of carrier density (n) while the mobility limited by short-range scattering has a $\mu \propto 1/n$ dependence;[33] assuming negligible short-range scattering, the maximum on-off ratio will be 30, for V_g in the range ±50 V. Due to impurity-induced effects, the carrier density at $V_g = V_{gmin}$ is higher than n_i and the on-off ratios measured have been smaller than 30 for monolayer graphene. Also, the constant μ make the α-V_g relationship to be linear-however, μ could be different between the electron and hole regimes because of various symmetries in the FET.

1.5 Doping strategy for SWNT and graphene field-effect transistors

1.5.1 Doping of SWNT-based field-effect transistors

P-N junctions constitute the building blocks for virtually all conventional micro electronic device structures, and the precise control of the chemical doping profiling of semiconductor materials presents the key for device performance optimization. For planar Si structures, chemical doping is achieved by replacing the lattice atoms by impurities with three (acceptor) or five (donor) valence electrons. In carbon nanotubes, however, replacement of the carbon lattice atoms results in a severe degradation of the carrier mobility due to the destruction of the C-C sp^2 network and localization of the carriers. The doping in these surface structures is instead attained through the charge transfer from non-covalently bonded electron donating or withdrawing molecular precursors.[34-40] This is quite unique to a 1-D system where all atoms are near the surface (in case of SWNTs, all atoms are at the surface), and therefore, efficient doping can be attained through surface engineering and

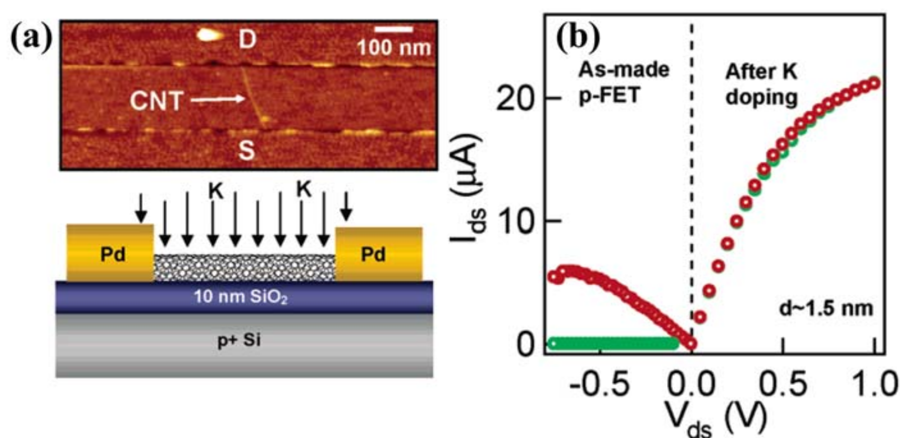

Figure 1.15. n-doping of nanotubes by K vapor. (a) AFM image of a nanotube device (top) and schematic drawing of K doping of the device (bottom). (b) I_{ds}-V_{ds} characteristics of a device before and after K doping at two gate voltage V_{gs} = -3 (red) and 0 V (green).[42] Reproduced with permission. Copyright 2005, American Chemical Society.

charge injection. Charge injection provides a major advantage over lattice replacement as defects are not introduced in the lattice, and therefore, reducing the defect scattering of the carriers due to dopant species.

Chemical doping of carbon nanotubes by charge injection was first demonstrated by Jing Kong et al. The researcher observed the doping effect of NO_2 and NH_3 gases on nanotube devices, therefore, allowing the detection of these molecules by CNTFETs.[37] Upon absorption of NO_2 on the nanotube surface, a dramatic p-type doping effect was observed owing to the well-established electron withdrawing nature of NO_2. On the other hand, NH_3 absorption resulted in electron injection into the nanotubes, therefore, effectively n-type doping the nanotubes. The same researcher also demonstrated the potassium (K) doping of nanotubes and doping profiling for enabling various P-N junction structures.[34-36] As compared to NH_3, potassium shows a significantly stronger electron donating behavior (~ one electron per K atom), therefore, enabling heavily n-doping of nanotubes. IBM researchers utilized this strategy for uniform n-doping of nanotubes by K to achieve metal-contacted n-FETs (K was evaporated on top of nanotubes FETs in vacuum),[40] leading the way to the demonstration of the first complementary inverter logic gate on a single nanotube.[41] Later, A. javey et al. demonstrated the first MOSFET-like nanotube structure with chemically doped (n+) contacts and chemically intrinsic channels by patterned doping of nanotubes with potassium as shown in Figure 1.15.[42] A disadvantage of K is that it is not

Table 1.1. Work function table of various metal electrodes for CNT FET.

Materials	CNT	Au	Pd	Pt	Cr	Mg	Ca
Work function [eV]	~ 4.8	5.1	5.4	5.8	4.4	3.6	2.9

air stable, and requires the dopant coverage and measurement to be done under a vacuum environment. Beside gas molecules and alkali metals, air stable polymer, such as polyethyleneimine,[39] have also been shown to successfully dope the nanotubes. While polymers exhibit better air stability, so far, they have enabled only low to moderate doping concentrations, therefore, limiting their application for contacts. This is due to their weaker electron donating characteristics as compared to potassium. Still significant work needs to be done in designing appropriate dopant molecules for heavy n- and p-doping of nanotubes with long term stability in ambient air condition. Better theoretical understanding of the interactions between various molecular species and nanotubes is also needed in guiding the design of the ideal dopant structures.

Although the chemical approach is good for scientific purpose, this approach is often disfavored by the industry due to the contamination issues. Here shows several methods of doping without chemical approaches. Figure 1.16(a) shows the transfer curves of CNTFETs using different metal contact electrodes such as Pd, Ti, Mg, and Ca.[43] The transfer characteristics show the p-type behavior in the case of Pd and Ti, ambipolar behavior in the case of Mg, and n-type behavior in the case of Ca electrodes. The Fermi level of the source electrodes is positioned close to the valence band of the carbon nanotube, resulting in p-type conductions from the large work function of the Pd and Ti electrodes due to the hole injection into the carbon nanotube. The Fermi level of the Mg electrode is positioned in the middle of the nanotube band gap, resulting in ambipolar characteristics. In the case, both electrons and holes are injected into the nanotube, depending on the polarity of gate bias. The Fermi level of the Ca electrode, with low work function, lies close to the conduction band of the carbon nanotube, exhibiting n-type conduction property due to the electron injection. Although this method works to control the type of doping, use of different metal

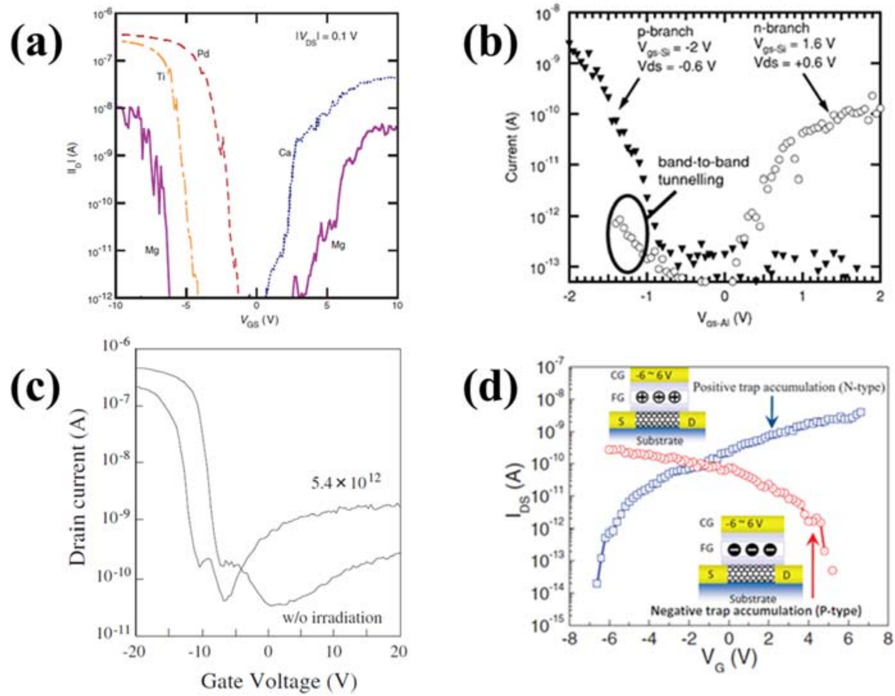

Figure 1.16. Non-chemical doping strategy of SWNT. (a) Transfer characteristics of the CNTFET varied from p-type through ambipolar to n-type with decreasing work function of the contact metal electrodes.[43] (b) Transfer characteristics of a dual-gate CNTFET measured at constant bottom gate ($V_{gs\text{-}Al}$) voltages exhibiting clear p-type and n-type unipolar behaviors depending on the electrostatic doping y back gate ($V_{gs\text{-}Si}$).[44] Reproduced with permission. Copyright 2005, IEEE. (c) Transfer characteristics of CNTFET without and with nitrogen ion irradiation dose of 5.4 × 10^{12} ions cm^{-2}.[45] Reproduced with permission. Copyright 2005, The Japan Society of Applied Physics. (d) Transfer curves of a CNTFET that consists of a floating gate in between top gate and channel. The device shows p-type and n-type behavior due to trap layer-induced electrostatic doping from floating gates.[46] Reproduced with permission. Copyright 2009, Wiley.

electrodes in high density device fabrication could be problematic and lead to a complicated

process.

Type conversion of CNTFETs can be achieved by electrostatic doping. Figure 1.16(b) shows p-type and n-type branches of CNTFET by electrostatic doping.[44] Transfer characteristics of the device using a bottom-gate electrode shows p-type behavior under a constant negative back gate (-2 V) and source-drain bias (-0.6 V), whereas the device exhibits n-type behavior under a constant positive back gate (1.6 V) and source-drain bias (0.6 V).

Ion implantation can also partially dope CNTs. Nitrogen ion irradiation (with an energy of 25 eV and a dose of 5.4×10^{12} ions cm^{-2}) onto CNT device downshifts the threshold voltage and the current increases in positive gate bias region, exhibiting ambipolar characteristics, which is again n-type doping behavior in Figure 1.16(c).[45]

It can be also shown that the type conversion of CNTFETs could be possible by trap-layer-induced electrostatic doping using a charge-trap layer between top gate and nanotube active channel.[46] Figure 1.16(d) shows the transfer curves of p-type and n-type CNTFET converted using Au floating gate. At high negative gate bias (-20 V), which is applied initially before the device operation, positive charges are trapped in the trap layer. Therefore, electron tunneling is favored, creating n-type doping behavior. The gate voltage sweep between -6 V and +6 V then provides I-V characteristics of n-type FET. Inversely, negative charges are trapped at high positive gate bias (+20 V), where hole tunneling is favored, creating a p-type FET. The gate voltage sweep between -6 V and +6 V provides n-type FET behavior.

1.5.2 Doping of Graphene-based field-effect transistors

Doping offers a way to control the conductivity of graphene, and can also allow control of

carrier type. Doping also allows for tuning the carrier injection from the contact to the semiconducting material-band alignment between the electrode and semiconductor is critical for efficient carrier injection. Traditional doping in semiconductors such as Si has been substitutional-an atom of the dopant replaces a host atom and donates a hole or electron. A doping density of 1 per 100,000 host atoms can improve Si conductivity by orders of magnitude compared to intrinsic Si.[47] Carrier mobility in Si falls with increasing doping due to increased scattering from the dopant atoms. For e.g. when doping density increases from 10^{15} cm^{-3} to 10^{18} cm^{-3}, mobility reduces from more than 1000 $cmV^{-1}s^{-1}$ to 300 $cmV^{-1}s^{-1}$. Complementary doping in Si is the cornerstone of CMOS circuits; n-type and p-type transistors are coupled together such that there is no current path from source to ground when the circuit is not switching. Switching from bipolar and NMOS technologies to CMOS resulted in a dramatic reduction in the energy dissipation of solid state circuits.

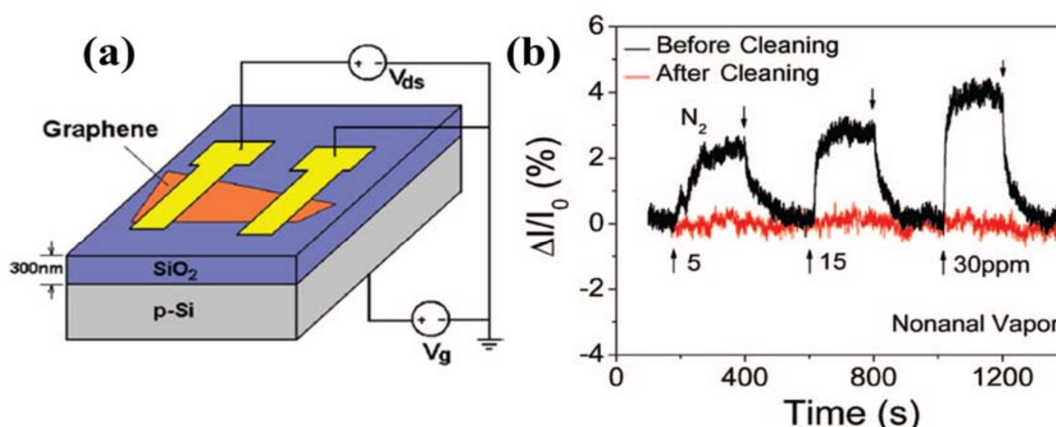

Figure 1.17. (a) Device schematic. (b) Measured sensor responses, before and after device cleaning. Exposure to nonanal vapor results in a 3 % change in current (for 5 ppm exposure) before sample cleaning; but the response drops by 1-2 orders of magnitude after sample cleaning.[50] Reproduced with permission. Copyright 2009, American Chemical Society.

A number of materials have been used to dope graphene. Unlike substitutional doping in solid state semiconductors, graphene doping is mostly surface charge transfer based. It was observed early on that flaked graphene devices were slightly p-doped even through intrinsic graphene is supposed to be undoped. This p-doping was thought to come from oxygen or water vapor in the ambient. In a controlled experiment, it was found that NH_2 and CO dope graphene n-type whereas H_2O and NO_2 dope it p-type, for gas concentration in the ppm range.[48] The high surface area to volume ratio of graphene makes it a very good sensing platform; on the other hand, because of the unavailability of bonding sites on ideal graphene, most sensing is performed by surface charge transfer doping rather than covalent bonding. Graphene transistors have been used a probe for getting insight into electrochemical reactions at interfaces, especially atmospheric doping of graphene; the water/oxygen redox couple was identified as the underlying mechanism.[49]

It was also noticed that the enhanced sensitivity of graphene to various gases was more than to process residues adhered to its surface rather than the intrinsic response of graphene.[50] These process-induced residues on graphene can be cleaned by current anneals or furnace anneals. Furnace anneals typically involve placing the sample in H_2/Ar flow at elevated temperatures (> 440 ^{o}C) for 1 h. Compared to as fabricated (contaminated) devices, cleaned devices had roughly one-third the concentration of doped carriers, four times higher carrier mobility, and much weaker electrical response (1-2 orders of magnitude lower) on exposure to chemical vapor, as shown in Figure 1.17. AFM measurements revealed that cleaned graphene had a much reduced thickness; in addition, hysteresis in electrical measurements was also reduced significantly. It is likely that resist residue acts as an adsorbent layer that concentrates molecules from the vapors, and thus amplifies the sensitivity of graphene. Polymer films are used as analyte concentrators in some types of

vapor sensors, and polymer on graphene could be performing a similar function.

The roughness of the substrate has been found to carry over to graphene,[51] and this introduces additional scattering. Also, surface impurities on the SiO_2 substrate introduce electron hole puddles in graphene,[52] causing impurity scattering. In addition, the ambient doping of graphene is thought to occur in large part because of the interaction of atmosphere with the SiO_2 substrate. Thus, there is a quest for alternatives for SiO_2 substrates, and various substrates have been tried including mica, SiN, hexagonal boron nitride (h-BN), ferroelectric substrate, and various types of surface functionalization. It has been noticed that ambient doping of graphene can be reversed; the intrinsic doping level drops when graphene is placed in vacuum for an extended period; this can be accelerated by heating the sample above 140 ^{o}C. This behavior seems to suggest that loosely bound species, like water attached to the silanol groups of the surface, are the main culprits for ambient doping. The initial state of doping is returned when graphene is exposed to air for a short time (1 min). This reversibility suggests that adsorbate-induced doping is dependent on substrate specific properties. Substrate quality depends on the morphology and defects of the SiO_2 surface (for flaked graphene); it is thought that when adsorbates such as hydroxyl groups attach to dangling bonds on the surface, there is a buildup of silanol (SiOH) layer which is hydrophilic. Dipolar molecules can attach to the silanol layer and cause adsorbate-induced doping of graphene. This was a motivation behind chemical hydrophobization of the substrate;[53] the process involves leaving the SiO_2 substrate in a HMDS solution for more than 15 h; the HMDS molecules seem to form an ordered self-assembled layer on the substrate. Electrical measurements reveal that mobilities as high as 12,000 cm$V^{-1}s^{-1}$ can be obtained and gate hysteresis is suppressed even in ambient conditions. The HDMS screens the influence of substrate charges, and leads to a more

reproducible behavior between different graphene flakes. In a separate work, phenyl-alkyl terminated self-assembled monolayers were used to functionalize the oxide surface before transfer of CVD graphene to SiO_2. This was found to result in an improved carrier mobilitiy.[54]

H-BN has been found to have an atomically smooth surface and a low density of dangling bonds and charge traps. In addition, its lattice constant is similar to that of graphite and it has a large electrical band gap. Mono- and bilayer graphene on h-BN have been found to have carrier mobilities an order of magnitude higher than graphene on SiO_2; the devices on h-BN also show reduced chemical reactivity and display intrinsic doping.[55]

Charge screening has been used to limit disorder induced by the substrate. Ferroelectric PZT substrates were used as a support for graphene flakes; these substrates had a large spontaneous polarization pointing into the surface.[56] This polarization is thought to be almost fully screened by a high-density layer of surface adsorbates prior to exfoliation since scattering from interfacial adsorbates was found to be much weaker than on SiO_2; carrier

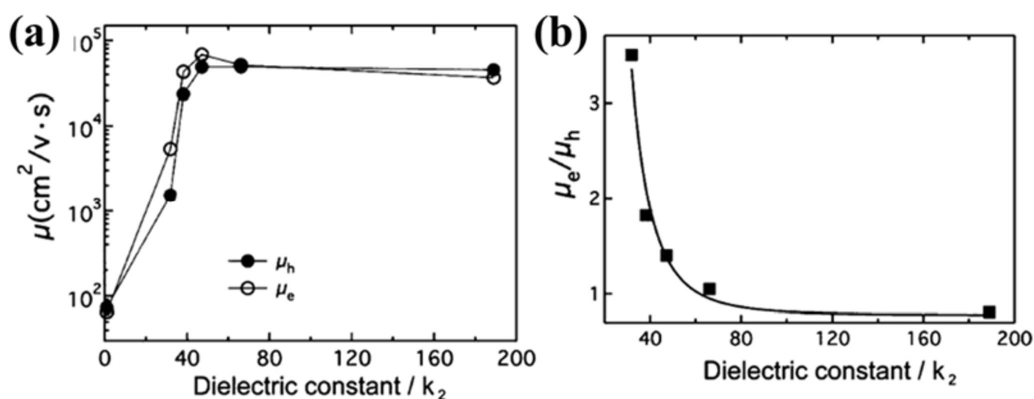

Figure 1.18. (a) Carrier mobility versus dielectric constant of solution (κ_2). Both electron and hole mobility improve as κ_2 increases. (b) Ratio of electron to hole mobility versus κ_2.[57] Reproduced with permission. Copyright 2009, American Chemical Society.

mobility in excess of 70,000 $cmV^{-1}s^{-1}$ at n = 2.4 × 10^{12} cm^{-2} and T = 300 K was measured. Screening was studied by immersing graphene in various organic solvents, with dielectric constants up to 189 (N-methylformamide).[57] The transport characteristics change systematically with dielectric constant; carrier mobility up to 70,000 $cmV^{-1}s^{-1}$ have been measured in graphene devices in a high-**K** solution (with a dielectric constant κ_2). Beyond a certain κ_2, transport properties do not improve further, indicating that the intrinsic limit of room temperature mobility has been reached (for graphene on SiO_2), in Figure 1.18. The ratio of electron to hole mobility was found to decrease sharply from more than 3 to almost 1 when κ_2 approaches 80. The asymmetric scattering in graphene has been attributed to the differing scattering cross sections by charged impurities for holes and electrons. As the charged impurity scattering is screened, this asymmetry disappears. It was also found that short range scattering is unaltered by the high-**K** solvents. Ionic solutions of NaF have also been used to investigate screening;[57] it was noticed that as the ionic concentration is increased from 0.005 **M** to 1**M**, carrier mobility increases by more than 5 times; the position, and the width of the minimum conductivity point changes significantly, indicating a much weaker intrinsic doping of graphene with increasing ionic concentration.

There have been a few reports of substitutional doping of graphene. N-doped graphene is obtained by irradiating graphene with 30 keV N^+-ions followed by an anneal in NH_2, in Figure 1.19.[58] Raman spectroscopy was used to confirm that defects created by N^+ irradiation were restored after the NH_3 anneal. Annealing in NH_3 was compared to that in N_2; when annealing in N_2 was followed by Auger electron spectroscopy (AES), there was no N-signal; however, an anneal in NH_3 revealed an N signal. Back gated transport measurements reveal that V_{gmin} is negative after the NH_3 anneal but positive after an N_2 anneal; the positive V_{gmin} after N_2 anneal was thought to be from atmospheric doping of

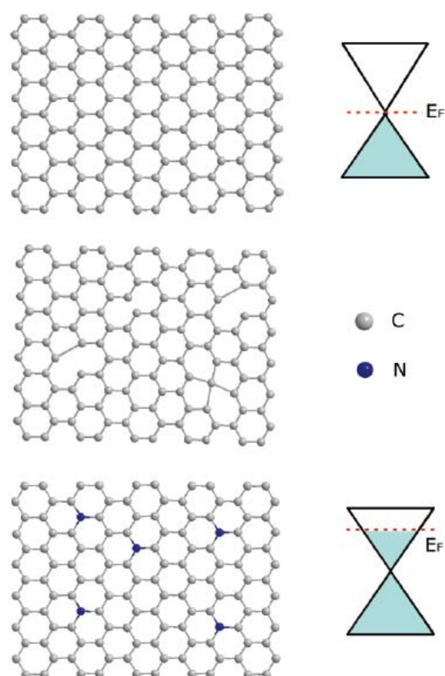

Figure 1.19. The atomic structure of graphene annealed in NH_3 after irradiation. Graphene is doped by substituting C atoms with N atoms.[58] Reproduced with permission. Copyright 2010, American Chemical Society.

defect sites. Carrier mobility was measured to be a few 1,000 after the NH_3 anneal.

Diazonium salts and poly(ethylene imine) (PEI)were used to dope graphene to be p-type and n-type, respectively.[59] Graphene devices were exposed to a solution of 4-bromobezenediazonium tetraflouroborate at 300 K in atmosphere. The resulting I-V curve was found to have shifted to the right, indicating p-type doping. In addition, electron mobility was found to be reduced when compared to the as-fabricated device; the hole mobility and minimum conductivity were found to be unchanged. This lack of conductance suppression suggested that there was no significant sp^3 hybridization; Raman imaging suggested that the attachment of diazonium salt was more than simple van der Waals adsorption.

PEI has been known to be an n-type dopant for CNTs. Graphene devices were soaked in a 20 % PEI solution for 3 h at 300 K. Post-soak testing revealed a strong n-type doping along with a conduction asymmetry, this time for holes. Nonequilibrium Green Function (NEGF) modeling was used to explain this phenomenon; it was postulated that the asymmetry is caused by a combination of the Fermi level misalignment at the electrode/channel interface and the nonconstant DOS of the graphene electrodes. It was also predicted that when graphene is doped by metal, conductance asymmetry occurs even of the channel is intrinsic.

Stacks of CVD graphene were p-doped doped with nitric acid.[60] The doping decreases sheet resistance by 3 times, down to 90 Ω/sq for eight layers. HNO_3 doping is thought to occur when electrons are transferred from graphene to nitric acid during for formation of a charge-transfer complex:

$$6HNO_3 + 25C \rightarrow C_{25}^{+}NO_3^{-}\,4HNO_3 + NO_2 + H_2O$$

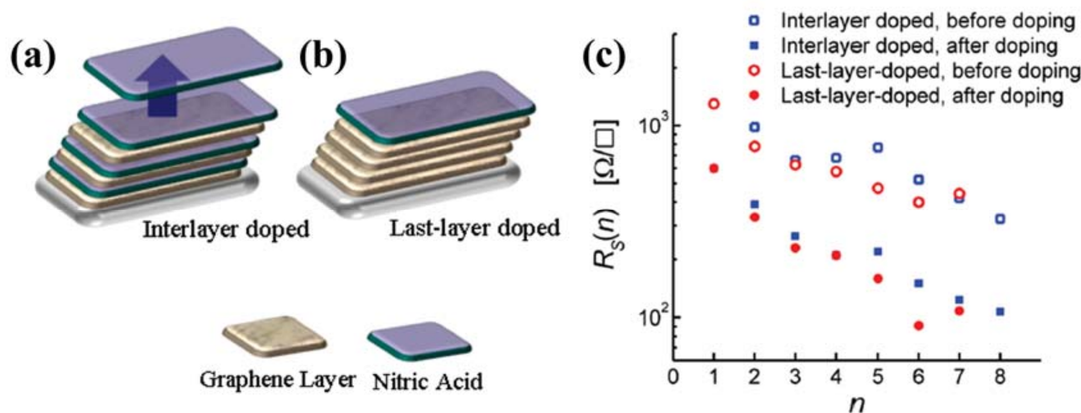

Figure 1.20. Schematic of (a) interlayer doped and (b) last-layer doped graphene stacks. (c) Sheet resistance versus number of layers for both interlayer and last-layer doped cases.[60] Reproduced with permission. Copyright 2010, American Chemical Society.

Two types of doping were demonstrated—"interlayer doped" where doping was performed after etch each layer was stacked, and "last layer doped" where doping was performed after all layers were stacked, in Figure 1.20. Simulations have revealed that the graphene surface acts as a catalytic reducing/oxidizing agent; this drives the chemical disproportionation of adsorbed dopant layers into charge transfer complexes; these complexes then inject carriers into the 2D graphene lattice.

It was shown that CVD graphene can be made p-doped by $AuCl_3$.[61] CVD graphene on PMMA was dipped in a 5 m**M** aqueous solution of $AuCl_3$; $AuCl_3$ is reduced to Au particles by charge transfer from graphene; the surface potential change was studied by Kelvin probe microscopy, and it was found that the potential shift was as much as 0.5 eV within 20 s; after 20 s, the potential saturates, and then slightly decreases beyond 40 s. Au particles were found to aggregate on wrinkles and thicker layers of graphene for less than a 20 s exposure; but for doping tome longer than 20 s, the coverage was more uniform across the graphene surface. In a study of layer by layer doping using $AuCl_3$,[62] it was found that a four-layer stack of CVD graphene can be doped so that the sheet resistance was 54 Ω/sq. In addition, the optical transmittance of the stack was measured to be 85 % at 550 nm wavelength, making it a contender for applications that need a high electrical conductance along with a good optical transmittance.

As-grown epitaxial graphene on SiC, because of the work function difference with the SiC substrate, is n-doped; the Dirac point is 300 meV below the Fermi level. Doping of epitaxial graphene was demonstrated using F4-TCNQ,[63] an electron acceptor. Angle resolved photoemission spectroscopy (ARPES) measurements were used to study doping behavior, and it was found that a 0.8 nm thick layer of the dopant was sufficient to compensate for the intrinsic doping induced by the workfunction difference with the substrate. The dopant

could be applied via wet chemistry and was fairly stable to temperature and light. Photoemission spectroscopy revealed that electron transfer from graphene to F4-TCNQ was responsible for p-doping of graphene.[64] F4-TCNQ has an electron affinity of 5.2 eV; another accepter, C_{60}, was also tried out as a dopant; because of the weaker electron affinity of C_{60} (3.7 eV), only a weak doping of graphene occurs. Gold, bismuth and antimony were also demonstrated to doped epitaxial graphene;[65] the doping was verified by ARPES measurements; it was shown that while bismuth and antimony shifted the Fermi level in the direction of the Dirac point, gold was able to p-dope the graphene, with the Dirac point about 100 meV above the Fermi level.

Chemically derived GNRs were n-doped by ammonia when the GNRs were electrically annealed in a NH_3/Ar mixture at 1 torr.[66] The source-drain bias was swept from zero to a

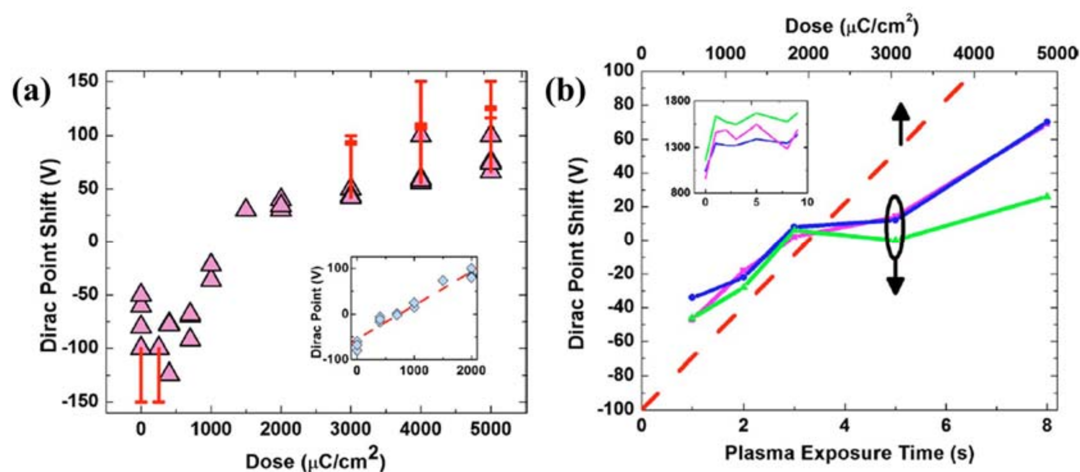

Figure 1.21. (a) Incident e-beam dose versus V_{gmin} shift for a number of flaked graphene devices coated with 30 nm HSQ. For small incident dose, the graphene is n-doped while for large doses the graphene is p-doped. (b) Doping by plasma-induced cross-linking of HSQ. Electrical measurements were performed after 1 s plasma exposures, for three devices. Also shown for reference is the dependence of V_{gmin} shift on incident e-beam dose.[69] Reproduced with permission. Copyright 2010, American Physical Society.

few volts, resulting in a temperature rise of the GNRs due to Joule heating; Raman thermometry revealed that the temperature of the GNRs rose to about 300 ^{o}C. XPS and nano SIMS confirmed the presence of nitrogen in the GNRs; it was postulated that most of the doping occurred at the edges and defect sites since these regions have a much higher chemical reactivity. In addition, similar mobilities before and after NH_3 doping revealed that carrier transport is not degraded by this method.

Hydrogen silsesquioxane (HSQ) has been investigated as a dopant for graphene; an early report speculated that hydrogen released from HSQ resulted in basal plane hydrogenation.[67] HSQ, a well-known spin-on dielectric,[68] also came to be known for its use a high resolution e-beam resist. Thus a doping technique using HSQ can enable high resolution patterning and doping.[69] In the context of its use as a spin-on dielectric, HSQ crosslinking has been found to be a complex transition from a hydrogen-rich cage-like structure to a hydrogen-depleted network-like structure.[70] This transition enables HSQ to function as both a p-type and n-type dopant. Flaked graphene was deposited on 300 nm SiO_2 followed by pattering of contacts. The devices were tested for their electrical response; following this, a 30 nm HSQ layer was spin coated onto the graphene, followed by a 180 ^{o}C bake for 3 min. One set of samples were washed in TMAH, which is normally used as a developer for HSQ. Electrical testing of these samples revealed a strong n-type doping, indicated by a shift of V_{gmin} to large negative voltages. A second set of samples coated with HSQ was exposed to e-beam radiation; a 100 kV beam was used, and the incident dose ranged from 250 to 5,000 μCcm^{-2}. Since as-fabricated devices can have a slight initial doping, the V_{gmin} shift (rather than the absolute V_{gmin}), $\Delta V_{gmin,}$ is used as a metric to gauge HSQ doping. For 250 < Dose <1,000 μCcm^{-2}, ΔV_{gmin} increases from less than -100 V to 0 V. For dose between 1,000 to 5,000 μCcm^{-2}, ΔV_{gmin} increases from 0 V to more than 100 V; saturation is seen in the

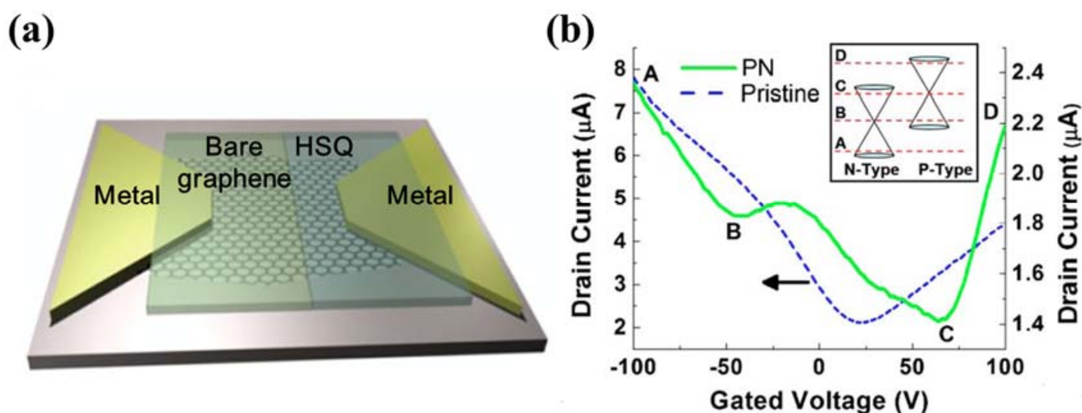

Figure 1.22. (a) Schematic of a graphene p-n junction─one half of the graphene surface is doped p-type and the other half is doped n-type by HSQ. (b) Electrical testing reveals a double dip for the p-n junction; the Fermi level separation is found to be more than 340 meV.[69] Reproduced with permission. Copyright 2010, American Physical Society.

amount of shift induced, in Figure 1.21. This saturation is likely because the cross-linking process is almost complete as dose reaches 2,000 μCcm^{-2}.

In addition to using e-beam irradiation, plasma and thermal treatment were also investigated for doping large areas of graphene with HSQ. Thermal annealing of HSQ as 500 °C is known to induce a structural change; a plasma of energetic ions is better for processes with a tight thermal budget. A set of devices with a HSQ layer dosed with e-beam irradiation at 600 μCcm^{-2} was used to study plasma-induced doping from HSQ. A dose ~ 600 μCcm^{-2} was chosen so that the pre-plasma V_{gmin} was close to 0 V. The devices were taken through an exposure to low power Ar plasma. Short, 1 s flash exposures to the plasma were performed followed by electrical testing. ΔV_{gmin} is initially negative and slowly becomes positive compared to the as fabricated devices, in Figure 1.21; carrier mobility shows improvement at early stages of cross-linking followed by a saturation at longer

exposure times—this indicates that there is little surface damage of graphene as a result of the doping, and there is possibly some compensation of charged impurities, thus actually improving carrier mobility.

The ability of HSQ to dope graphene either p-type or n-type results from a mismatch of bond strengths between Si-H and Si-O bonds in the HSQ, as well as outgassing of H at higher degree of crosslinking. Si-H and Si-O in HSQ have bond strengths of 4.08 eV and 8.95 eV, respectively; at low temperatures (100-200 ^{o}C) or small incident dose (< 300 μCcm^{-2} at 100 kV), Si-H bonds are readily broken, providing hydrogen to bond with the graphene basal plane. Due to the offset in electronegativity, hydrogen acts as an n-type dopant for graphene. Higher degrees of cross-linking in the HSQ film leads to p-doping by two primary mechanisms—Si-O bonds being to break at larger incident energies, and this provides O for adsorption at the graphene surface. In addition, hydrogen is removed from the HSQ film by outgassing. Advanced stages of cross linking leads to HSQ decomposing into SiH_4 and H_2 components. These components escape from the HSQ film, as evident through decreased Si-H to Si-O bond ratio as well as the porous nature of the film. The complementary doping property of HSQ has been used to demonstrate p-n junctions; an as-fabricated graphene flake was covered with a film of HSQ followed by high dose e-beam incidence on one half of the flake—this part of the flake becomes p-doped. The other half was left unexposed, and it thus doped n-type. Back gated I-V measurements revealed a double-dip curve indicating a superposition of two V-curve; one V_{gmin} was at +70 V and the other at - 50 V, in Figure 1.22; the separation between the energy levels on the p- and n-sides was in excess of 340 meV.

1.6 Challenges of SWNTs and graphene technology

In order for the nanotubes to come to the forefront of mainstream commercial use, significant research and development has to continue. There are numerous barriers in the field, and Table 1.1 enumerates only some of the major challenges that need to be addressed. Mainly, new strategies need to be developed to (1) remove metallic nanotubes and purify the semiconducting mixture of CNTs and (2) assemble nanotubes with controlled pitch and placement. Besides these material challenges, developing new processing and device fabrication technologies will be the key for enabling self-aligned transistors with low parasitics and high performances.

Depending on the maturity of the SWNT fabrication process in the future, SWNTs may be used in ICs either by themselves (homogeneous) or in a hybrid (heterogeneous) configuration. However, regardless of the approach, it is envisioned that Si will remain as the main substrate for processing, mechanical support, and heat transfer with the carbon nanotubes serving as a thin layer of high mobility material for active and/or passive elements.

Table 1.2. Major challenges for device/circuit fabrication with SWNTs

Challenges and future tasks
1. Chemically doped SWNTs with air-stable and robust molecular species to make unipolar devices for traditional circuits
2. Produce/synthesize highly pure carbon nanotubes with deterministic diameter and chirality
3. Fabricate dense and regular arrays of nanotubes to achieve high current drive capability with high packing density
4. Fabricate complementary devices
5. Develop self-aligned device strategies
6. Reduce parasitics and optimize the device structure
7. Develop ohmic, nano-scale contacts to SWNTs
8. Heat removal and managing the high power density

Graphene transistors based on traditional FET structures are attractive due to the high carrier mobility. Considering progress to date, graphene FETs are more suitable for radio frequency (RF) applications since they do not require a bandgap. For digital applications, it remains to be seen if graphene FETs with bandgap can outperform Si FETs. A number of device related challenges need to be addressed before graphene FETs can be integrated into mainstream circuits; these include doping, contact resistance, and scattering from edge, dielectrics, and substrate.

1.7 Objective and organization of this thesis

Nanotechnology research can impact the semiconductor industry either by directly integrating high mobility nanoscale devices and circuits, or by impacting the scaling of silicon CMOS technology by for instance, self-assembly and lower manufacturing cost. Many groups have shown that graphene- and SWNT-FETs provide a number of performance advantages over Si MOSFETs throughout experiments and/or simulations. Without discussion either explicitly pessimistic or optimistic about the future of graphene- and SWNT-FET technology, the state of the art manufacturing process of graphene- and SWNT-FETs was far from what the simulations promise. Significant technological advances, including removal of metallic tubes, reliable growth of well-ordered arrays, maintaining control on the diameter and chirality, graphene with bandgap are only a few the breakthroughs necessary to make this technology mature enough for the semiconductor industry to adopt.

Widely known is that obtaining both p- and n-type materials and controlling their charge carriers are crucial to the current microelectronics including nanocarbon materials. With graphene and carbon nanotube, FET exhibits ambipolar behavior with high mobility compared to silicon devices. However, graphene and carbon nanotube show p-type behavior

with holes as the majority carriers in air due to oxygen and/or water molecules. The ability to tune graphene and SWNTs into both n- and p-type should be important to their applications in molecular electronics. The major carrier types in graphene and SWNTs can be enhanced or converted by chemical and/or non-chemical doping methods. Long term stability can further enable us to fabricate basic logic circuits under ambient conditions.

The objective of this thesis is related with the solutions of issues on tuning the electrical properties of nanocarbon materials. For more details, it is to develop methods to realize stable n-type graphene FET, and to explore the as-grown nitrogen-induced HASWNT FET properties.

The organization of this thesis is as follows:

After the brief introduction to graphene and SWNTs in this chapter, the main results of my PhD research are presented from Chapter 2. Chapter 2 discusses a controllable n-type behavior graphene FET using polymer thin films. A possible mechanism of this doping is proposed, based on the electrical transport property with consistency of polymer solution.

Chapter 3 presents an electric property of as-grown nitrogen-induced HASWNT, which is a similar work in chapter 2 even though it is a different material and method. Based on the previous theory results, nitrogen atom can be affected electrical properties as configuration of nitrogen atom on the carbon nanotubes. From these, nitrogen-induced HASWNT was grown and characterized to apply integrated circuit with CNTFETs.

Closing remarks of the whole thesis are presented in Chapter 4, including the summaries, highlights, degree of objective fulfillment, and perspectives.

Chapter 2

Highly stable n-doped graphene field-effect transistors with polyvinyl alcohol films

In this chapter a protocol to exceedingly stable n-type graphene FETs under ambient air condition is presented. The intrinsic p-type behavior of graphene field-effect transistors (FETs) in ambient condition exhibits a main challenge for the assembly of complex electronic devices such as integrated circuits (ICs). This part presents a protocol of tunable n-type doping for graphene FETs via polyvinyl alcohol (PVA) coating. Using high-quality graphene grown from alcohol catalytic chemical vapor deposition, functionalization of its surface by this hydroxyl anion-rich polymer results in an evolution of the FETs from p-type to ambipolar or n-type even under ambient condition. The doping level of graphene is strongly related with the treatment procedures of the PVA film, such as solution concentration, hardening temperature and hardening time. This PVA coating proves to be a simple and stable approach of tuning the Dirac point and doping level of graphene, which is highly desirable and of great significance in the future graphene-based electronic devices.

2.1 Background and motivation

There have been many advantages of using graphene for electronic and optoelectronic devices due to its outstanding electrical, mechanical, and optical transparent properties.[71-73] Its many physical and electrical properties, such as extraordinarily high carrier mobility (up to 200,000 $cm^2V^{-1}s^{-1}$),[74] ballistic transport distance up to 1 μm,[75] half-integer quantum Hall effect,[76,77] superior mechanical elasticity,[78] open up possibilities as a promising candidate to substitute silicon in the next generation electronics. However, the full potential of graphene in device industry is still restricted by several challenges. For example, it is crucial to open a bandgap in graphene to realize the "ON" and "OFF" states in electronic devices. Solutions to this challenge involve tailored nanoribbon structure,[79-82] bilayer graphene with a vertical electric field,[31,83-85] graphene nanomeshes,[86] etc. Moreover, due to the fact that ambient condition makes graphene behave as p-type semi-metal,[49] to facilitate the electronic transport properties in graphene-based devices, the positive and negative carrier concentrations of graphene must be adjusted by shifting the Fermi level away from its Dirac point, so that the device can also behave as n-type and be assembled into circuits.[7,87] Several approaches to locally change the carrier density have been explored using different dopants, such as gases, alkali metals, polymers, and so on.[48,49,58,87,88] However, these approaches show disadvantages in device fabrication, such as difficult to process or pattern, or low device stability and so on. For instance, potassium doping has led to the fabrication of n-type graphene field-effect transistors (FETs) and enabled the integration of more complex devices such as intra-graphene p-n junctions with different device functions.[89] However, such alkali dopants suffer from immediate degradation upon exposure to air, making them unapplicable for n-type doping of graphene in practical device applications.

In this section, a protocol of tunable n-type doping of graphene by functionalizing its surface with PVA film is presented. Using high-quality graphene grown from alcohol

catalytic chemical vapor deposition (ACCVD), functionalization of its surface by this hydroxyl anion-rich polymer results in an evolution of the FETs from p-type to ambipolar or n-type. The doping level of graphene is strongly related with the treatment procedure of the PVA film, such as the solution concentration, spin-coating speed and hardening time. This PVA coating proves to be a simple and stable approach of tuning the Dirac point and doping level of graphene, and this environmentally free n-type doping enable us to fabricate more complex electronic devices such as p-n junction diodes, complementary inverters, and numerous complicated logic circuits.

2.2 Experimental

2.2.1 Growth and Fabrication of graphene FETs

The graphene used in our study was produced by ACCVD using a copper foil enclosure, as described in our previous work as shown in Figure 2.1.[90] For more details, the copper substrate was first cleaned by hydrogen chloride (HCl), acetone and isopropanol (IPA) sequentially to remove protection layer. To smooth the metal surface and remove metal oxides, the copper substrate was annealed at 1000 °C for 20 min in Ar/H_2 (3 %). The graphene growth was at 1000 °C with 10 sccm ethanol flow diluted by 300 sccm Ar/H_2, and

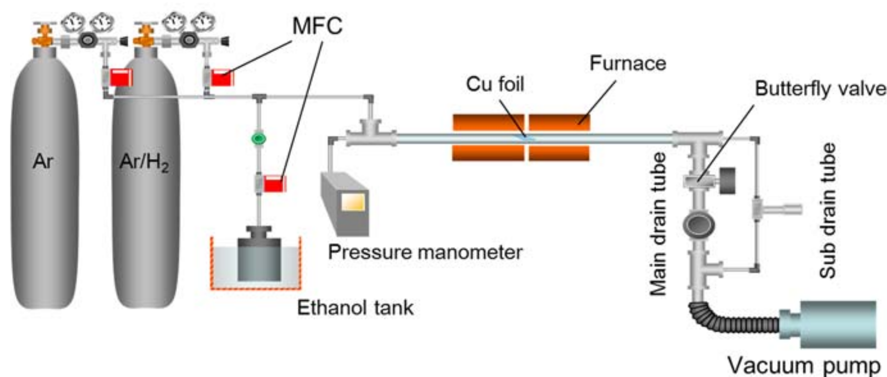

Figure 2.1. Schematic illustration of alcohol catalytic chemical vapor deposition.

the growth time was 10 min.[90] Uniform monolayer graphene was obtained on the inside surface of the copper enclosure. As to device fabrication, the source/drain electrodes were firstly patterned on a Si/SiO_2 (600 nm) substrate using a standard photolithography process as shown in Figure 2.2 and Figure 2.3. The 40 nm/10 nm thick Au/Ti electrodes were deposited in high vacuum condition using a thermal evaporator (ULVAC VPC-260F) with a quartz crystal thickness meter (CRTM-6000). As-grown graphene was then transferred by poly(methyl methacrylate) (PMMA) (average molecular weight ~ 950k, Sigma-Aldrich) 4 % in anisole onto this substrate with predefined electrodes, similar as a process reported previously.[91] The PMMA layer was then removed by acetone, followed by annealing the device at 350 °C for 3 h under vacuum condition. Subsequently, the second photolithography step was adopted to remove graphene film exclusive of channel region by

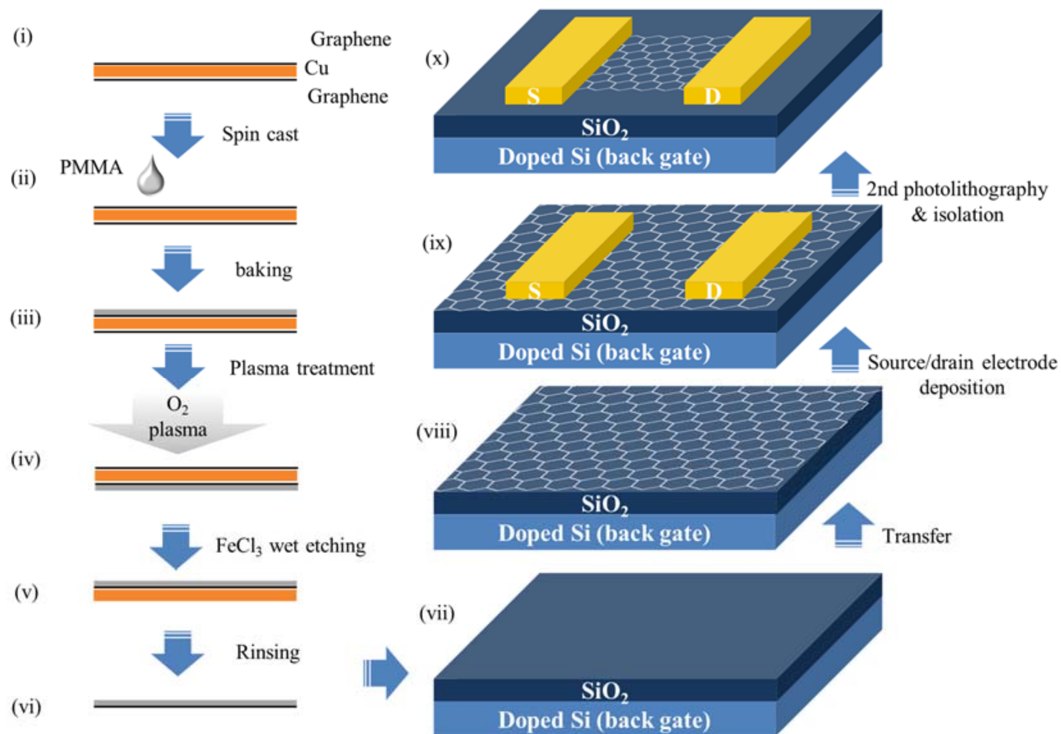

Figure 2.2. Experimental procedures of graphene transfer and monolayer graphene field-effect transistors.

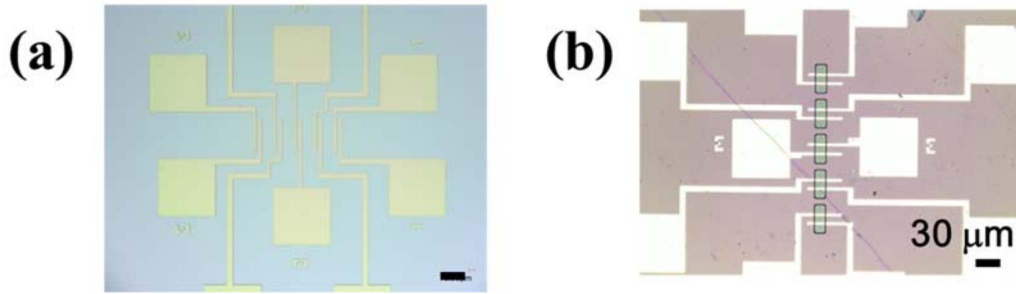

Figure 2.3. Optical micrograph of fabricated device array. (a) Optical image after first photolithography process. (b) Optical image after second photolithography process.

exposing the substrate oxygen plasma (100 W, 100 Pa) for ~ 1 min as shown in Figure 2.3(b).

2.2.2 Electrode array formation

A p-type silicon wafer with oxide layer (t_{ox}: 600 nm) was used as a substrate. Figure 2.4 shows a flow diagram of a manufacturing process:

(1) After standard dry/wet cleaning substrate, OAP as an adhesive layer spin coating (3000 rpm, upTM 3.0 sec, runTM 30.0 sec).

(2) Positive photoresist (JSR) spin coating over the layer (3000 rpm, upTM 3.0 sec, runTM 30.0 sec).

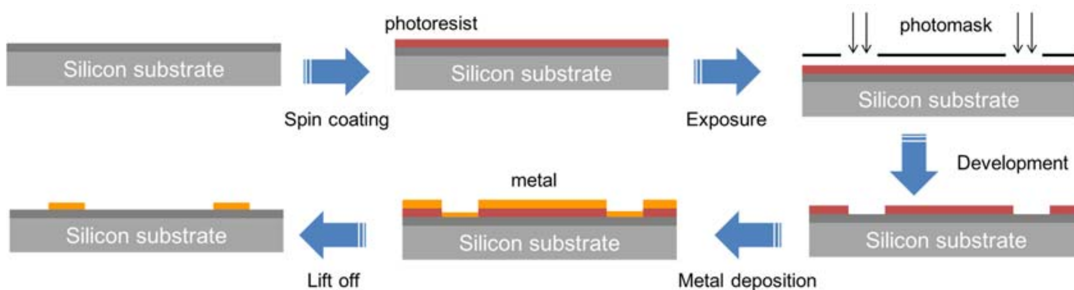

Figure 2.4. Process steps for graphene-FET fabrication.

(3) Exposure with photomask, after soft baking (110 ^{o}C, 90 sec).

(4) Pattern formation soaked in the developer (Tetramethylammonium hydroxide, TMAH) for 60 sec.

(5) Lift-off after being deposited as an electrode by vacuum deposition to remove the excess metal.

2.2.3 Characterization of graphene field-effect transistors

After the fabrication of graphene FETs, the devices were characterized by semiconductor parameter analyzer system (Agilent 4156C) at ambient condition as shown in Figure 2.5., scanning electron microscope (SEM, acceleration voltage at 5 kV, S-4800, Hitachi), ultraviolet-visible-near infrared (UV-vis-NIR) spectroscopy (UV-3600, Shimadzu Co. Ltd.), and micro-Raman spectroscopy (Raman-11 system, inVia Renishaw).

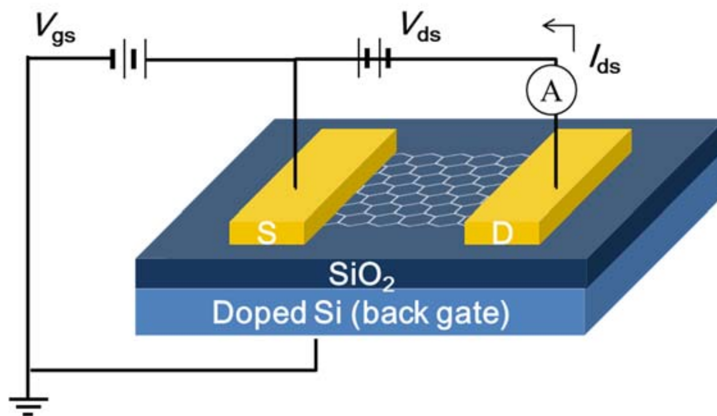

Figure 2.5. Schematic diagram of a back-gated graphene FET measurement.

2.3 Result and discussion

2.3.1 Properties of as-grown CVD graphene

Figure 2.6(a) presents the SEM image of as-grown graphene on the inside copper surface of the enclosure. The graphene film shows uniform high quality, as demonstrated by scanning

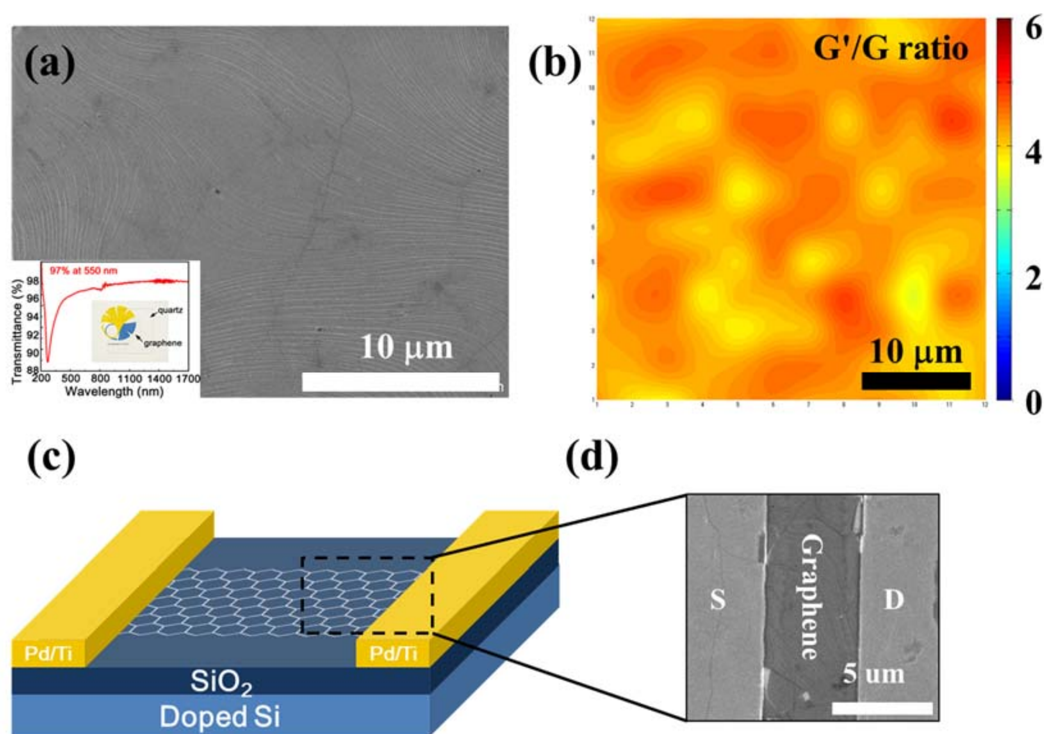

Figure 2.6. (a) SEM image for as-grown graphene on copper substrate via ACCVD. (b) Intensity ratio of G' to G band of scanning Raman spectroscopy using an excitation energy of 514.5 nm (2.41 eV). (c) The schematic of as-grown graphene field-effect transistors with source, drain, and gate electrodes. A 600 nm SiO_2 was used as an insulator layer. (d) The corresponding SEM image of graphene on silicon substrate between the source/drain electrodes after transferred.

Raman map in Figure 2.6(b). The number of active graphene layers were determined from the intensity ratio between Raman G'- to G-band ($I_{G'}/I_G$), which exhibits a large value of ~ 4. Only small disorder band is visible in the Raman spectra (see also Figure 2.7(a)), which proves a high quality monolayer of graphene.[19] Its full width at half maximum (FWHM) was 32 - 35 cm^{-1} in our as-grown graphene, consistent with the value reported for monolayer graphene. The Figure 2.6(c) and 2.6(d) illustrate the schematic and SEM image

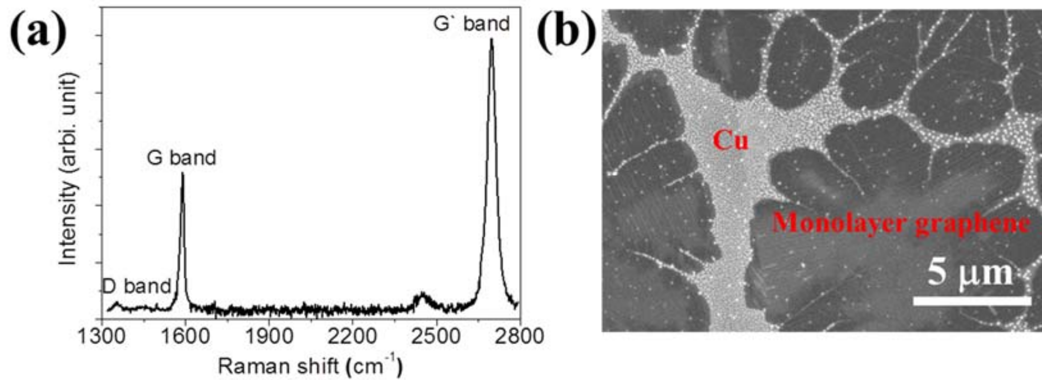

Figure 2.7. (a) Raman spectroscopy using an excitation energy of 488 nm (2.54 eV) for as-grown LPCVD graphene on SiO_2/Si substrate. (b) Graphene domain grown at 1000 ^oC on Cu an average growth rate of ~ 50 μm per 30 seconds.

of as-grown graphene FETs on silicon substrate with a bottom gate. Very low pressure CVD (LPCVD) process can grow graphene with large domains of up to ~ mm in size, which has been found to be harmful to the transport properties.[92] The mechanism of the degradation still remains obscure, but what is known is that structural defects promote surface reactions with adsorbates from ambient or other defects some of which are induced by the transfer process.[93] From previous work, electrical transport properties showed that graphene films with large domains have higher mobility than those with small domains predominantly. The size, number, and surface coverage of as-grown LPCVD graphene domains/islands as a function of growth time are observed and domain size was limited to a few tens of micrometers as shown in Figure 2.7(b).[90] The quality of the graphene films will be also evaluated by measuring the transport properties of the graphene transferred onto SiO_2/Si wafers later.

PVA was formerly an encouraging material as polymer dielectrics in flexible devices or

alignment layer in liquid crystal applications because of its high dielectric constant ($\kappa \sim 6$), good surface alignment effect, photosensitivity, and good resistance to damage by solvents involved in the lift-off process up to this time.[94-97] We have examined the doping effect of the graphene devices with PVA coating by preparing an as-grown graphene on SiO_2/Si substrate and measuring its gate response to different polymer film conditions, such as annealing time, temperature, and polymer concentration. The functionalization of graphene surface by hydroxyl group-rich polymers leads to the conversion of graphene FETs from p-type to n-type or ambipolar. Thus, doping by functional groups of adsorbed polymers on graphene presents a simple means of changing the doping level. For the first time, we achieve n-type graphene FETs that are stable under air without keeping the graphene in a vacuum condition or an inert environment. This will be discussed in more detail in the Raman spectroscopy part later.

We demonstrate that the adsorption of PVA on graphene results in a negative shift of the Dirac point. Similar phenomena was also reported by our previous result for single-walled carbon nanotube FETs, and graphene using poly(ethylene imine) (PEI) from other groups.[59,88,98] However, the neutrality point of as-grown graphene devices was a surpassing position gate voltage range, for instance, from -100 V to 100 V because the as-grown graphene was heavily p-type doped, as shown in Figure 2.8(a). The reason is that the adsorption of water molecules and/or oxygen or unintentional contamination during the fabrication procedures can affect the electrical properties of as-grown graphene, as shown in Figure 2.8(b). The intrinsic Fermi level of graphene is downshifted to the valence band when graphene is exposed readily to ambient air condition, as indicated in the schematic illustration shown in Figure 2.8(c). Prior to PVA dopant applied, we always characterized if the transfer curves of our as-transferred LPCVD graphene transistors (channel: L = 10 μm;

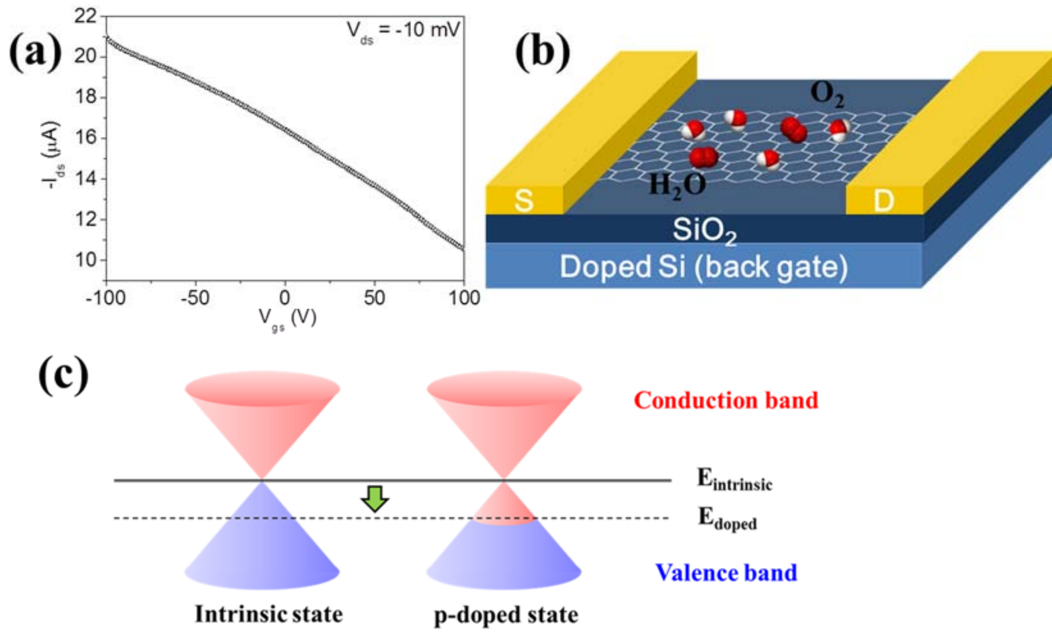

Figure 2.8. (a) Corresponding transfer (I_{ds}-V_{gs}) characteristics of as-grown graphene device. (b) Water, oxygen, and/or residues adhere on graphene surface. (c) Schematic illustration of the Fermi level shift of monolayer graphene in air.

W = 50 μm) were comparable with each other to confirm the quality of initial graphene was at the similar level show p-type transport behavior with highly positive Dirac points of > 40 V, as shown in Figure 2.8(a).

2.4 PVA-coated graphene devices

2.4.1 Fabrication of PVA-coated graphene FET

The PVA solution was prepared by dissolving 1, 10, and 20 wt % PVA powder (average molecular weight ~ 1,500; Wako) in distilled water, respectively. First of all, the DI water is kept in the refrigerator at least for 1 hr, and PVA powder was dissolved in DI water by stirring with a magnetic stirrer at 350 rpm for few hours at 90 ^{o}C. Followed completely

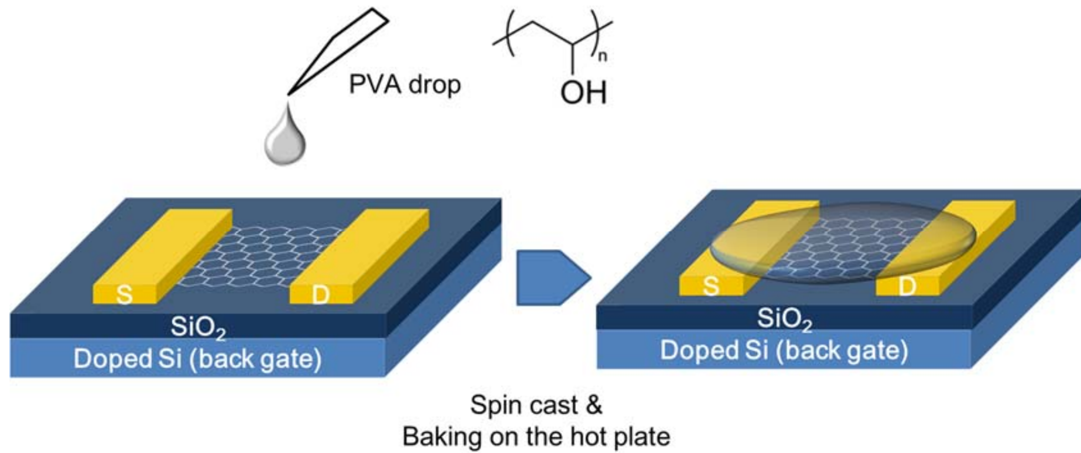

Figure 2.9. Process steps for PVA-coated graphene device.

dissolved PVA solution, the solution keep in the bath-type sonication about for 10 hrs to remove some bubble in the solution. The polymer thin films were formed on the graphene channel by spin-coating the solution at 2000 rpm for 60 s, followed by baking at 60–150 ^{o}C for 10–30 min as shown in Figure 2.9.

2.4.2 Transfer (I_d-V_g) characteristics of PVA-doped graphene FETs

This is illustrated in Figure 2.10(a) and (b), where the transfer curves (I_{ds}-V_{gs}) before and after 10 wt% PVA (PVA-10W) exposure exhibits a shift of the neutrality point to more negative gate voltages under ambient conditions compared to pristine transistor. After spin casting of 10 wt% PVA solution on graphene, the Dirac point of the graphene transistors was shifted around 5 V indicating the n-type doping effect of coated PVA film on monolayer graphene. The hole conduction was suppressed with respect to the gate voltage in the negative bias region, whereas the electron conductance in the positive biased region was increased with ambipolar behavior. The electrical conductivity of PVA film is negligible because PVA is an insulator polymer. Hence the observed unipolar p-type to

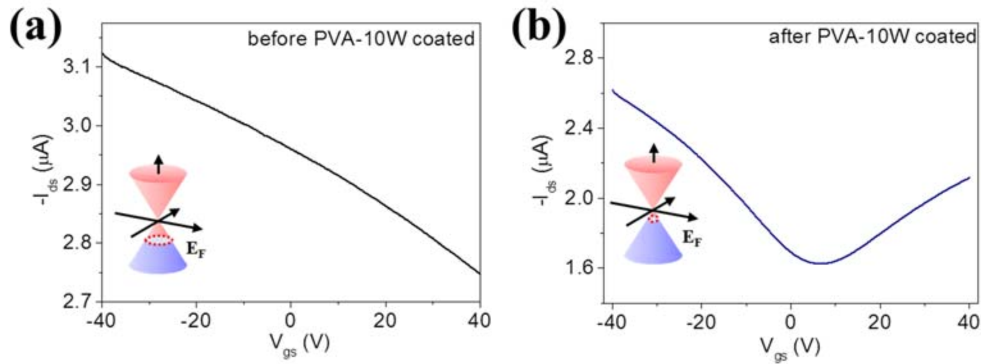

Figure 2.10. Electronic transport properties of as-grown ACCVD graphene devices. (a) Transfer characteristics before PVA-coated graphene device under ambient condition (Channel length = 10 μm; width = 10 μm; V_{ds} = -10 mV). (b) Transfer characteristics after PVA-10W coated ACCVD graphene transistors in air**.**

ambipolar conversion comes from modification of the graphene channel induced by PVA in the film as hydroxide ions are electron donating. The doping-induced electric transport asymmetry shown in Figure 2.10(b) is caused by a combination of the neutrality point misalignment at the electrode/channel interface and the nonconstant density of states of the graphene electrodes.[59]

The observed phenomena result from the effective carrier density modulation in the graphene by the PVA thin film is proposed. As a strict 2D electronic system, a capacitor model has been effective and frequently adopted to describe transport in SWNT and graphene FETs.[99,100] For the weak dependence of carrier mobility on carrier density in graphene,[101] the conductance change is approximately proportional to the change in carrier density that is linearly modulated by an external gate voltage. The coating of the PVA film on the graphene surface breaks the linear relationship between the increase of

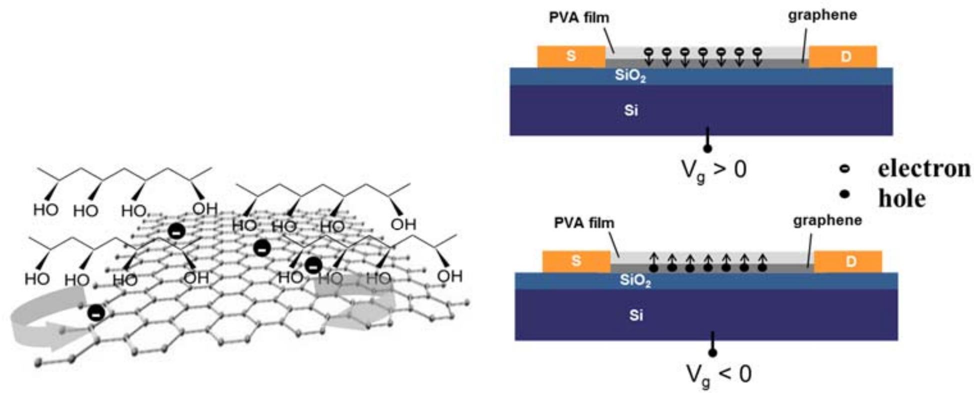

Figure 2.11. Schematic of carrier migration at the PVA film and graphene interface.

carrier-density and the gate voltage as described in a simple capacitor model by introducing as additional carrier injecting/withdrawing source. As the hydroxyl groups in PVA is effective electron donors since they bear lone pair electrons, electron carriers from these sites are pulled into the graphene by the downward electric field induced by a positive back gate voltage in Figure 2.11., resulting in a sudden increase in electron density and hence conductance increases. Meanwhile, hydroxide is electronegative and can serve as effective hole traps. The increased hole carriers generated by a negative back gate voltage are pull into the PVA layer and trapped by the hydroxide ions in Figure 2.11. Since there is a finite number of hydroxide near the graphene, the carrier modulation is also expected to be finite. This is seen in Figure 2.10(b).

2.4.3 Temperature effect of PVA-doped graphene FETs

The hardening temperature that can affect on the transport behavior of graphene FETs with 10 wt% PVA solution is also found as another factor. As shown in Figure 2.12(a), similar heavily p-type unipolar to ambipolar conversions were observed when using different baking temperature. The Dirac point of graphene device changes as temperature increases,

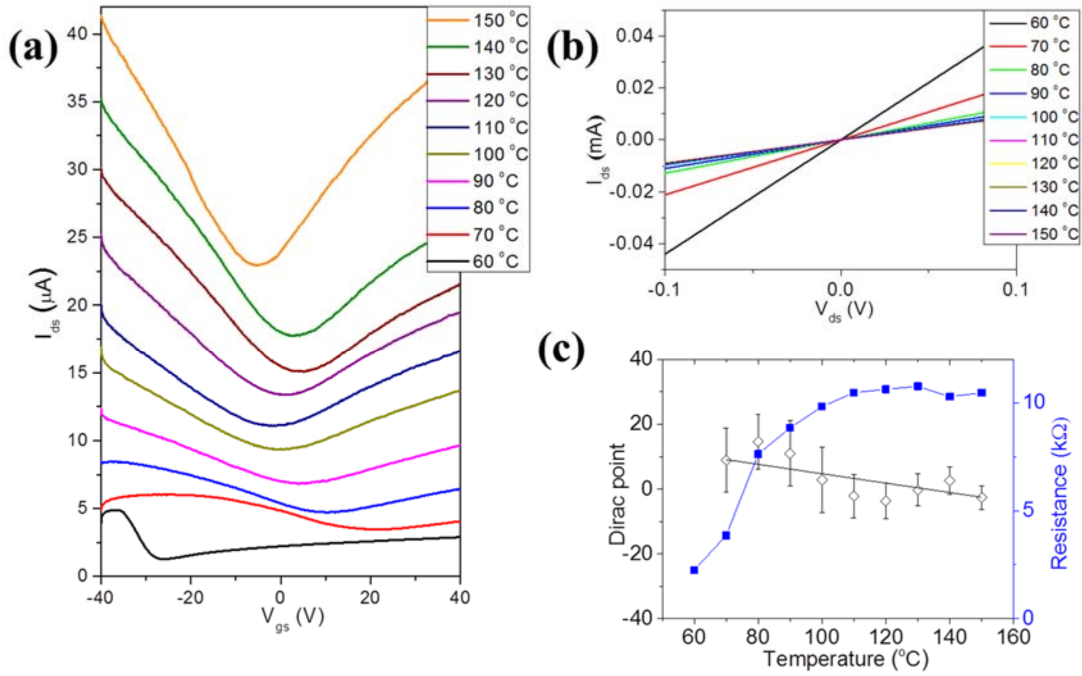

Figure 2.12. I-V characteristics of PVA-10W doped graphene transistors. (a) Corresponding I_{ds}-V_{gs} characteristics of PVA-10W coated graphene devices as a function of different hardening temperature for 10 min. Drain current are shifted for clarity. (b) Dirac point position depends on diverse hardening temperature. (c) The corresponding I_{ds}-V_{ds} characteristics as a function of different hardening temperature.

for instance, the corresponding transfer curves (I_{ds}-V_{gs}) of graphene FETs are gradually shifted from 20 V when it is hardened at 70 ºC to -7 V at 150 ºC. Figure 2.12(b) and 2.12(c) show the Dirac point shift as a function of baking temperature with error bar and source-drain currents modulation with various temperatures, respectively. We can also straightforwardly tune the Fermi level of the graphene using coated PVA films with different hardening time, as shown in Figure 2.13(a)-(f). The Dirac point of PVA-doped graphene transistors induced a down-shift compared to that of the as-grown graphene at first,

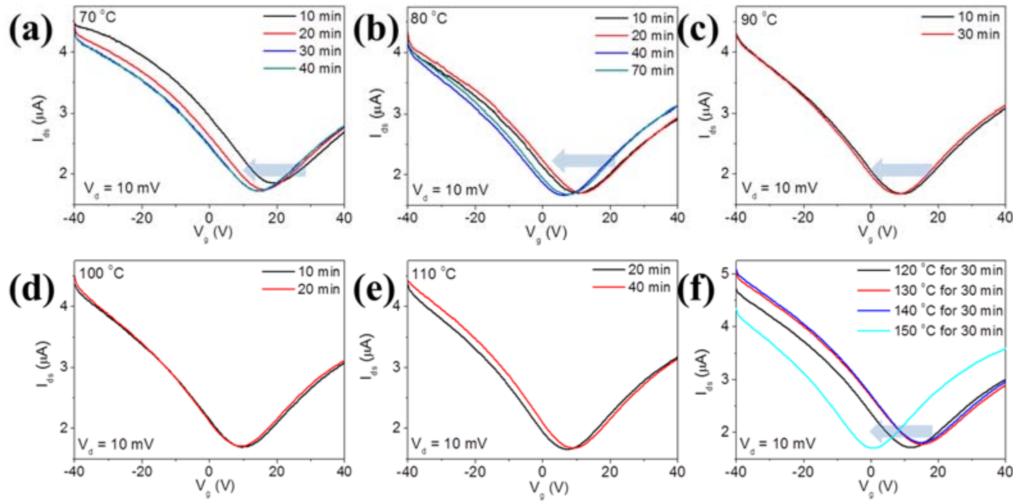

Figure 2.13. I_{ds}-V_g characteristics of PVA-10W doped graphene transistors with different baking temperature and time.

and then saturated around zero gate voltage when the baking time increases. Results show that the hardening temperature and time can administer the Dirac point of graphene devices.

2.4.4 Electron-donating ability of PVA for GFET

To estimate the electron-donating ability of PVA, we compared the Dirac point shifts between devices based on different concentrations of PVA solution. Because PVA consists of anion-rich groups, which is presumably electron-donating, we considered only anion molecules adsorbed on graphene. Prior to PVA coating, we first confirmed the transfer characteristics of all as-grown graphene transistors were the quality and doping level. As the extension of PVA concentration, the neutrality point of graphene device is readily shifted to negative gate voltage i.e. n-type electrical switching behaviors, because of electron transfer to graphene surface from coated polymer films. The transfer (I_d-V_g) characteristics of 1 wt% PVA (PVA-1W) doped graphene field-effect transistors as a function of gate voltage for

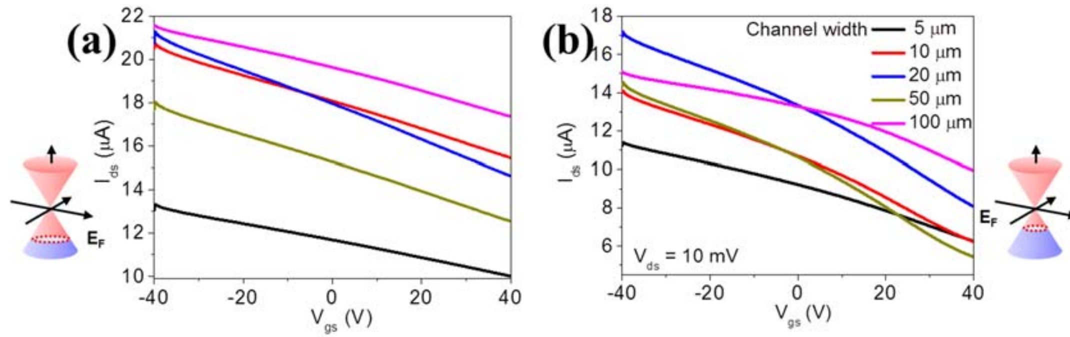

Figure 2.14. (a) Transfer curves of as-grown graphene transistors before PVA-1W doping. (b) I_{ds}-V_{gs} characteristics of PVA-1W doped graphene devices as a function of gate voltage for different channel widths.

varying channel widths do not significantly change when compared with that of pristine graphene although current level down-shifted relatively in Figure 2.14(a) and 2.14(b), respectively. Low concentration of PVA solution, for instance 1 %, is not enough to convert not only to ambipolar but also to n-type for electrical behavior of the graphene devices. On the other hand, the transfer characteristics of 20 wt% PVA (PVA-20W) coated graphene devices as a function of gate voltage for varying channel widths convert to n-type from p-type behaviors as shown in Figure 2.15(a) and 2.15(b), respectively. For this particular sample, it resulted in a drop in the sheet resistance down to compared with pristine graphene.

2.4.5 Charge transfer evidence between PVA and graphene

To confirm the n-type doping effect of PVA on as-grown graphene films and derive a better understanding of the interfacial electron transfer, we performed Raman spectrum measurement on these graphene FETs. We characterized both the as-transferred and doped graphene films with different concentrations of PVA solutions and compared their Raman spectrum features. The G-band and G'-band positions of as-grown graphene are ~ 1584 cm^{-1}

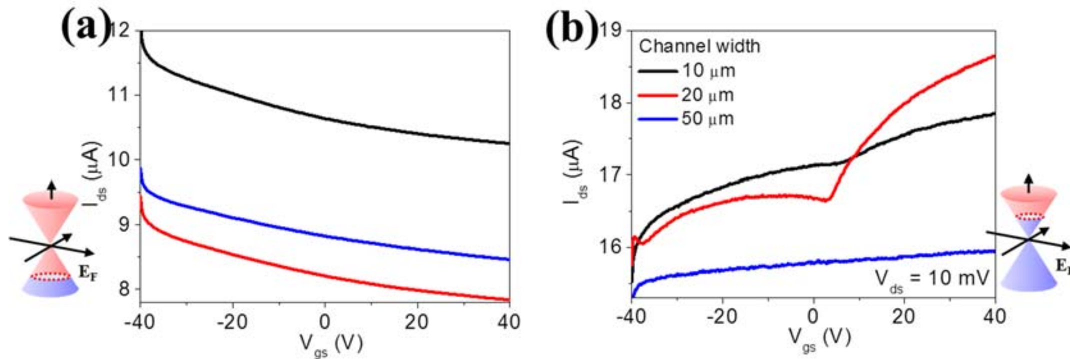

Figure 2.15. (a) Transfer curves of as-grown graphene devices before PVA-20W doping. (b) Transfer characteristics of PVA-20W doped graphene transistors as a function of gate voltage for varying channel widths.

and ~ 2700 cm^{-1}, respectively.[102] Previous reports for in situ Raman measurements using gate tuning of Dirac points found that the G-band position of graphene upshifts for both n-type and p-type doping.[103,104] On the other hand, the G'-band downshifts with heavy electron donation, and the G' to G-band intensity ratio has a strong dependence to the doping level. As to our graphene devices, the as-grown graphene shows a slight upshift of G-band position due to unintentional p-type doping by oxygen and other impurities from transfer process in Figure 2.16(a). After doped with a small amount of PVA (PVA-1W), the graphene G-band starts to downshift to lower wavenumbers, indicating a doping effect that is consistent with the observed conversion from p-type to ambipolar. As the PVA concentration increases, the G-band position upshifts as the graphene FET becomes n-type, which was also observed for doping by gate tuning. The evolution of G-band FWHM is opposite to that of the G-band position, which exhibits a narrowing the line width for both electron and hole doping as shown in Figure 2.16(b). Moreover, the change in G'-band

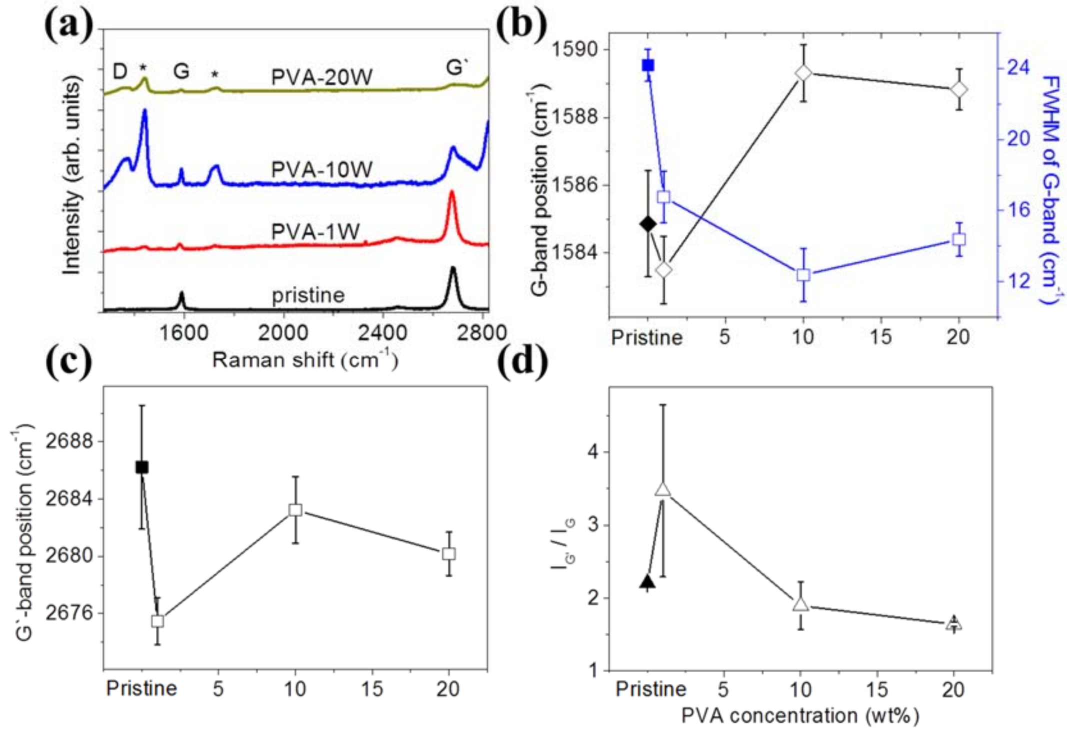

Figure 2.16. (a) Raman spectra of graphene monolayer on SiO_2/Si wafer doped with various concentrations of PVA solutions, for instance, PVA-1W, -10W, and -20W. The intensity of G'/G ratio was more than twice, while the peak position of G and G' band is ~ 1584 and 2688 cm^{-1}, respectively. (b) G-band position and its FWHM in terms of PVA contents. (c) G'-band shift as a function of PVA concentrations. (d) Intensity of G'-band to G-band ratio depend on the various concentrations of PVA.

position is smaller than that in G-band position in Figure 2.16(c). Another important parameter to estimate the doping level is the intensity ratio of G' to G-band. $I_{G'}$ to I_G shows a strong dependence on the PVA doping concentration, as shown in Figure 2.16(d).

2.4.6 Mobility before and after PVA doping of GFETs

The transfer curve of a typical as-grown CVD and PVA coated device is respectively shown in Figure 2.17(a) and 2.17(b) with higher hole and electron mobilities of ~ 1116 $cm^2V^{-1}s^{-1}$

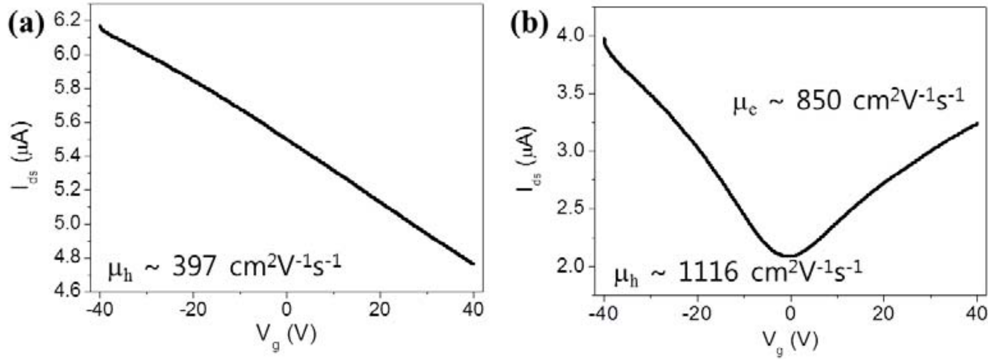

Figure 2.17. I_d-V_g characteristics before and after PVA-10W coated graphene devices under ambient conditions (V_{ds} = -10 mV). (a) Transfer curve for as-grown CVD graphene transistor. (b) Transfer curve for PVA-10W coated graphene devices under ambient air condition.

and ~ 850 $cm^2V^{-1}s^{-1}$ compared with as-grown graphene FETs (hole mobility of ~ 397 $cm^2V^{-1}s^{-1}$), calculated from the transfer curves (I_d-V_g). The field-effect mobilities of electrons and holes were derived from the slope of source-drain current variation from gate voltage to the linear regime using the equation $\mu = \frac{L_c}{WCV_d}\frac{\Delta I_{ds}}{\Delta V_{gs}}$. Here L_c and W are the channel length and width, $(\Delta I_{ds})/(\Delta V_{gs})$ is the transconductance, C is the gate capacitance, and V_d is the source-drain voltage. The hole mobility for PVA-10W coated graphene devices (2200 $cm^2V^{-1}s^{-1}$) showed ~ 2 times that of the as-grown GFET (1260 $cm^2V^{-1}s^{-1}$). Both type conversion and the changed mobilities are reproducible in many graphene FETs that were independently prepared, as shown in Figure 2.18(a) and 2.18(b).

2.4.7 Stability for PVA-coated graphene devices

Figure 2.19(a) show that the Dirac point of the PVA-10W doped graphene transistors

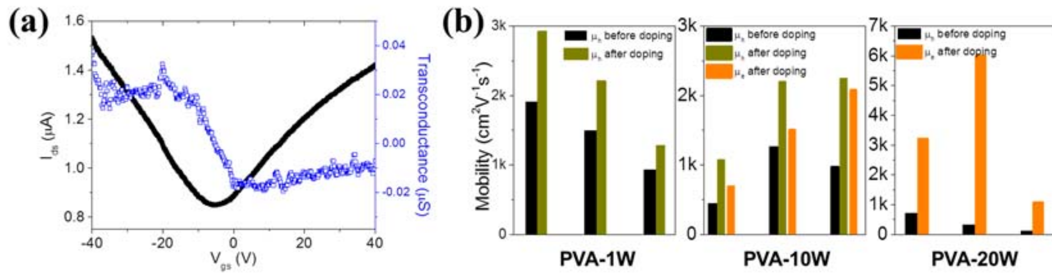

Figure 2.18. (a) I_{ds}-V_{gs} characteristics and transconductance as a function of gate voltage for PVA-10W doped graphene transistors (V_{ds} = -10 mV). (b) Hole and electron mobility before and after PVA-1W, -10W, and -20W coated graphene devices as a function of different channel widths, respectively.

significantly was shifted from > 40 V to about -20 V after 7 days. A PVA-10W doped graphene device was left under ambient conditions for up to one month, and its Dirac voltage move to positive gate voltage but the n-type doping behavior was still preserved, as show in Figure 2.19(a). The air stability of a PVA doped graphene transistor was monitored by measuring the performance as a function of time, in which graphene was doped with a solution concentration of 10 wt% in distilled water and monitored for more than 30 days. After more than 30 days, the Dirac point of these graphene devices that we kept in ambient was not shifted to over 0 V and sill exhibited ambipolar behavior, indicating that the doping with PVA was still effective in air to donate electrons to the unintentional p-doping of graphene and recover its expected ambipolar behavior for pristine graphene, in Figure 2.19(b).

The Dirac point of graphene is controlled by the density and character of its charge carriers.[65] A drawback of chemical doping is the return of an n-type FET to p-type when

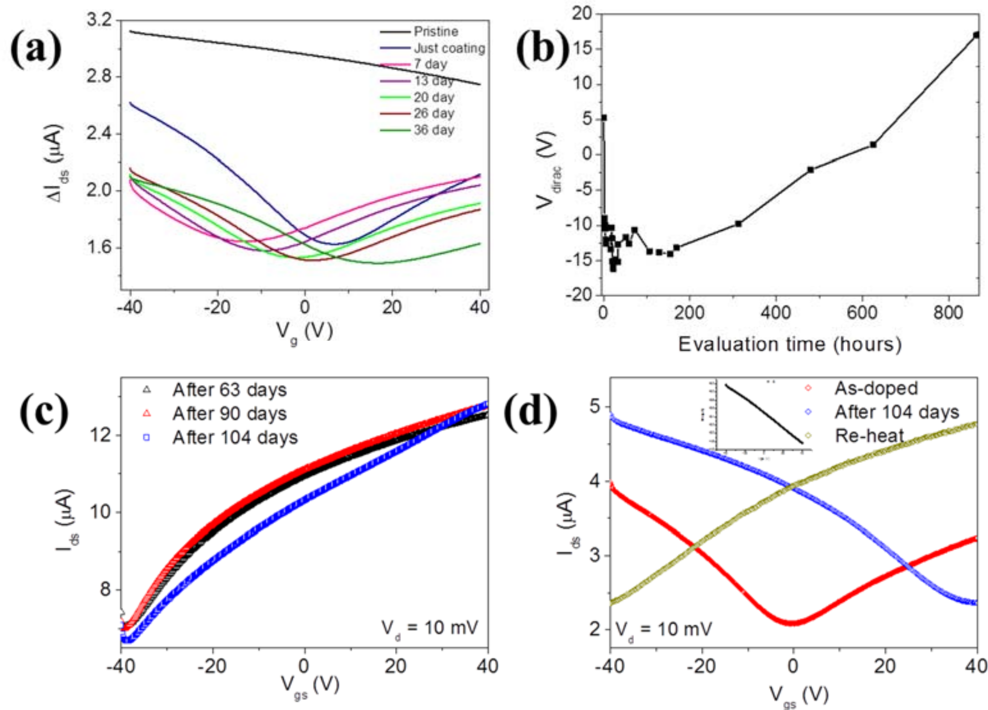

Figure 2.19. (a) Transfer curves of PVA-10W doped graphene FETs as a function of time. (b) Dirac point of PVA-10W GFET as a function of evaluation time. (c) I-V characteristics of as-grown, PVA-20W doped, after 104 days, and re-heat treatment graphene devices, respectively. (d) I_{ds}-V_{gs} characteristics of PVA-10W doped, after 104 days, and re-heat treatment graphene FETs (that of the as-grown graphene device in inset).

exposed to air, because the dopants are readily oxidized and lose their ability for n-type doping. For instance, inorganic (NO_2)[105] and organic molecules (amines)[59] doped graphene FETs exhibit n-type behavior in vacuum, but readily change to a p-type behavior on exposure to air. PEI, which contains an amine group, leads to doped graphene FETs that exhibit n-type behavior with a relatively high on/off ratio, but again changes back to p-type under ambient conditions. The I_d-V_g characteristics of a heavily doped device was slightly reduced but n-type doping behavior maintained under ambient conditions, as shown in

figure 2.19(c). This long term stability in PVA allows the fabrication of circuits using conventional lithography under ambient conditions. It is expected that this reversible stability will prove in many aspects of device fabrication in the future. The PVA-10W coated graphene FETs results in n-type characteristics that is stable under ambient air conditions for one month, as shown in inset of Figure 2.19(a). The lightly- and heavily-doped devices were left under ambient condition for up to 3 months. A lightly-doped device goes back to p-type characteristics similar to as-grown graphene device, as shown in Figure 2.19(d). However, after heat treatment of the sample at 150 ^{o}C for 30 min, the device fully recovered the n-type behavior. This remarkable reversibility can be attributed to the charge transfer as well as the passivation layer by the bulky PVA film, which prevents ambient gases from being adsorbed to the graphene surface. Although water molecules are adsorbed on the PVA films as time increases, these molecules can be removed by heat treatment.

2.5 Conclusion and originality of this chapter

In summary, we demonstrated a method of implementing n-type doping to as-grown graphene in ambient condition using solution-based PVA coating. The n-type doping level can be achieved by varying temperature and hardening time of PVA coated on graphene films. Moreover, the graphene transistors can be converted from p-type transport behavior to ambipolar and n-type transport behavior by PVA doping with different solution concentrations. Long term stability of the n-doped graphene transistors up to three months has also been achieved. The highly stable n-doped originated from molecular charge transfer doing and PVA films played as passivation layer against p-doping from ambient condition. This long term stability can further enable us to fabricate basic logic circuits under ambient conditions. We believe that our approach will improve the fabrication of

complicated graphene-based logic circuits and numerous device fabrications in air.

Chapter 3

Transport characteristics of nitrogen-doped horizontally aligned SWNTs

This chapter continues discussing the doping of nanocarbon material, for instance, single-walled carbon nanotubes using as-grown chemical vapor deposition method. Horizontally aligned carbon nanotubes-based field-effect transistors are expected to enable the fabrication of high performance device using relatively simple techniques. However, as-grown nanotubes usually contain both metallic and semiconducting nanotubes, which lead to a trade-off between charge carrier mobility and on/off ratio. This part represents the synthesis and fabrication of nitrogen-doped horizontally aligned single-walled carbon nanotubes (N-HASWNTs) FETs. The growth of N-HASWNTs using chemical vapor deposition on an r-cut crystal quartz substrate, followed by peel off and transfer to a target substrate. Nitrogen dopant, either in the form of a chemical adatom or the pyridinelike configuration, would lead to p-type, whereas the substitutional nitrogen dopant induces the n-type doping. Although our N-HASWNT FETs show p-type behaviors, the resulting N-HASWNTs have will-controlled density and a unique morphology, consisting of small diameter nanotubes with large bandgap (~ 1 eV). N-HASWNTs device can simultaneously

demonstrate a mobility of 1,284 $cm^2V^{-1}s^{-1}$ and an on/off ratio ~ 10^6. We also demonstrate flexible FETs using N-HASWNT with high performance.

3.1 Background and Motivation

Carbon nanotubes (CNTs) is one of the leading materials for next electronics and optoelectronics due to its extraordinary properties, such as electrical, mechanical, and optical properties.[6] CNT field-effect transistors using horizontally aligned single-walled carbon nanotubes (HASWNTs) is relatively easy with high performance to fabricate devices on desired location and substrate compared with other method.[106] CNTFETs are also expected to enable fabrication complementary circuits with high performance by control of carrier type or density using several techniques. Compared to complementary metal-oxide-semiconductor (CMOS) FETs, CNTFETs have several advantages. First, near ballistic transport of carriers can be achieved which makes possible ultra-fast and high efficient devices due to its one dimensional structure. Second, high-k dielectric materials can be used as gate dielectric without degrading carrier transport in the active channel because of the absence of dangling bonds in carbon nanotubes. This leads to efficient gate field coupling that results in low subthreshold swing.

CNTFETs have been previously reported and have achieved high performance.[107-109] Simple logic gates, such as, inverter, NOR, SRAM and ring oscillator, and analog circuit using CNTFETs have been demonstrated.[110-112] Although these circuits show potential and a lot of challenges exist for nanotubes to fully replace CMOS technology. As different techniques point of view, individual nanotube mobility (~ in 10,000 cm^2/Vs range) is higher than as-deposited random network one (~ in 100 cm^2/Vs range). For CNT devices to be practically implemented in electronics, a full control of carrier type (hole or electron) and carrier concentration is fundamentally required. In this regard, the charge transfer from/to

physically or chemically adsorbed species has been widely studied. Amine-containing molecules,[39] potassium,[113,114] or Benzyl viologen[115] have been shown to n-type characteristics of CNTFETs. Some of non-chemical doping methods have also investigated, for instance, metal work function,[43] electrostatic,[44] and ion implementation.[45] However, adsorption of water or oxygen have been believed to be the origin of p-type behaviors of nanotube FETs.[116] Water or oxygen molecules induce a hole doping in the CNTs channel as well as reduce the Schottky barrier between the metal and nanotubes contact. Due to this reason, carbon nanotube FETs need to a more stabilized control carrier density of SWNTs.

Nitrogen atom has naturally been considered a good electron donor.[117,118] Previous simulation results suggest the substitutional atom has been shown different phenomena compared to chemically adsorbed adatom or pyridinelike configurations. [117,118] The former would lead to n-type nanotubes, whereas the later induces the p-type doped nanotubes. Recently we reported that heterostructure SWNTs were directly grown on the silicon substrate at 800 ^{o}C using ethanol and/or acetonitrile by chemical vapor deposition system.[119] It was characterized by x-ray photoelectron spectroscopy that nitrogen atoms are doped in our SWNTs. In this work, we report the synthesis and fabrication of nitrogen-doped horizontally aligned single-walled carbon nanotubes FETs. The growth of N-HASWNTs using CVD on an r-cut crystal quartz substrate, followed by peel off and transfer to a target substrate. Nitrogen dopant, either in the form of a chemical adatom or the pyridinelike configuration, would lead to p-type, whereas the substitutional nitrogen dopant induces the n-type doping. Although our N-HASWNT FETs show p-type behaviors, the resulting N-HASWNTs have will-controlled density and a unique morphology, consisting of small diameter nanotubes with large bandgap (~1 eV). N-HASWNTs can simultaneously demonstrate a mobility of 1,284 $cm^2V^{-1}s^{-1}$ and an on/off ratio ~ 10^6. We also demonstrate

flexible FETs using N-HASWNT with high performance.

3.2 Experiments

3.2.1 Growth of nitrogen-doped HASWNTs

Nitrogen-doped horizontally aligned single-walled carbon nanotubes were synthesized by CVD using an r-cut crystal quartz substrate (Hoffman Materials or Kyocera) as shown in Figure 3.1. Growth conditions of N-HASWNTs are different with that of conventional ACCVD HASWNTs in Table 3.1. Before N-HASWNT growth, the quartz substrates are annealed at 900 °C for 12 hrs in air. Catalyst lines were patterned using standard photolithography techniques in Figure 3.2, and then Fe (2 Å) were deposited in high vacuum condition using a thermal evaporator (ULVAC VPC-260F) with a quartz crystal thickness meter (CRTM-6000), and lift-off process. The patterned quartz substrate was annealed at 550 °C for 10 min in atmosphere to remove residual. The growth of

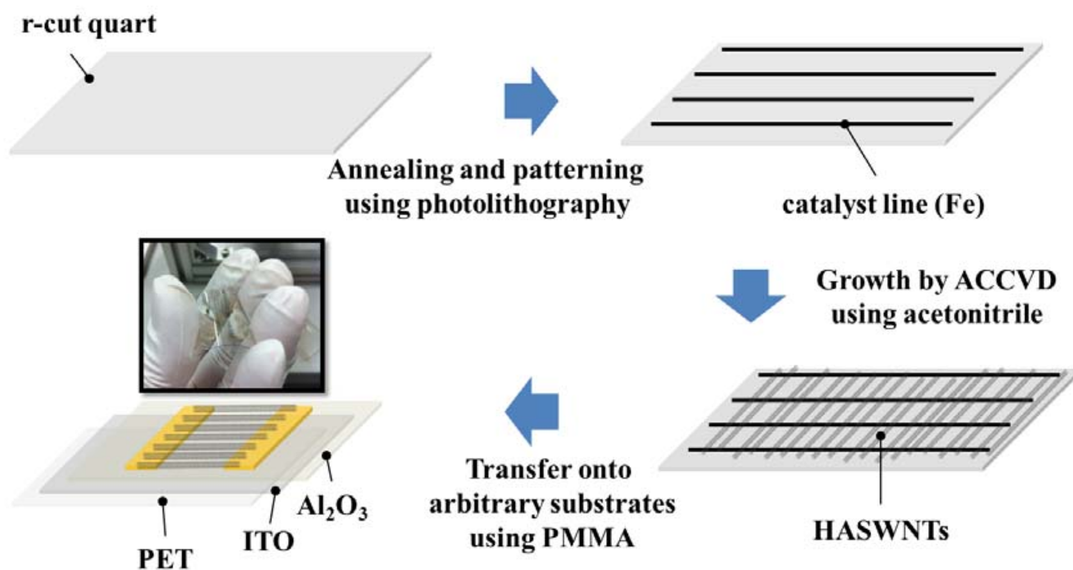

Figure 3.1. Growth procedures of horizontally aligned carbon nanotubes on a quartz substrate.

	Ethanol-based	Nitrogen-doped
Temperature	800 °C	800 °C
Catalyst	Fe or Co	Fe
Source gas	EtOH	EtOH or/and CH_3CN
	10 sccm & Ar/H2 440 sccm	50 sccm & Ar 500 sccm
Growth time	15 min	15 min

Table 3.1. Comparison of growth conditions between ethanol based HASWNTs and nitrogen-doped HASWNTs.

N-HASWNTs is carried out at 800 °C for typically 15 min under ethanol and/or acetonitrile (C_2H_3N). Prior to growth, iron oxide was reduced under Ar/ H_2 (3 %) until temperature reached at 800 °C. Following the reduction, 50 sccm and 500 sccm of ethanol or/and acetonitrile and argon atmospheres, respectively. To study the effect of the nitrogen source gas, the ratio of ethanol and acetonitrile is varied between 100:0 to 0:100. During the cooling step, 300 sccm of argon was flowed until room temperature was reached.

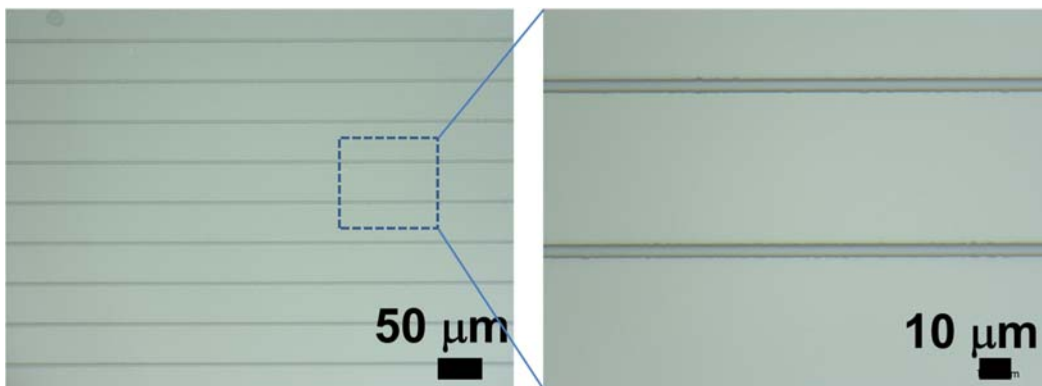

Figure 3.2. Optical image of the line pattern on an r-cut crystal quartz substrate by conventional photolithography process.

3.2.2 Transfer process

There are many kinds of transfer methods, such as wet-etching with $FeCl_3$ or HCl, roll-to-roll, dry transfer with thermal release tape, and membrane filter, to fabricate electronic device or transparent conducting film on a desired location and substrate using SWNTs and graphene.[120-124] The HASWNTs/quartz and transfer process used in this study to fabricate carbon nanotube can be applied to device fabrication on rigid or flexible substrates. Here, the transferring of the HASWNTs on a SiO_2/Si substrate was carried out similarly to a method previously reported on the transfer of carbon nanotubes.[125] Figure 3.3(a) summarizes the steps of the transfer process.

Poly(methyl methacrylate) (PMMA) (4 % in anisole) was spun on the as-grown N-HASWNT on quartz substrate in Figure 3.3(b) with 3,000 rpm for 1 min, followed by peeling off at 90 °C for 5 min with 1 M of sodium hydroxide (NaOH, Wako). The quartz

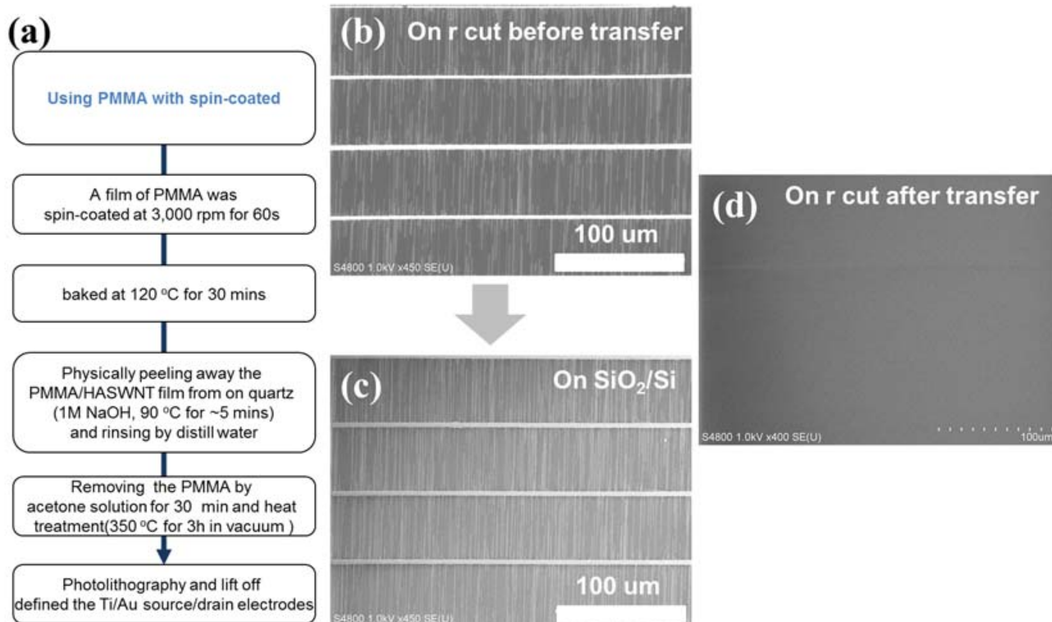

Figure 3.3. (a) Transfer process of HASWNTs on a quartz substrate. (b), (c), and (d) SEM images of HASWNTs on quartz and SiO_2/Si substrates before/after transfer carbon nanotube by PMMA, respectively.

substrate does not etch completely, and only a miner etching of the quartz surface is enough to release the PMMA/HASWNTs layer. The PMMA/N-HASWNTs film was rinsed and floated for 20 min by distilled water to remove the residual, followed by neutralizing with deionized water. After the PMMA/N-HASWNTs film was transferred onto either SiO_2/Si in Figure 3.3(c) or an indium tin oxide (ITO) -coated polyethylene terephthalate (PET) substrate (thickness ~ 190 μm), PMMA layer was removed by acetone vapor and thermal annealing at 350 ^oC for 3 hrs under an vacuum atmosphere. A transferred quartz substrate was clean by SEM as shown in Figure 3.3(d).

3.2.3 Fabrication of N-HASWNT field-effect transistors

The N-HASWNT FETs were fabricated using standard photolithography techniques. An

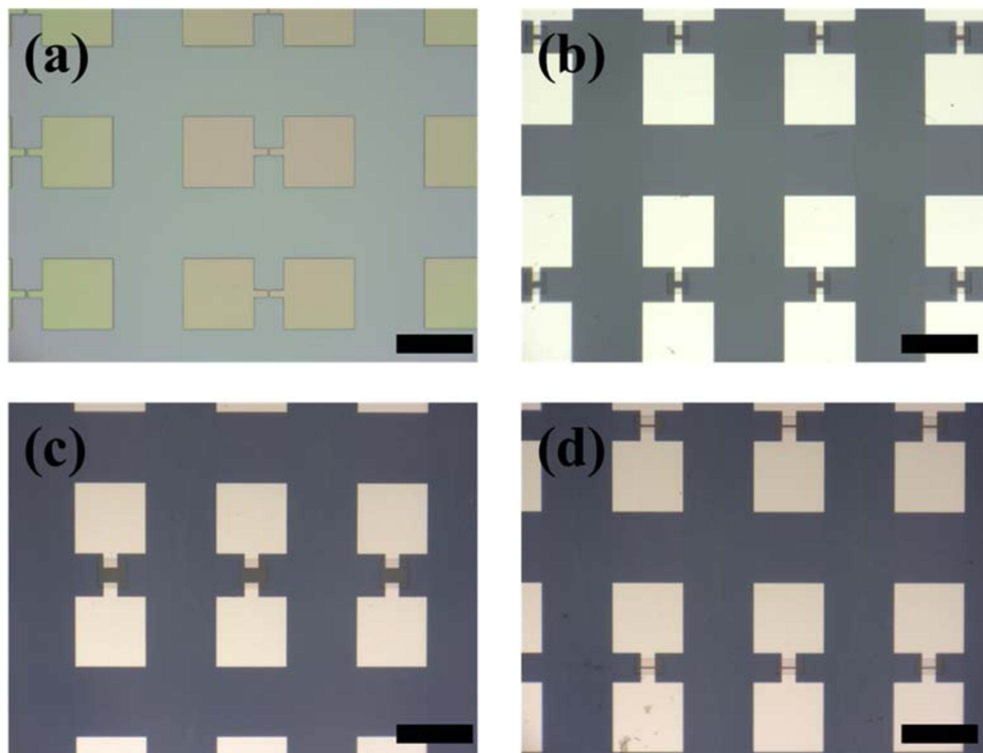

Figure 3.4. Optical images of patterning HASWNTs on SiO_2/Si and PET substrates after 1st and 2nd photolithography procedures, respectively. (a) and (b) are on a silicon substrates. (c) and (d) is optical images in PET substrates. (Scale bars are 100 μm)

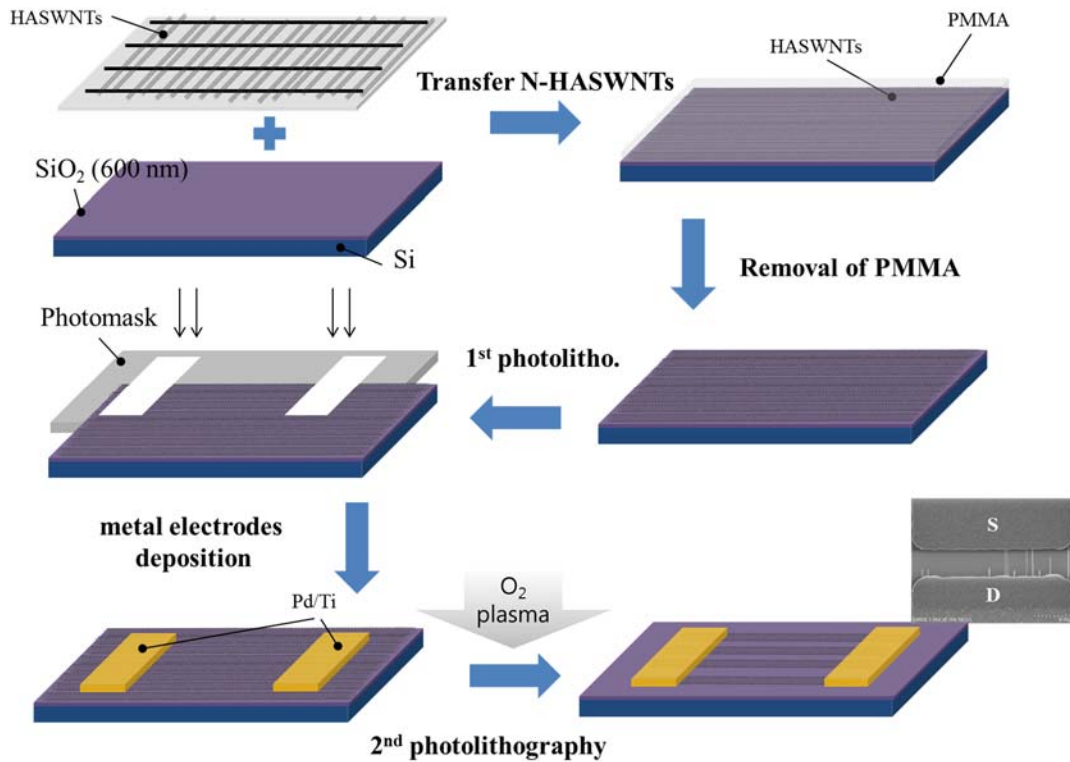

Figure 3.5. Process for HASWNT-FET fabrication and schematic diagram of a back-gated HASWNT-FET measurement.

N-HASWNTs grown from an r-cut crystal quartz substrate was transferred onto thermally grown silicon dioxide (600 nm) on doped silicon or flexible substrate, for instance, ITO-coated PET. Ti/Pd (2/40 nm) ohmic metal contacts were patterned using a lift-off process as shown in Figure 3.4(a) and (c), respectively. Subsequently, the patterned substrate was carried out 2nd photolithography in Figure 3.4(b) and (d). N-HASWNTs outside the active channel area were removed by oxygen plasma etching system (100 W, 100 Pa) for 60 s. The entire fabrication step of HASWNT FETs is shown in Figure 3.5.

3.2.4 Characterization of N-HASWNT FETs

An Agilent Semiconductor Parameter Analyzer 4156C was used to characterize the

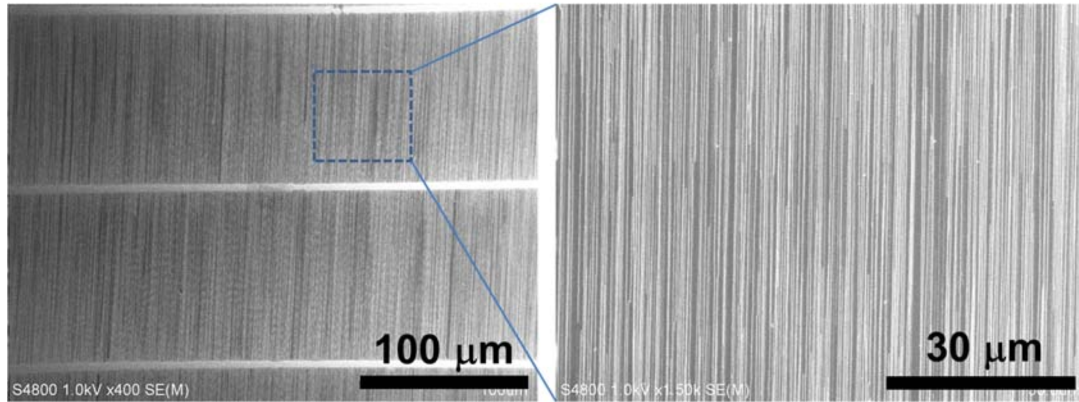

Figure 3.6. SEM images of a pattern of perfectly aligned, perfectly linear SWNTs on a quartz substrate by ACCVD growth. The bright horizontal stripes correspond to the regions of iron catalyst. The right SEM image provides a magnified view. Theses arrays contain ~ 4 SWNTs μm^{-1}.

electrical properties of N-HASWNTs devices. The surface morphology of N-HASWNT was examined by atomic force microscopy (SPI3800N, Seiko Instrument) and scanning electron microscopy (S-4800, Hitachi). Micro Raman spectroscopy (inVia Renishaw) was used to characterize N-HASWNTs. To identify configuration of a nitrogen atom in carbon nanotube, we used Electron Energy Loss Spectroscopy (EELS) and high resolution transmittance electron microscopy (TEM, JEM-ARM200F) because the combination of TEM imaging, core-loss EELS, and low-loss EELS provides detailed information about physical structure, chemical bonding, density, and electronic behavior on a nanometer scale.

3.3 Results and discussion

3.3.1 HASWNTs and N-HASWNTs growth on quartz substrates

Figure 3.6 shows SEM images of representative array ethanol-based HASWNTs on a quartz substrate by ACCVD growth. ACCVD on quartz wafers using patterned stripes of iron

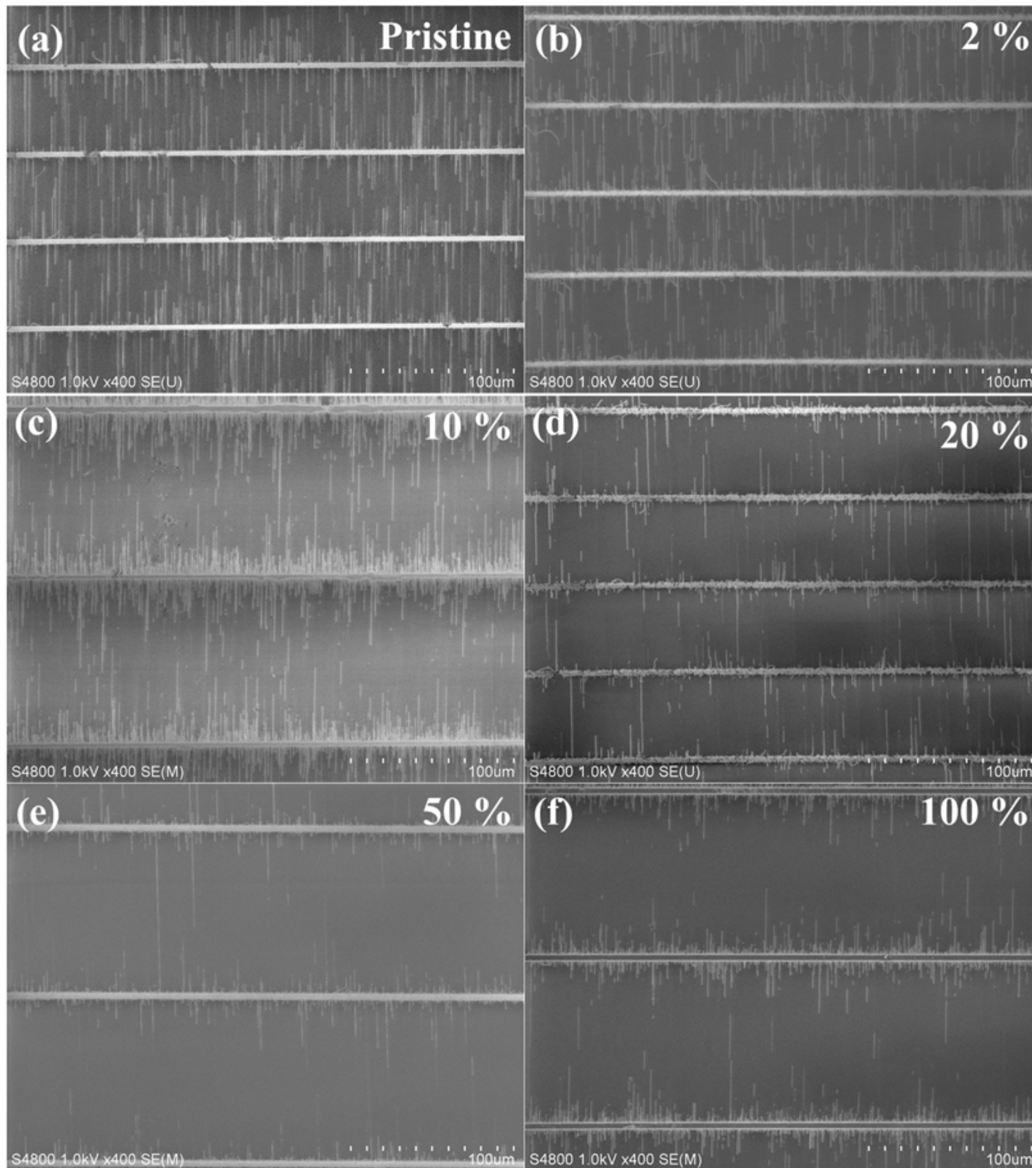

Figure 3.7. SEM images of nitrogen-induced HASWNTs and ethanol-based HASWNTs on a quartz substrate by CVD growth as a function of acetonitrile concentration , for instance, (a) low density pristine, (b) 2 %, (c) 10 %, (d) 20 %, (e) 50 %, and (f) 100 %, respectively. (Scale bars are 100 μm)

catalyst and EtOH feed gas forms arrays of individual SWNTs with average diameters of ~

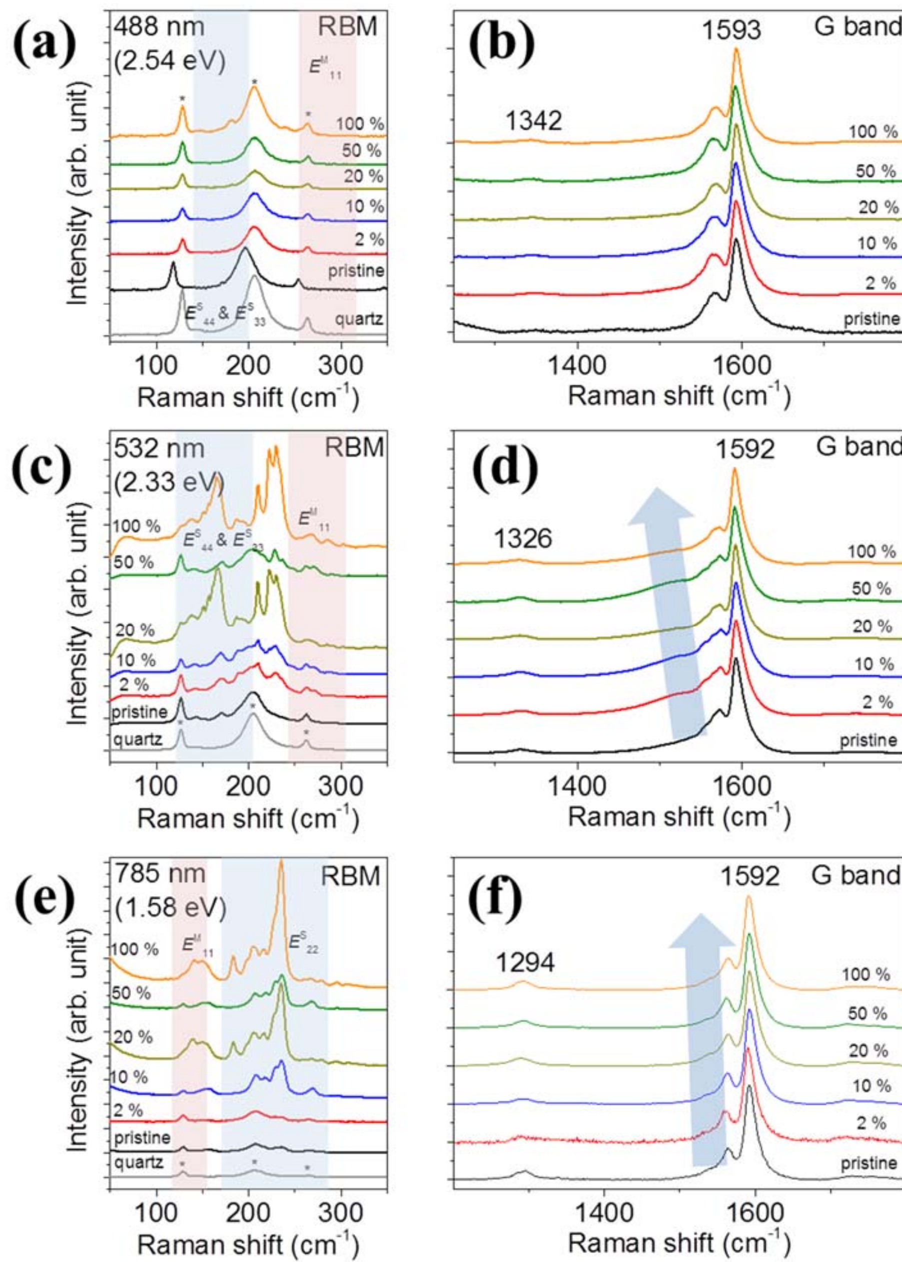

Figure 3.8. Raman spectra of the pristine HASWNT sample and nitrogen-induced HASWNT on an r-cut crystal quartz substrate at excitation energies of (a)-(b) 2.54 eV, (c)-(d) 2.33 eV, and (e)-(f) 1.58 eV. All Raman spectra were normalized to the G band intensity. The peaks marked by asterisks originated from the quartz substrates in RBM modes. The arrow shows the G band peak position shift in G band modes.

1 nm, lengths of up to a few hundred μm, and densities approaching ~ 4 SWNTs μm-1. The

synthesis of nitrogen-doped HASWNTs was carried out at same temperature under EtOH and C_2H_3N source with low pressure CVD. Figure 3.7 shows SEM images of N-HASWNTs and ethanol-based HASWNTs on an r-cut crystal quartz substrate as a function of nitrogen consistency, for instance, (a) low density EtOH-based HASWNTs, (b) 2 %, (c) 10 %, (d) 20 %, (e) 50 %, and (f) 100 % acetonitrile-based sample, respectively. The density of horizontally aligned SWNTs was reduced as nitrogen concentration increases. We also synthesized a low density of ethanol-based HASWNTs on purpose to make a comparison between N-HASWNTs and pristine without considering density of nanotubes.

Figure 3.8 shows the Raman spectra of the pristine HASWNTs and nitrogen-treated samples on an r-cut crystal quartz substrate with laser excitation energies at (a)-(b) 2.54 eV, (c)-(d) 2.33 eV, and (e)-(f) 1.58 eV. The corresponding RBM spectra and the number of G band show the phonon frequencies. All peak intensities were normalized to the G band intensity at 1590-1593 cm^{-1}. For the 2.54 eV E_{laser}, the RBM spectra correspond to the $E^{S}_{33}$and and E^{S}_{44} semiconductor and E^{M}_{11} metallic resonance conditions that were assigned by the calculated Kataura plot by extended tight-binding method.[126] RBM peaks shift as a function of nitrogen content is not clearly shown due to some peaks from the quartz substrates. Similarly, for the 2.33 eV and 1.58 eV E_{laser}, the RBM spectra could not be assigned specifically as being metallic and semiconducting HASWNTs, as shown in Figure 3.8(c) and 3.8(e). The G+ band peak shift has been observed as acetonitrile increase. The downshift by 1 ~ 2 cm^{-1} in N-HASWNTs with reference (ethanol-based HASWNT) at 2.33 eV and 1.58 eV is evidence of charge transfer from electron-donating nitrogen to carbon nanotubes in Figure 3.8(d), and 3.8(f). However, the G band peak shift from n-doping could not confirm because of substrates effect.

To reduce the substrate effect, evaluation from resonance Raman spectra on each sample

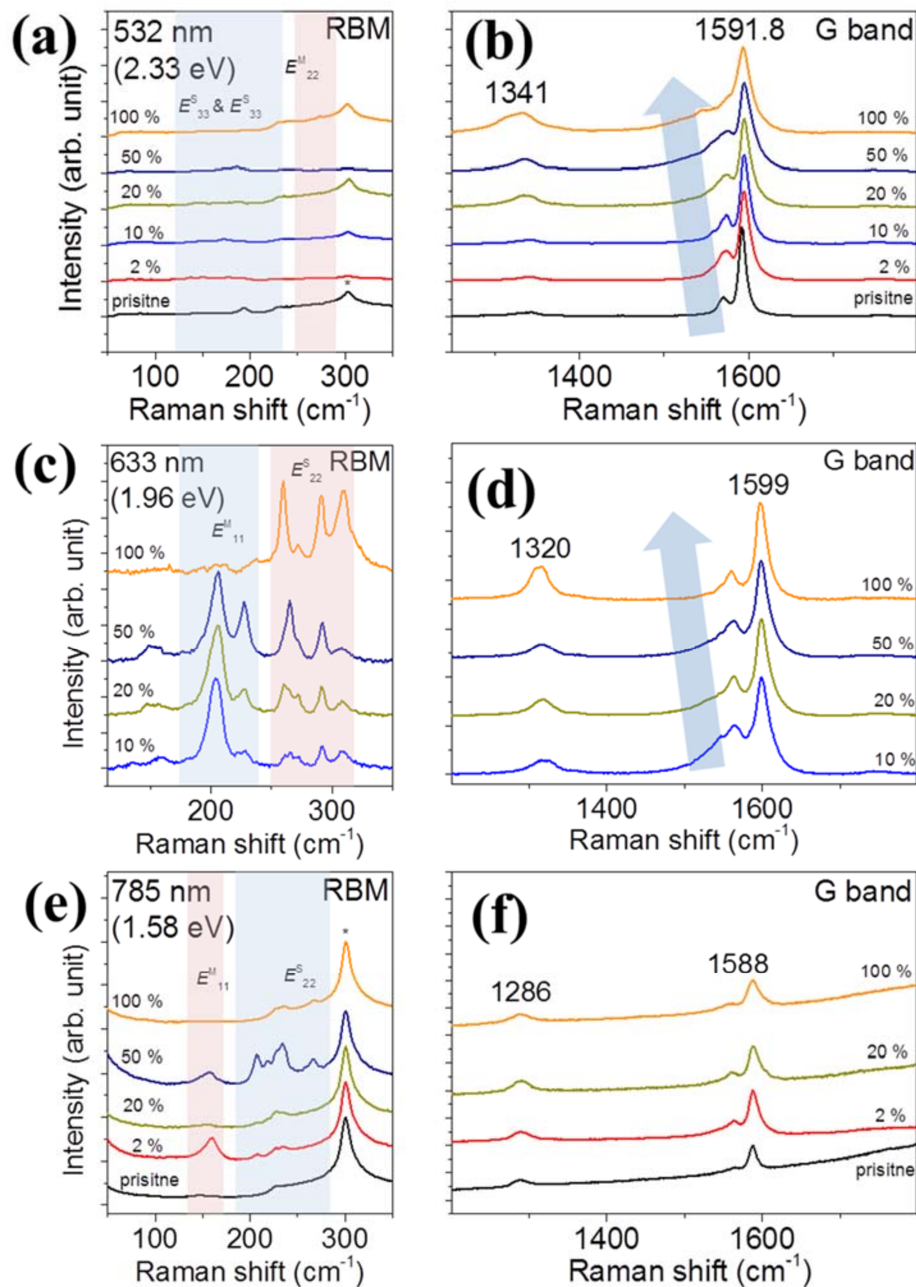

Figure 3.9. Raman spectra at various excitation energies of the HASWNT and N-HASWNT samples on SiO_2/Si: (a) and (b) 2.33 eV, (c) and (d) 1.96 eV, and (e) and (f) 1.58 eV. All Raman spectra were normalized to the G-band intensity. The numbers in each figure are the diameters of the corresponding peaks in nm and phonon frequencies. $E^{S(M)}_{ii}$ indicate the van Hove singularity transition energy between the *i*th levels of the semiconducting (metallic) nanotube.

on a silicon substrate using 532 nm (2.33 eV), 633 nm (1.96 eV), and 785 nm (1.58 eV)

laser excitation wavelengths reveals that the resulting sample contains several other chiralities with low density, such as diameter reduction, as shown in Figure 3.9. The chirality of carbon nanotubes can be identified using the RBM in Raman spectroscopy.[127] The RBMs are inversely proportional to the diameter of the nanotubes, $\omega\,(\mathrm{cm^{-1}}) = a/d_t\,(\mathrm{nm}) + b$, where d_t is the diameter of the nanotube, and a and b are constants that vary according to the environment such as the bundle or substrate. For example, a=248 and b=0 for isolated nanotubes on a SiO_2 substrate, and a=234 and b=10 for bundles. However, the assignment becomes difficult for a relatively higher E_{ii} and a larger d_t because there are many overlaps of (n,m) in the Kataura plat between semiconducting and metallic nanotubes. G band spectra might be able to distinguish between metallic and semiconducting nanotubes in the Raman spectra, where the separation of frequencies for the split G band (G+ and G-) has a different diameter dependence and a different spectral shape.[128] This discussion is difficult because the G band Raman intensity strongly depends on the chiral angle,[128] particularly for

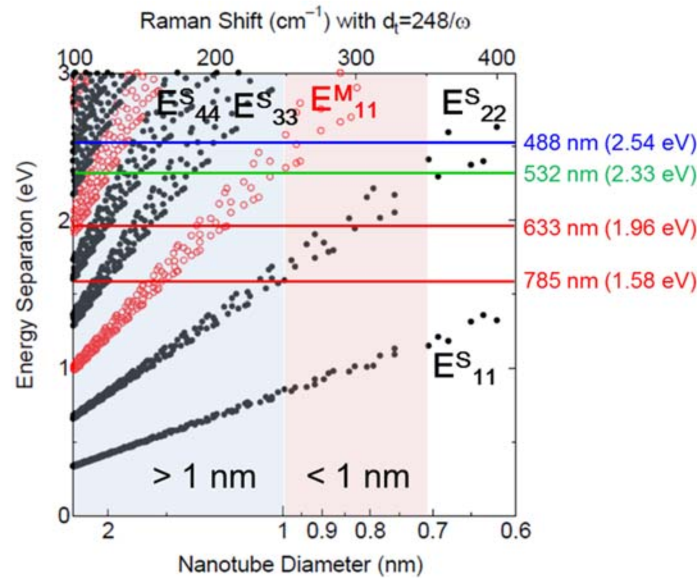

Figure 3.10. Kataura plot obtained from extended tight-binding model. The solid line is incident laser energies used in experiment.

a nanotube with a chiral angle near a zigzag nanotube.[129]

Figure 3.9(c) shows the RBM using 1.96 eV laser excitations for different nitrogen concentration, and Figure 3.9(d) shows also G band. From these spectra, the RBM frequency at ~ 203 cm^{-1} was predominant for 10 % amounts of acetonitrile and 90 % EtOH, however this peak was weakened and other peaks at 260, 291, and 309 cm^{-1} were strengthened when the concentration of acetonitrile is 100 %. The strongest RBM peak in Figure 3.8(c) at 203 cm^{-1} is assigned to (15,0) metallic nanotubes with a diameter of ~1.2 nm, due to metallic (E^{M}_{11}) nanotube by 633nm laser, according to the Kataura plot (transition energies as a function of nanotube diameter),[22,130] as shown in Figure 3.10. This assignment is consistent with the fact that the G band spectra show a metallic Breit-Wigner-Fano (BWF) line but a Lorentzian G band at the lower energy side as shown in Figure 3.9(c) and (d). However, with high acetonitrile concentration over 50 %, the RBM peaks were observed relatively strong at 260, 291, and 309 cm^{-1}. These RBM peaks are assigned to semiconducting nanotubes with a diameter of 1, 0.9, and 0.8 nm, due to the second van Hove transition (E^{M}_{22}) by 633 nm laser by the calculated Kataura plot. This

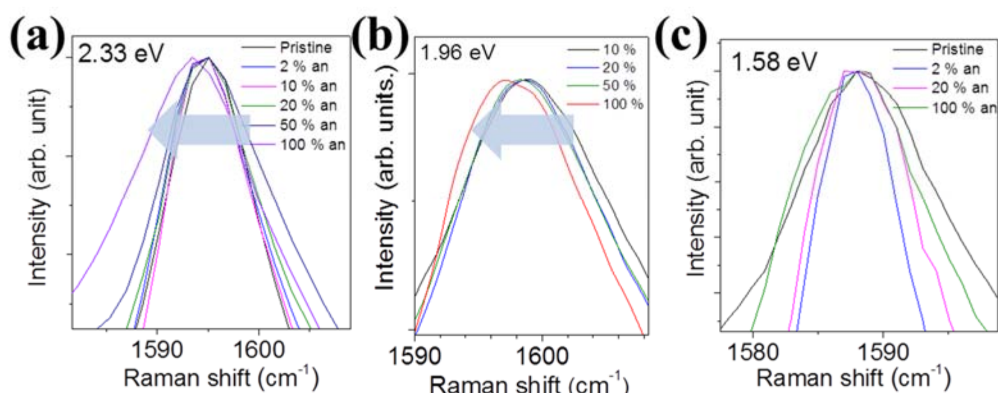

Figure 3.11. G band peak shift as a function of various acetonitrile concentrations by different laser. (a) 2.33 eV, (b) 1.96 eV, and (c) 1.58 eV.

assignment is in proportion to the fact that the G band spectra do not show a metallic BWF line but a Lorentzian G band as shown in Figure 3.9(d). Therefore, it is believed that the change of RBM peaks from the specimen grown under the high acetonitrile concentration is possibly due to deformation or etching of nanotubes by acetonitrile. Similar trends were shown using 2.33 eV and 1.58 eV laser excitation wavelengths as shown in Figure 3.9(a)-(b) and 3.9(e)-(f).

The G+ band peak shift has been observed in acetonitrile with nitrogen. The downshift by ~ 3 cm^{-1} in N-HASWNTs with reference (ethanol-based HASWNT) at 2.33 eV and 1.96 eV is evidence of charge transfer from electron-donating nitrogen to carbon nanotubes in Figure 3.11(a), and 3.11(b). Nevertheless, this trend becomes ambiguous in some cases, particularly in SWNTs at 1.58 eV is unclear as shown in Figure 3.11(c). The change in charge transfer was negligible. This concurs with the previous report that intentional doping

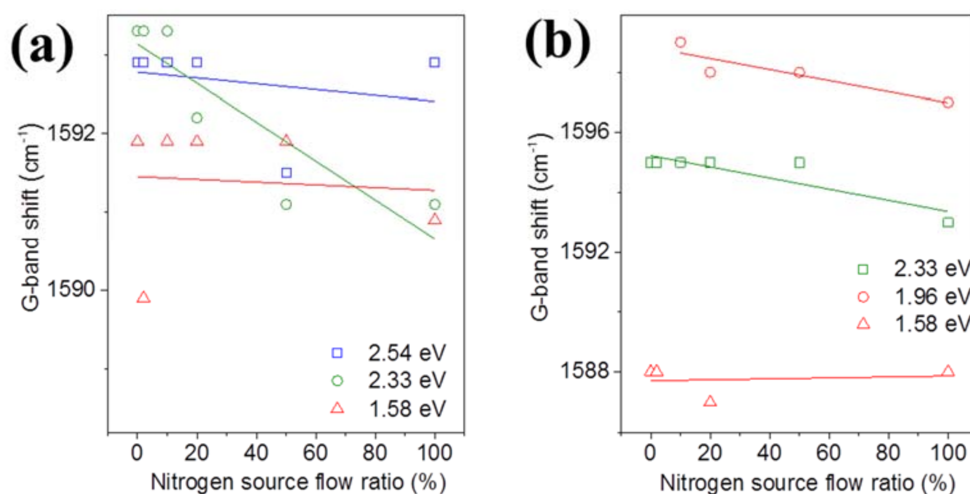

Figure 3.12. (a) G band peak shift of HASWNT on quartz substrates with an acetonitrile concentration increases. (b) G band peak shift of HASWNT on silicon substrates with an acetonitrile concentration increases.

invoked by charge transfer resulted in a downshift (donor) and upshift (acceptor) of the G band.[131] This suggests that the electron-donating/withdrawing ability determines the amount of charge transfer to carbon nanotube depend on dopants. From this point of view, the peak shift in the G+ band effect of charge transfer is effective, therefore it may be a good measurement of the changes induced by the acetonitrile consistency. The G peak shift of samples on quartz and silicon substrate with various lasers is respectively summarized, as shown in Figure 3.12(a) and 3.12(b).

The weak peak (D band) near 1317 cm^{-1} in Figure 3.9(b), 3.9(d), and 3.9(f) is attributed to disordered graphite and amorphous carbon. The generation of D band strongly suggests that the nitrogen atom interacts with the carbon nanotube during the growth. With HASWNTs synthesis by acetonitrile and/or EtOH, nitrogen dopant can be in the form of a chemical adatom, the pyridinelike, or the substutional configuration in nanotubes. The intensity ratio

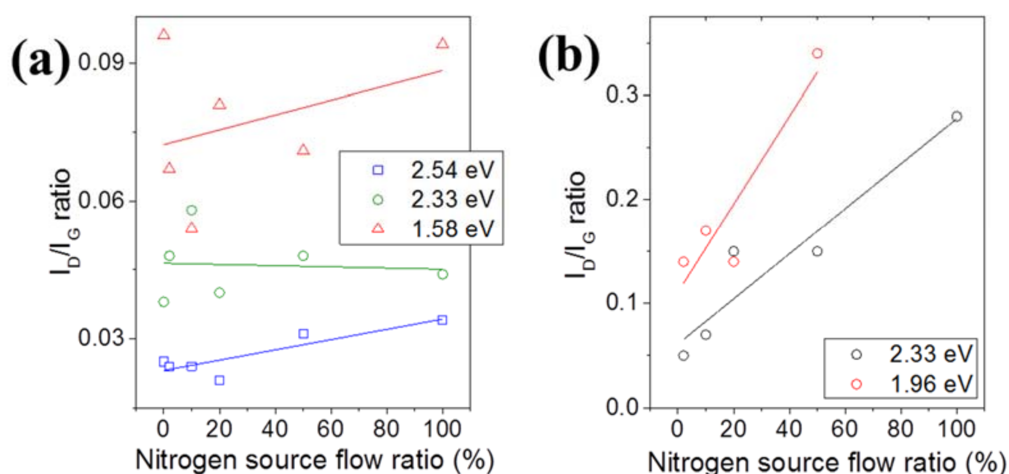

Figure 3.13. (a) Intensity ratio of D band to G band of HASWNT on quartz substrates with an acetonitrile concentration increases. (b) Intensity ratio of D band to G band of HASWNT on silicon substrates with an acetonitrile concentration increases.

of D band to G band (I_D/I_G) can be used as a measure of nanotube imperfection. Figure 3.13(a) and (b) show that I_D/I_G increases of the pristine and nitrogen-doped HASWNT on a quartz and silicon substrate as increase of the nitrogen consistency. It is thought that the N-SWNTs are not stably formed under a high dose of acetonitrile.

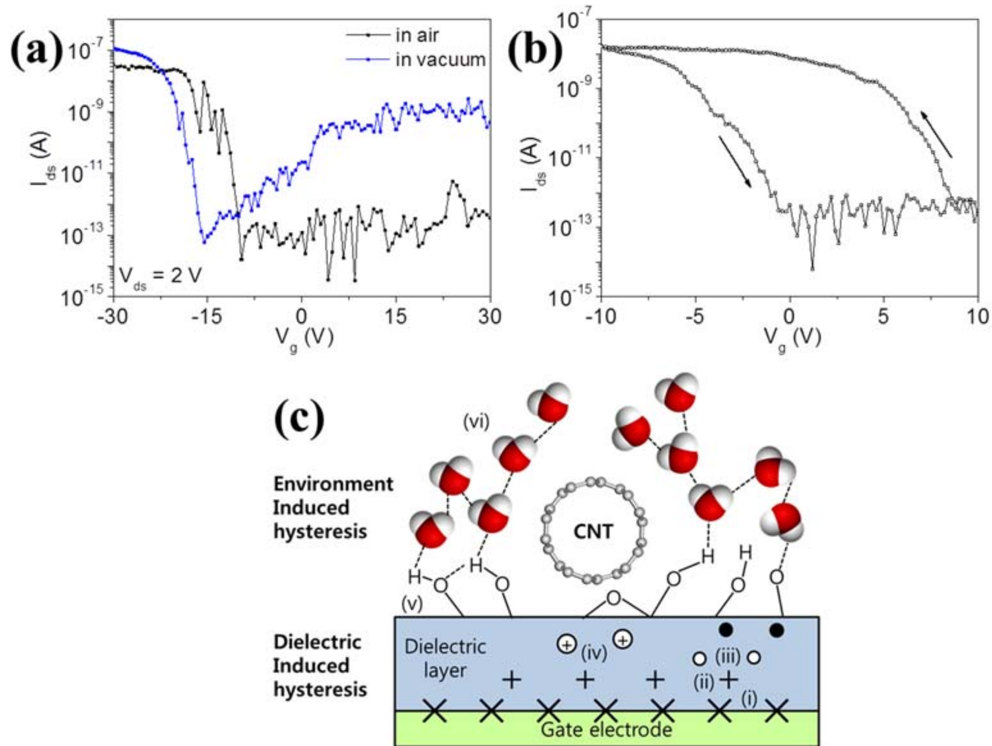

Figure 3.14. Typically electrical properties of back-gated (t_{ox} ~ 600 nm) HASWNT FETs. (a) Transfer characteristics at V_{ds} = 2 V was applied from -30 to +30 V in air (black) and vacuum (blue) condition, respectively. (b) Sweeping characteristics of HASWNT device. (c) The possible origin of hysteresis of (i) interface trapped charge, (ii) fixed oxide charge, (iii) oxide trapped charge, (iv) mobile oxide charge, (v) oxide-CNT interface charge, (vi) water molecule-induced charge.

3.3.2 I-V characteristics (I_{ds}- V_{gs}) of HASWNT devices

Figure 3.14 shows typical transfer characteristics of the HASWNT FETs measured from a

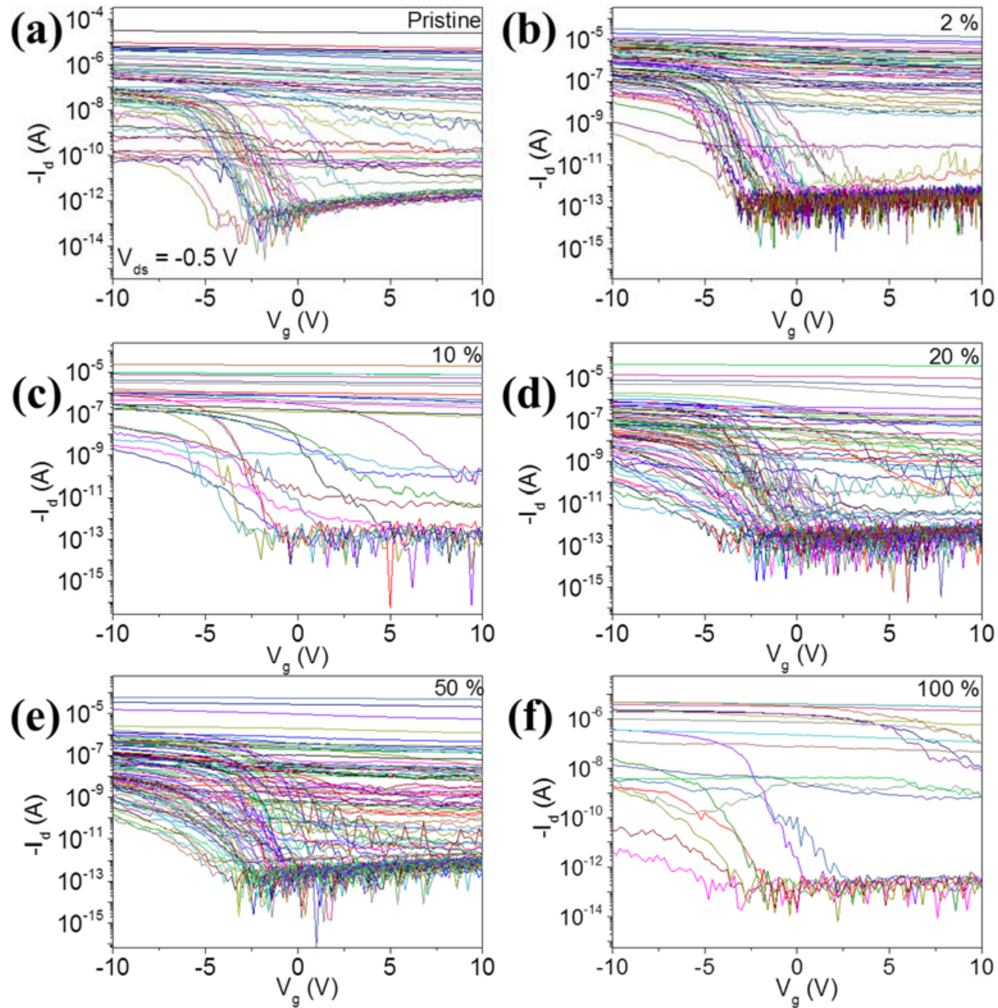

Figure 3.15. Corresponding transfer characteristics in terms of each device in ambient air condition (V_{ds} = -0.5 V), respectively. (a) pristine, (b) 2 % acetonitrile concentration, (c) 10 %, (d) 20 %, (e) 50 %, and (f) 100 % HASWNT FETs.

set of devices in ambient air and vacuum condition, respectively. The responses indicate p-type behavior, consistent with observations in single nanotube devices that use similar materials and designs in air. A common feature of the back-gated, un-passivated nanotube FETs is the large hysteresis in the I_{ds}-V_{gs} characteristics that are often observed when the

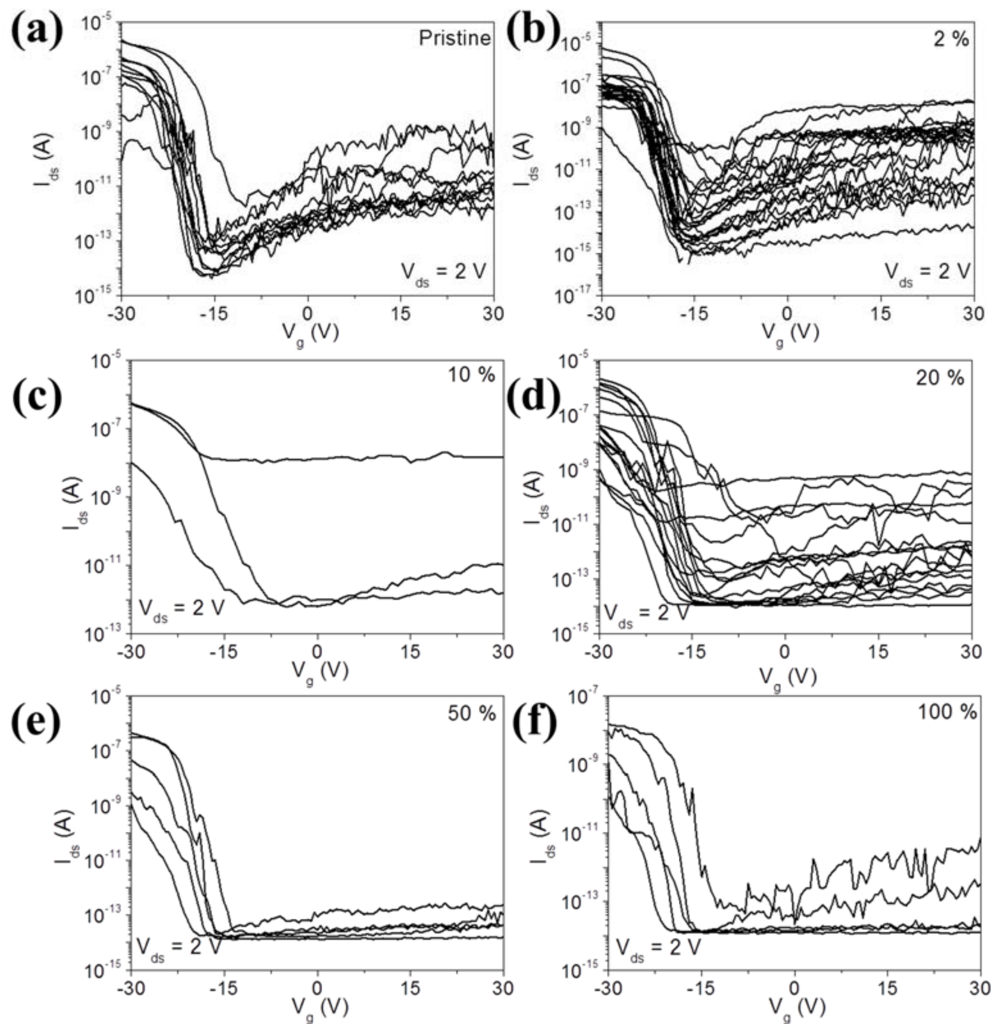

Figure 3.16. Corresponding transfer characteristics in terms of each device under vacuum condition (~10^{-3}-10^{-4} Pa), respectively (V_{ds} = 2 V). (a) pristine, (b) 2 % acetonitrile concentration, (c) 10 %, (d) 20 %, (e) 50 %, and (f) 100 % HASWNT FETs.

back gate voltage is swept in different directions in Figure 3.14(b).[116] This hysteresis which depends on the sweeping speed is highly undesirable for transistor applications as it induces instability in the threshold voltage and the current of the device. In general, several source of hysteresis exits, as shown in Figure 3.14(c): (i) interface trapped charges due to structural

defects or impurities, (ii) fixed oxide charges near the electrode and oxide interface, (iii) oxide trapped charges due to holes or electrons trapped in the oxide, (iv) mobile oxide charges caused by ionic impurities, (v) surface dipoles formed between nanotube channel and gate oxide surface, and (vi) environmental adsorbates.[116,132] The hysteresis can be reduced by gentle annealing of the nanotube devices in a vacuum condition, first. Upon exposure to air, the devices once again showed large hysteresis as the water molecules reabsorbed on the device surfaces. The large sensitivity to the environment is expected for carbon nanotubes due to their large surface area to volume ratio, with all atoms exposed to the surface. Second method, a simple approach for passivating nanotube FETs is to spin-coat a thin film of PMMA (~ 100 nm), followed by baking at 180 ^{o}C for 12 hrs during which water molecules are desorbed from the nanotube surface. PMMA is a highly hydrophobic polymer that results in effective passivation of the nanotube devices with low permeability to water molecules. However, we need to other annealing method to see the intrinsic nitrogen-doped nanotubes, and will discuss later.

3.3.3 I-V characteristics (I_{ds}-V_{gs}) of N-HASWNT devices

In Figure 3.15(a)-(f), the transport characteristics of pristine and N-HASWNT transistors show p-type transport behavior in air, as characterized by on- and off-states in negative and positive biases, respectively, with the I_{on}/I_{off} ratio of 10^2-10^5 or without off-state due to metallic nanotubes. The p-type unipolar characteristics change to ambipolar transport only after evacuation for several hours, as shown in Figure 3.16(a) and (b). It should be noted that the large increases in I_{ds} at high V_{gs} are not due to the leakage current (I_{gs}) through the gate oxide. Such a conversion from p-type to ambipolar behavior is a typical behavior of the intrinsic SWNT transistors, being ascribed to the removal of environmental residues. However, transport behaviors of other N-HASWNT FETs, for instance, above 10 %

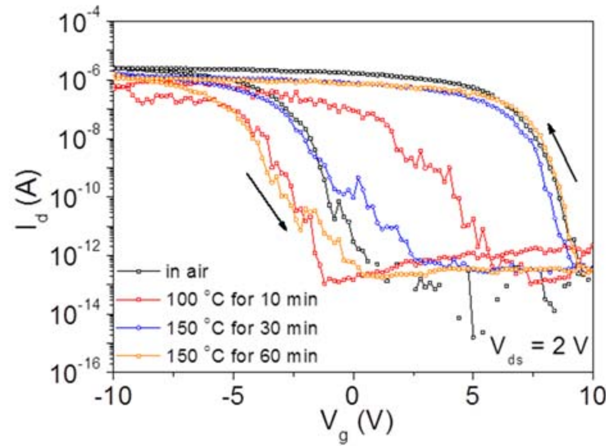

Figure 3.17. Corresponding I_d-V_g characteristics of the 10 % N-induced HASWNT FETs before/after thermal annealing in vacuum condition (10^{-3}-10^{-4} Pa).

nitrogen consistency, did not convert to ambipolar or n-type behavior in spite of in vacuum condition (~ 10^{-3}-10^{-4} Pa) as shown in Figure 3.16(c)-(f). We cannot identify the intrinsic electrical property of N-HASWNT without post treatment, for instance, heat annealing or electrical annealing due to environmental residues.

3.3.4 I_{ds}-V_{gs} curves of N-HASWNT devices after electrical annealing

After N-HASWNTs device fabrication, we first probed the devices in air and always observed p-doping as shown in Figure 3.17. Then we pumped the devices to ~ 10^{-3} to 10^{-4} Pa for several hours and recorded I_{ds}-V_{gs} curves in vacuum, followed by thermal annealing in vacuum. Figure 3.17 shows the thermal annealing condition in vacuum for a 10 % N-HASWNTs and the I_{ds}-V_{gs} curves after V_{ds} double sweep. The hysteresis of the device was not reduced up to the maximum temperature of the analyzer. In case of 10, 20, 50, 100 % N-HASWNT transistors, we probed the devices in vacuum and always observed p-type behaviors between V_{gs} = -10 to 10 V in I_{ds}-V_{gs} curves as shown in Figure 3.17, subsequently, by electrical annealing (e-anneal) in vacuum. In other words, the source/drain

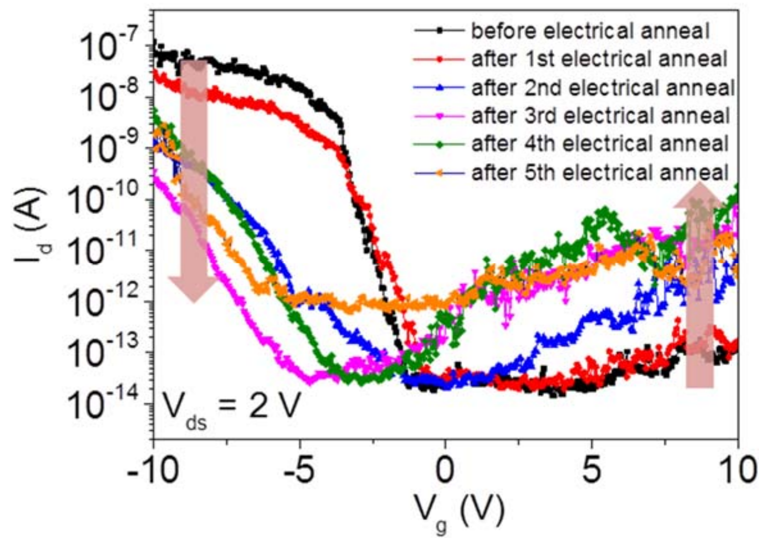

Figure 3.18. Corresponding I_d-V_g characteristics of the 20 % N-HASWNT FETs before/after annealing using electrical annealing in vacuum condition (~ 10^{-3}-10^{-4} Pa).

bias was swept from zero to a few volts, resulting in a temperature rise of the nanotubes due to Joule heating. With 20 % N-HASWNT FET, the p-type unipolar of I_{ds}-V_{gs} curves change to ambipolar transport after e-anneal for several repeated attempts with different condition, such as various drain voltages and with/without gate voltage as shown in Figure 3.18. We need to do experiments with much stronger e-anneal condition than previous to see the intrinsic N-HASWNTs transistors.

3.3.5 Threshold voltage (V_{th}) shift as a function of acetonitrile ratio

The annealing in vacuum removes the adsorbed oxygen and results in the direct modification of the Schottky barrier height at the contact. In contrast, doping changes the barrier thickness and introduces significant shifts of the threshold voltage of the device.[114] These results are consistent with a simple model in which the main role of oxygen is not to dope the nanotube but to modify directly the line-up of the nanotube bands at the

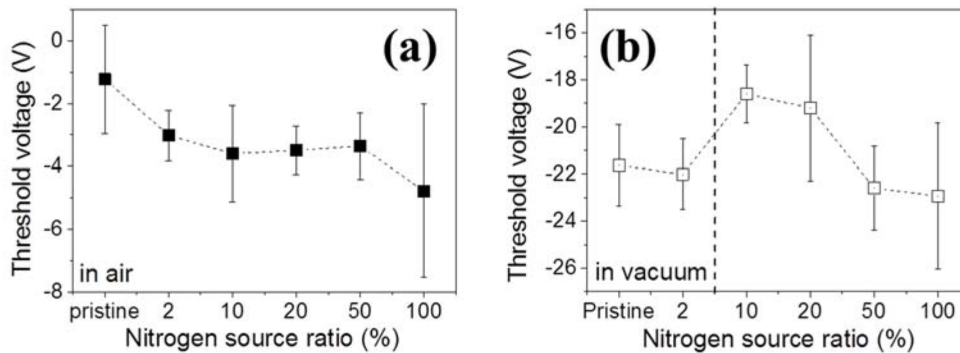

Figure 3.19. Threshold voltage shift as function of nitrogen-induced various acetonitrile concentrations ratio through transfer characteristics in the linear region. (a) In air. (b) In vacuum condition.

metal-nanotube junction. Figure 3.19(a) and (b) show shifts in the threshold voltage of N-HASWNTs transistors. Shifting its threshold voltage from -1 V to -5 in Figure 3.19(a) suggests an increase in electron concentration and corresponding electron (n-type) doping in carbon nanotubes. Nitrogen doping produces n-type carbon nanotubes by shifting the Fermi level to the conduction band, for instance, the electron concentration in the conduction band increases and the conductance of devices increases for a given positive gate voltage. The threshold voltage shift is similarly moved into negative gate voltage as shown in Figure 3.19(b).

Figure 3.20 shows the threshold voltage shift of 20 % N-HASWNT FET as the number of e-annealing increases under vacuum condition.

3.3.6 Nitrogen configuration of N-HASWNT by EELS

Electron energy loss spectroscopy (EELS) has been used for the identification of elements and the determination of their binding state to their environment. Even with pristine CNTs

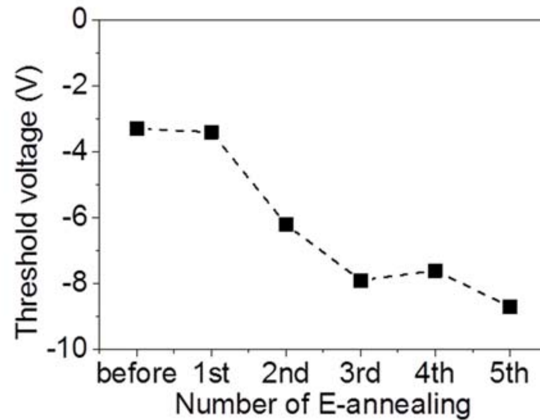

Figure 3.20. Threshold voltage shift as number of e-annealing increase with 20 % acetonitrile concentrations through I_d-V_g curves in the linear region in vacuum condition.

on which EELS has been used to detect the presence of amorphous carbon or impurities at the atomic scale.[133] The advantage of EELS over EDS is in its sensitivity to lighter elements such as boron and nitrogen. Spatially resolved EELS is an exceptionally sensitive technique for the study of decorated CNTs wherein a precise mapping of the various elements provides an atomic scale resolution of the coating and gives valuable information on the uniformity and crystal structure of the coating.

The HASWNTs samples were prepared for EELS and HRTEM analysis by transfer method by PMMA. First, 4 % PMMA solution was spin-cast on the HASWNT on quartz substrate with similar with ordinary condition. A thin film of the PMMA/HASWNT was then placed on a copper grid and the acetone allowed to remove PMMA. Subsequently, the grid was heat treatment at 350 ^{o}C for 3 hr under vacuum condition. We performed ~ 10 point EELS measurement with very short integration time due to beam damage and confirmed presence or absence of nitrogen peak (~401 eV) as shown in Figure 3.21. Decision of operating parameters involves a trade-off among signal levels, energy

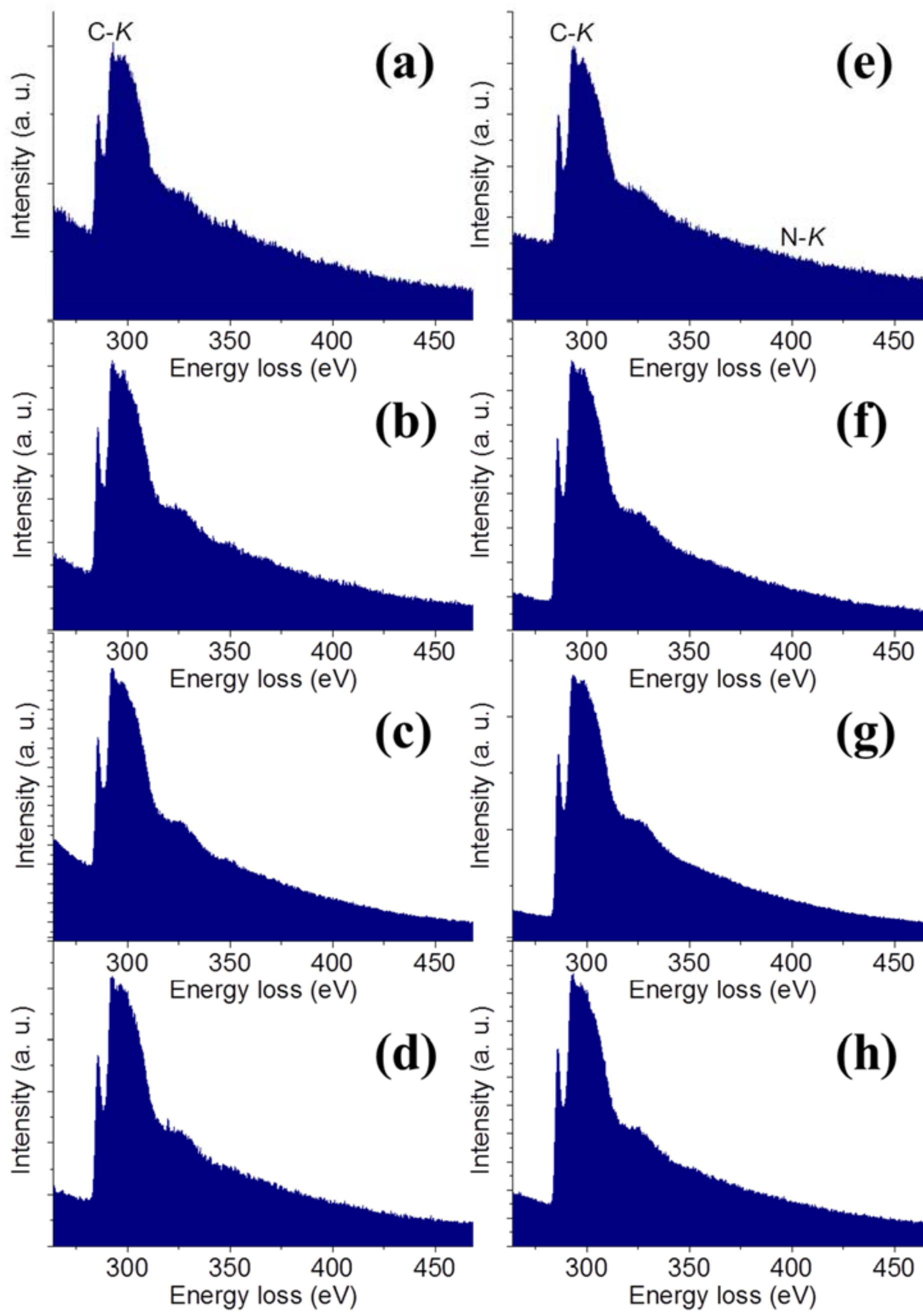

Figure 3.21. Electron energy loss spectrum of the HASWNTs. (a)-(d) EELS of pristine HASWNT, and (e)-(h) 50 % acetonitrile-induced HASWNT.

resolusion, and sample damage. We performed EELS measurements both of the carbon

K-edge and of nitrogen K-edge. In particular, the relatie strength of the initial peak has been established as a measure of the predominance of sp^2 as opposed to sp^3 hybridization. A strong initial peak should correspond to a high quzlity material, since ideal carbon nanotubes are purely sp^2 hybridized. Figure 3.21(a)-(d) show the EELS results from pristine from point to point across a sample. The carbon K-edge spectra show that the pristine material is much more strong sp^2 hybridized (indicated by the strength of the initial peak). The nitrogen-doped carbon nanotubes contains pyridinic,pyrrolic, and N_2 nitrogen species [134] with a nominal nitrogen level of 0.08~0.62 at % from previous result. Nitrogen groups in the nanotubes result from acetonitrile during synthesis and defects occur. Nitrogern species were identified by EELS with N-HASWNTs as shown in Figure 3.21(e)-(h). However, any nitrogen core signal could be detected in the sample. This will be discussed in more detail

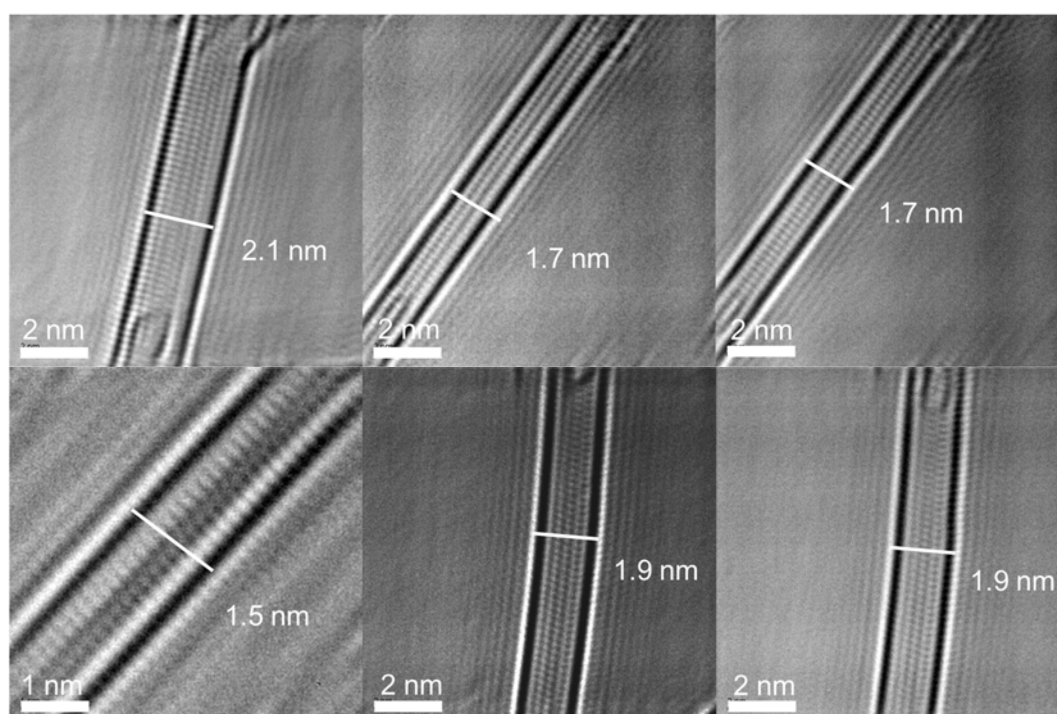

Figure 3.22. HR TEM images of pristine HASWNTs grown by only ethanol as carbon source with ACCVD.

later.

3.3.7 HRTEM images of HASWNT

Pristine and 50 % N-HASWNTs were measured with high resolution transmittance electron microscopy (HRTEM; lattice resolution: 0.2 nm; accelerating voltage: 80 kV), respectively. Figure 3.22 and 3.23 present the images of TEM from the ethanol-based pristine

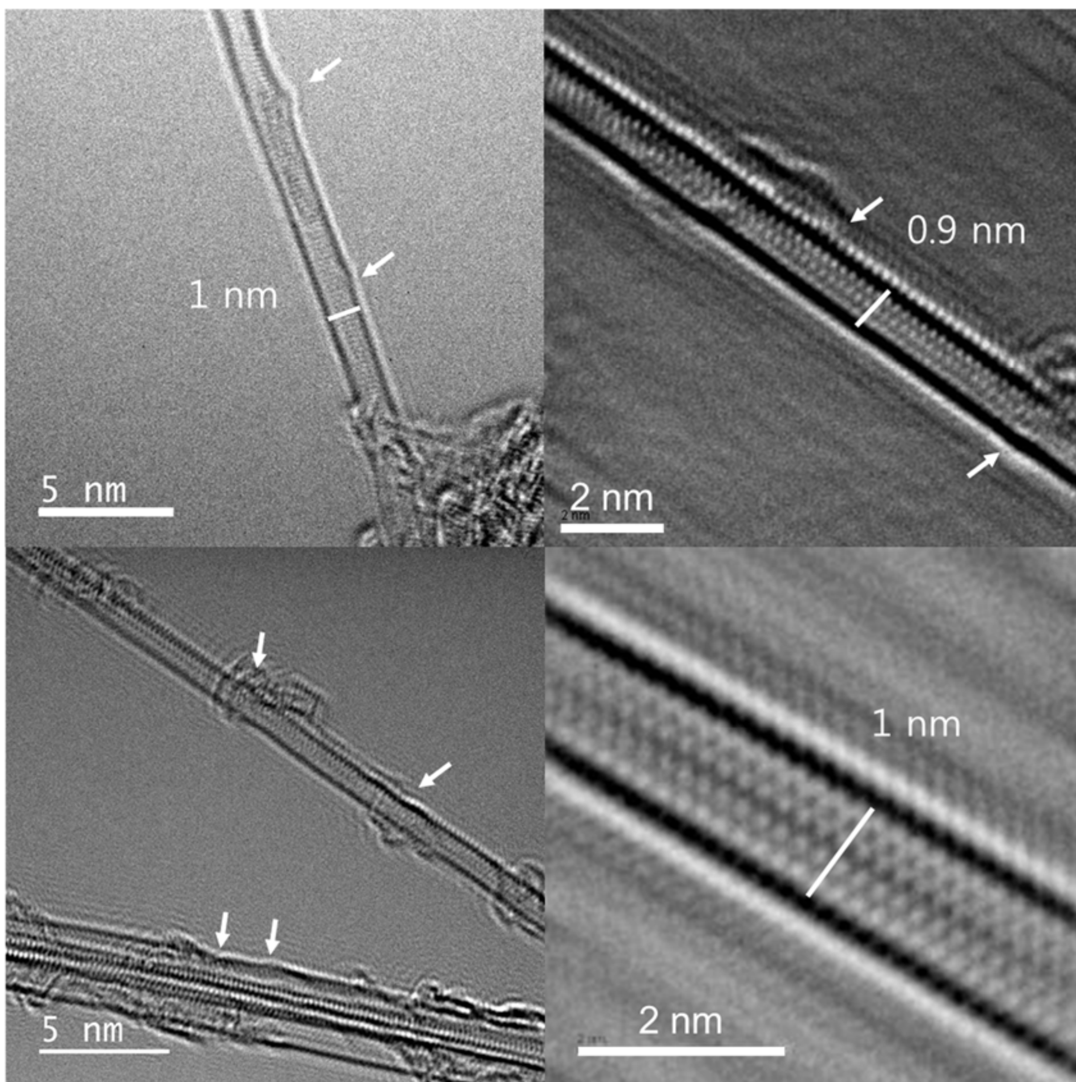

Figure 3.23. HR TEM images of 50 % acetonitrile-induced HASWNTs grown with ethanol and acetonitrile as carbon and nitrogen source, respectively.

HASWNTs and 50 % acetonitrile-induced HASWNTs by acetonitrile and ethanol, respectively. However, isolated nanotubes tend to vibrate or shift position due to heating from the electron beam. The crystallinity of the HASWNT surface was enhanced since the pristine sample was grown by only ethanol as a carbon source. Some defect states still remained in the SWNT surface. As a consequence, surface morphology of the sample shows straight. On the other hand, the crystallinity of the 50 % acetonitrile-induced HASWNTs surface grown by acetonitrile and ethanol was weakened as shown in figure 3.23. The

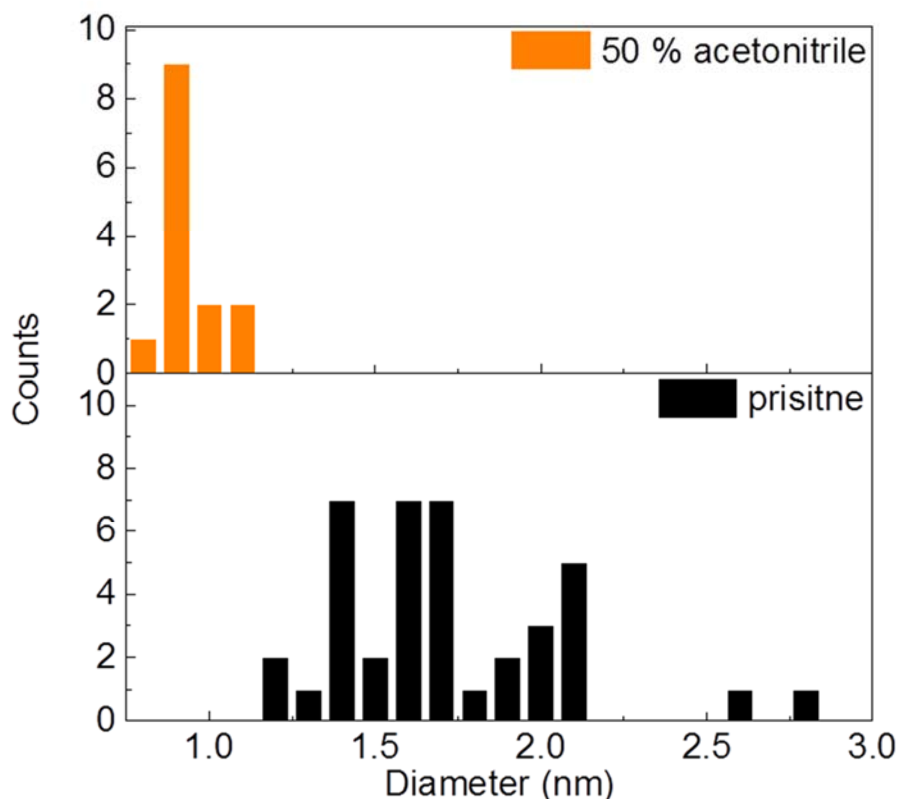

Figure 3.24. Comparison of the diameter distribution between pristine and 50 % N-HASWNTs. For pristine sample, mean diameter is ~ 1.7 nm with standard deviation 0.4 nm. For 50 % N-HASWNT, mean diameter ~ < 1 nm.

nitrogen-doped SWNT walls were damaged during synthesis with acetonitrile. Vacancies, kinks, and amorphous carbons were likely to be created, where some of them were visible in Figure 3.23. The generation of defects can be monitored with further acetonitrile by the disorder band in Raman spectroscopy as well, in Figure 3.13(a) and (b).

Figure 3.24 presents diameter distribution of the pristine and 50 % N-HASWNTs, respectively. In case of the pristine sample, mean diameter is ~ 1.7 nm with standard deviation 0.4 nm and smallest diameter of the HASWNT is > 1.2 nm. Most diameters of 50 % N-HASWNT is shown < ~ 1 nm. This result of TEM shows a similar tendency to that

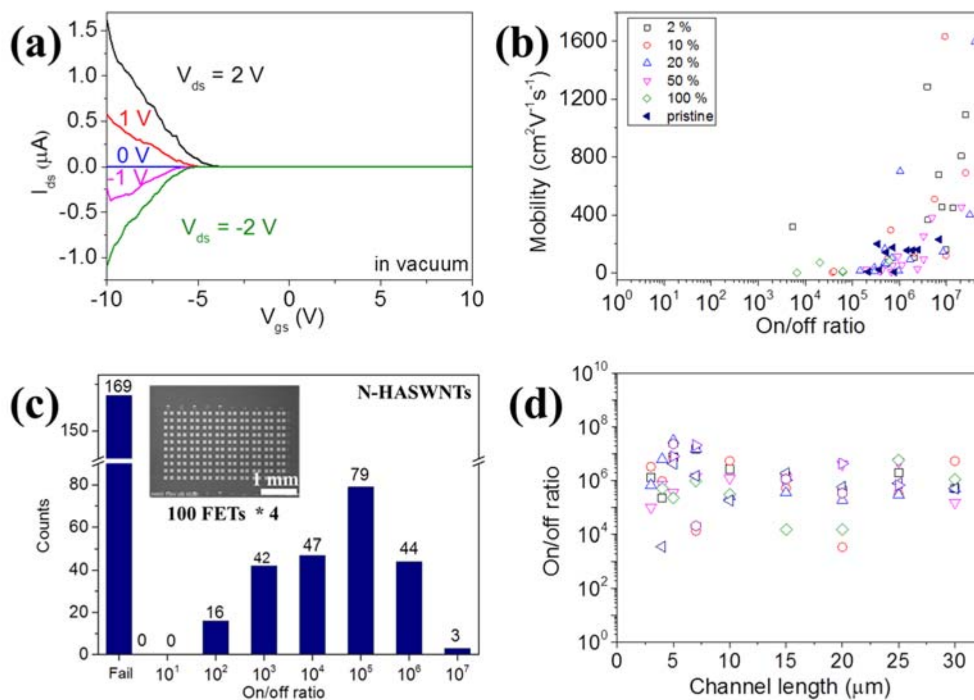

Figure 3.25. (a) I_{ds}-V_{gs} characteristics of 2 % N-HASWNT devices (V_{ds} range: -2~2 V). (b) Mobility plotted against I_{on}/I_{off} ratio of measured devices. (c) The number of devices as a function of the on/off ratio and optical micrograph image of an array of 100 devices (inset). (d) The influence of channel length on the on/off ratio.

of Raman spectra for between pristine and 50 % acetonitrile and ethanol sample.

3.3.8 Mobility vs on/off ratio of N-HASWNT transistors

The I_{ds}-V_{gs} curve in Figure 3.25(a) shows p-type characteristics with an on/off ratio about 10^6, while utilizing V_{ds} = 2 V. The contacts are clearly asymmetric due to the large difference in on/off ratio for -2 V and 2 V, V_{ds} bias. The mobilities of HASWNT devices were derived from the slope of source-drain variation from gate voltage to the linear regime using the equation $\mu = \frac{L_c}{WCV_{ds}}\frac{\Delta I_{ds}}{\Delta V_{gs}}$. Here L_c and W are the channel length and width, $\frac{\Delta I_{ds}}{\Delta V_{gs}}$ is the transconductance, V_{ds} is the source-drain voltage, and c is the gate capacitance.

The yield of working electrodes was ~ 60 %, and average mobilities of N-HASWNT and pristine were ~ 282 $cm^2/V{\cdot}s$ and 125 $cm^2/V{\cdot}s$ in Figure 3.25(b), respectively. The back gate test showed that

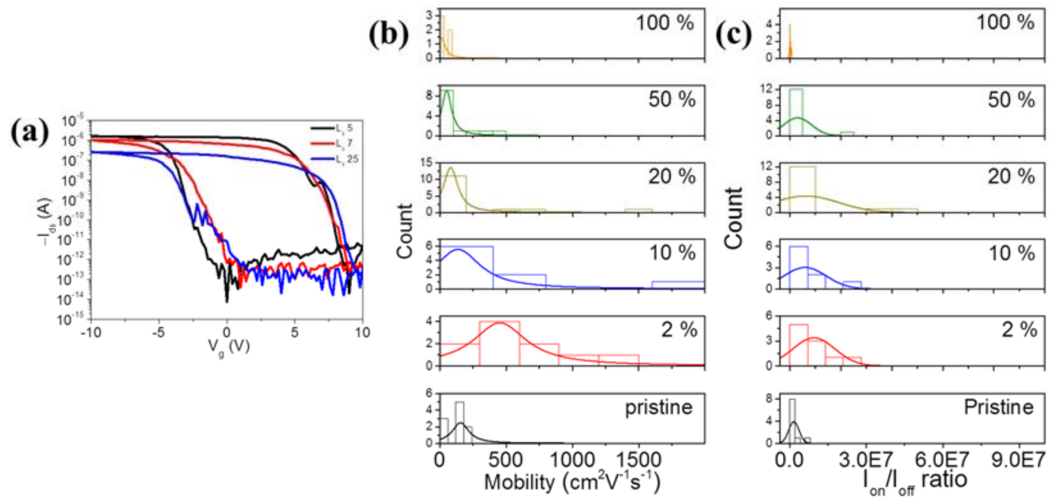

Figure 3.26. (a) Transfer characteristics of HASWNT with high performance. (b) Mobility and I_{on}/I_{off} ratio distribution as a function of different growth condition for HASWNTs devices.

93 % of the connected N-HASWNT FETs had an on/off ratio > 10^3 and 55 % had an on/off ratio > 10^5 as shown in Figure 3.25(c). The main reason for the high on/off ratios observed here is unclear so far. The on/off ratio was independent with increasing channel length as shown in Figure 3.25(d). Figure 3.26(a) shows transfer curves of HASWNT with high performance, for instance, high mobilities with I_{on}/I_{off} ratio. Figure 3.26(b) and (c) show mobility and I_{on}/I_{off} distribution as a function of acetonitrile concentration increases. Even though metallic nanotubes were retained in the sample, the probability of have semiconducting channels in the transistor increased with the channel. Figure 3.27 show electrical properties of nitrogen-induced HASWNT devices in ambient air condition.

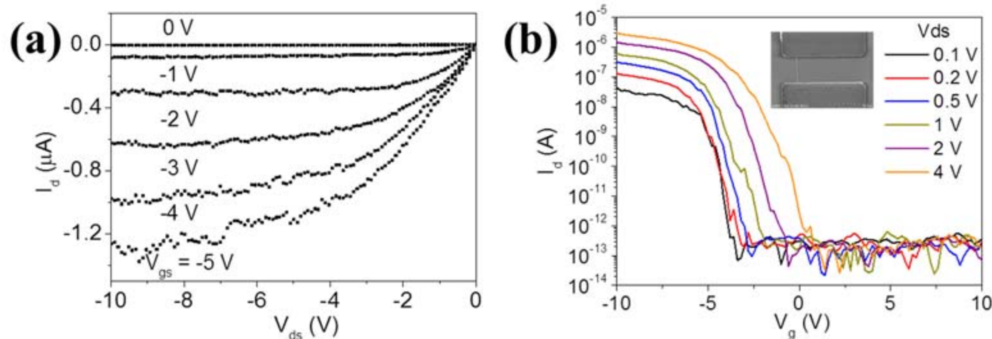

Figure 3.27. Electrical properties of 20 % acetonitrile induced HASWNT devices (L_c: 7 μm and W: 20 μm). (a) Output characteristics with V_{ds} sweep from 0 to 10 V. (b) Transfer characteristics at various drain voltage. V_{GS} was applied from -10 to 10 V with a 200 mV step in both cases.

3.3.9 Band diagram of nitrogen-doped SWNTs

To be confirmed..

3.4 Conclusion and originality of this chapter

In summary, a diameter of nitrogen-induced horizontally aligned SWNTs could be

controlled by different acetonitrile consistency with CVD. Nitrogen doping maybe produce n-type carbon nanotubes by shifting the Fermi level to the conduction band to identify nitrogen-induced HASWNT device throughout threshold voltage shift. Contrary to the expectation for the n-type doping nature of nitrogen atom, the electrical transports through N-HASWNTs are p-type in air and ambipolar or unipolar in vacuum. However, the N-HASNWT FETs is shown high performance, for instance, high mobilities with high on/off ratio compared ethanol-based SWNT devices. Nitrogen-induced small diameter CNTs with narrow diameter distribution, for instance, wide bandgap semiconducting materials have several characteristics that make them useful compared smaller bandgap materials or for bandgap control. The higher energy gap gives devices the ability to operate at higher temperature, and for some applications, allows devices to switch larger voltages. The wide bandgap also brings the electronic transition energy into the range of the energy of visible light.

Chapter 4

Closing remarks

4.1 Summaries of this thesis

The research conducted in this PhD thesis includes various improvements and discoveries to the synthesis, fabrication and characterization of doped monolayer graphene and SWNTs. After a brief introduction of the geometric and electronic structures of graphene and SWNTs in Chapter 1, a protocol was presented in Chapter 2 to control the electrical transport behaviors of as-grown CVD monolayer graphene transistors with specific PVA films under ambient condition. This conversion switching behavior was achieved using a PVA film by concentration of polymer solution and baking temperature. A Raman spectrum shows an evidence of charge transfer between monolayer graphene and polymer film after coating polymer solution. After PVA doping, mobility was increased due to the majority carrier increase. Long term stability of the n-doped graphene transistors above three months has also been achieved in case of high concentration (20 wt%) of PVA solution. This highly stable n-doped graphene device was originated not only from charge transfer but also PVA films played as passivation layer against p-doping from ambient condition.

The discussion on transport properties of nitrogen-doped HASWNTs was continued in Chapter 3 by systematically investigating how to configure nitrogen atoms on carbon

nanotubes. HASWNTs-based FETs are expected to enable the fabrication of high performance device using relatively simple techniques. However, as-grown nanotubes usually contain both metallic and semiconducting nanotubes, which lead to a trade-off between charge carrier mobility and I_{on}/I_{off} ratio. This part represents the synthesis and fabrication of nitrogen-induced HASWNT FETs. The growth of N-HASWNTs using chemical vapor deposition on an r-cut crystal quartz substrate, followed by peel off and transfer to a target substrate. Nitrogen dopant, either in the form of a chemical adatom or the pyridinelike configuration, would lead to p-type, whereas the substitutional nitrogen dopant induces the n-type doping. Although our N-HASWNT FETs show p-type behaviors, the resulting N-HASWNTs have will-controlled density and a unique morphology, consisting of small diameter nanotubes with large bandgap (~ 1 eV). N-HASWNTs can be This FET simultaneously demonstrates a mobility of 1,284 $cm^2V^{-1}s^{-1}$ and an on/off ratio ~ 10^6. We also demonstrate flexible FETs using N-HASWNT with high performance.

4.2 Future work of this thesis

- Fabrication and characterization of p-n junction diode with graphene and PVA thin film
- Complementary graphene inverter and characterization of circuit performance
- Mechanism study of interaction between graphene and PVA as a function of PVA consistency
- Optimization of the horizontally aligned carbon nanotube density to apply FETs
- Mechanism identification of nitrogen configuration in nitrogen-induced HASWNTs synthesis
- Growth of heterostructure HASWNT using cloning method

References

1 D. C. Mowery, R. R. Nelson, Sources of industrial leadership. Cambridge University Press Cambridge, UK , 1999.

2 H. W. Kroto, J. R. Heath, S. C. O`Brien, R. F. Curl, R. E. Smally, C60: Buckminsterfullerene. *Nature* **318**, 162-163 (1985).

3 D. S. Bethune, R. D. Johnson, J. R. Salem, M. S. de Vries, C. S. Yannoni, Atoms in carbon cages: the structure and properties of endohedral fullerenes. *Nature* **366**, 123-128 (1993).

4 S. Iijima, Helical microtubules of graphitic carbon. *Nature* **354**, 56-58 (1991).

5 J.-C. Charlier, X. Blase, S. Roche, Electronic and transport properties of nanotubes. *Reviews of Modern Physics* **79**, 677-732, (2007).

6 A. Javey, J. Kong, Carbon Nanotube Electronics. Springer, New York, 2009.

7 A. H. Castro Neto, F. Guinea, N. M. R. Peres, K. S. Novoselov, A. K. Geim, The electronic properties of graphene. *Reviews of Modern Physics* **81**, 109-162, (2009).

8 P. R. Wallace, The Band Theory of Graphite. *Physical Review* **71**, 622-634, (1947).

9 R. Saito, M. Fujita, G. Dresselhaus, M. S. Dresselhaus, Electronic structure of chiral graphene tubules. *Appl. Phys. Lett.* **60**, 2204-2206, (1992).

10 C. L. Kane, E. J. Mele, R. S. Lee, J. E. Fischer, P. Petit, H. Dai, A. Thess,R. E. Smalley, A. R. M. Verschueren, S. J. Tans, C. Dekker, Temperature-dependent resistivity of single-wall carbon nanotube. *Europhys. Lett.* **41** (6), 683-688 (1998).

11 S. Reich, J. Maultzsch, C. Thomsen, P. Ordejón, Tight-binding description of graphene. *Phys. Rev. B* **66**, 035412 (2002).

12 R. Saito, M. Fujita, G. Dresselhaus, M. S. Dresselhaus, Electronic structure of graphene tubules based on C_{60}. *Phys. Rev. B* **46**, 1804-1811, (1992).

13 R. Saito, M. S. Dresselhaus, G. Dresselhaus, Physical Properties of Carbon Nanotubes. Imperial College Press, London, 1998.

14 R. E. Peierls, Quantum Theory of Solids. Oxford University Press, London, 2001.

15 M. S. Dresselhaus, Graphite fibers and filaments. Springer-Verlag Berlin, New York, 1988.

16 M. S. Dresselhaus, G. Dresselhaus, P. C. Eklund, Science of Fullerenes and Carbon Nanotubes. Academic Press, San Diego, CA, 1996.

17 M. S. Dresselhaus, G. Dresselhaus, R. Saito, A. Jorio, Raman spectroscopy of carbon nanotubes. *Physics Reports* **409**, 47-99, (2005).

18 A. Jorio, M. A. Pimenta, A. G. Souza Filho, R. Saito, G. Dresselhaus, M. S. Dresselhaus, Characterizing carbon nanotube sampes with resonance raman scattering. *New J. Phys.* **5**, 139, (2003).

19 L. M. Malard, M. A. Pimenta, G. Dresselhaus, M. S. Dresselhaus, Raman spectroscopy in graphene. *Physics Reports* **473**, 51-87, (2009).

20 A. C. Ferrari, J. Robertson, Raman spectroscopy of amorphous, nanostructured, diamond-like carbon, and nanodiamond. *Philosophical transactions. Series A, Mathematical, physical, and engineering sciences* **362**, 2477-2512, (2004).

21 A. Jorio, G. Dresselhaus, M. S. Dresselhaus, Carbon Nanotubes - Advanced Topics in the Synthesis, Structure, Properties and Applications. Springer, 2008.

22 H. Kataura, Y. Kumazawa, Y. Maniwa, I. Umezu, S. Suzuki, Y. Ohtsuka, Y. Achiba,

Optical properties of single-wall carbon nanotubes. *Synthetic Metal* **103**, 2555-2558, (1999).

23 Maruyama-Shiomi Laboratory homepage (http://www.photon.t.u-tokyo.ac.jp).

24 M. Bockrath, D. H. Cobden, P. L. McEuen, N. G. Chopra, A. Zettl, A. Thess, R. E. Smalley, Single-Electron Transport in Ropes of Carbon Nanotubes. *Science* **275**, 1922-1925, (1997).

25 R. Martel, T. Schmidt, H. R. Shea, T. Hertel, Ph. Avouris, Single- and multi-wall carbon nanotube field-effect transistors. *Appl. Phys. Lett.* **73**, 2447-2449, (1998).

26 S. J. Tans, M. H. Devoret, H. Dai, A. Thess, R. E. Smalley, L. J. Geerligs, C. Dekker, Individual single-wall carbon nanotubes as quantum wires. *Nature* **386**, 474-477, (1997).

27 S. J. Tans, A. R. M. Verschueren, C. Dekker, Room-temperture transistor based on a single carbon nanotube. *Nature* **393**, 49-52, (1998).

28 C. Zhou, J. Kong, H. Dai, Intrinsic Electrical Properties of Individual Single-Walled Carbon Nanotubes with Small Band Gaps. *Phys. Rev. Lett.* **84**, 5604-5607, (2000).

29 K. S. Novoselov, A. K. Geim, S. V. Morozov, D. Jiang, M. I. Katsnelson, I. V. Grigorieva, S. V. Dubonos, A. A. Firsov, Two-dimensional gas of massless Dirac fermions in graphene. *Nature* **438**, 197-200, (2005).

30 C. Berger, Z. Song, X. Li, X. Wu, N. Brown, C. Naud, D. Mayou, T. Li, J. Hass, A. N. Marchenkov, E. H. Conrad, P. N. First, W. A. de Heer, Electronic confinement and coherence in patterned epitaxial graphene. *Science* **312**, 1191-1196, (2006).

31 F. Xia, D. B. Farmer, Y. Lin, Ph. Avouris, Graphene field-effect transistors with high on/off current ratio and large transport band gap at room temperature. *Nano lett.* **10**, 715-718, (2010).

32 T. Fang, A. Konar, H. Xing, D. Jena, Carrier statistics and quantum capacitance of graphene sheets and ribbons. *Appl. Phys. Lett.* **91**, 092109, (2007).

33 W. Zhu, V. Perebeinos, M. Freitag, Ph. Avouris, Carrier scattering, mobilities, and electrostatic potential in monolayer, bilayer, and trilayer graphene. *Phys. Rev. B* **80**, 235402 (2009).

34 C. Zhou, J. Kong, E. Yenilmez, H. Dai, Modulated Chemical Doping of Individual Carbon Nanotubes. *Science* **290**, 1552-1555, (2000).

35 J. Kong, J. Cao, H. Dai, E. Anderson, Chemical profiling of single nanotubes: Intramolecular p–n–p junctions and on-tube single-electron transistors. *Appl. Phys. Lett.* **80**, 73-75, (2002).

36 J. Kong, C. Zhou, E. Yenilmez, H. Dai, Alkaline metal-doped n-type semiconducting nanotubes as quantum dots. *Appl. Phys. Lett.* **77**, 3977-3979, (2000).

37 J. Kong, N. R. Franklin, C. Zhou, M. G. Chapline, S. Peng, K. Cho, H. Dai, Nanotube Molecular Wires as Chemical Sensors. *Science* **287**, 622-625, (2000).

38 J. Kong, H. Dai, Full and Modulated Chemical Gating of Individual Carbon Nanotubes by Organic Amine Compounds. *J. Phys. Chem. B* **105**, 2890-2893, (2001).

39 M. Shim, A. Javey, N. W. S. Kam, H. Dai, Polymer Functionalization for Air-Stable n-Type Carbon Nanotube Field-Effect Transistors. *J. Am. Chem. Soc.* **123**, 11512-11513, (2001).

40 M. Radosavljević, J. Appenzeller, Ph. Avouris, J. Knoch, High performance of potassium n-doped carbon nanotube field-effect transistors. *Appl. Phys. Lett.* **84**, 3693-3695, (2004).

41 V. Derycke, R. Martel, J. Appenzeller, Ph. Avouris, Carbon Nanotube Inter- and Intramolecular Logic Gates. *Nano lett.* **1**, 453-456, (2001).

42 A. Javey, R. Tu, D. B. Farmer, J. Guo, R. G. Gordon, H. Dai, High performance n-type carbon nanotube field-effect transistors with chemically doped contacts.*Nano lett.* **5**, 345-348, (2005).

43 Y. Nosho, Y. Ohno, S. Kishimoto, T. Mizutani1, Relation between conduction property and work function of contact metal in carbon nanotube field-effect transistors. *Nanotechnology* **17**, 3412-3415, (2006).

44 Y.-M. Lin, J. Appenzeller, J. Knoch, Ph. Avouris, Trans. Nanotechnol_High performance carbon nanotube field-effect transistor with tunable polarities. *IEEE Transactions on Nanotechnology* **4**, 481-489,(2005).

45 K. Yamoto, T. Kamimura, K. Matsumoto, Nitrogen Doping of Single-Walled Carbon Nanotube by Using Mass-Separated Low-Energy Ion Beams. *Jpn. J. Appl. Phys.* **44**, 1611-1614, (2005).

46 W. J. Yu, B. R. Kang, I. H. Lee, Y.-S. Min, Y. H. Lee, Majority carrier type conversion with floating gates in carbon nanotube transistors. *Advanced materials* **21**, 4821-4824, (2009).

47 S. M. Sze, K. K. Ng, Physics of Semiconductor Devices, 3rd Edition, Wiley-Interscience, Hoboken, NJ, 2007.

48 F. Schedin, A. K. Geim, S. V. Morozov, E. W. Hill, P. Blake, M. I. Katsnelson, K. S. Novoselov, Detection of individual gas molecules adsorbed on graphene. *Nature materials* **6**, 652-655, (2007).

49 P. L. Levesque, S. S. Sabri, C. M. Aguirre, J. Guillemette, M. Siaj, P. Desjardins, T. Szkopek,R. Martel, Probing charge transfer at surfaces using graphene transistors. *Nano lett.* **11**, 132-137, (2011).

50 Y. Dan, Y. Lu, N. J. Kybert, Z. Luo, A. T. Charlie Johnson, Intrinsic Response of

Graphene Vapor Sensors. *Nano lett.* **9**, 1472-1475, (2009).

51 M. Ishigami, J. H. Chen, W. G. Cullen, M. S. Fuhrer, E. D. Williams, Atomic structure of graphene on SiO_2. *Nano lett.* **7**, 1643-1648, (2007).

52 J. Martin, N. Akerman, G. Ulbricht, T. Lohmann, J. H. Smet, K. Vonklitzing, A. Yacoby, Observation of electron–hole puddles in graphene using a scanning single-electron transistor. *Nature Physics* **4**, 144-148, (2007).

53 M. Lafkioti, B. Krauss, T. Lohmann, U. Zschieschang, H. Klauk, K. v. Klitzing, J. H. Smet, Graphene on a hydrophobic substrate: doping reduction and hysteresis suppression under ambient conditions. *Nano lett.* **10**, 1149-1153, (2010).

54 Z. Liu, A. A. Bol, W. Haensch, Large-scale graphene transistors with enhanced performance and reliability based on interface engineering by phenylsilane self-assembled monolayers. *Nano lett.* **11**, 523-528, (2011).

55 C. R. Dean, A. F. Young, I. Meric, C. Lee, L. Wang, S. Sorgenfrei1, K. Watanabe, T. Taniguchi, P. Kim, K. L. Shepard, J. Hone, Boron nitride substrates for high-quality graphene electronics. *Nature nanotechnol.* **5**, 722-726, (2010).

56 X. Hong, A. Posadas, K. Zou, C. H. Ahn, J. Zhu, High-Mobility Few-Layer Graphene Field Effect Transistors Fabricated on Epitaxial Ferroelectric Gate Oxides. *Phys. Rev. Lett.* **102**, 136808 (2009).

57 F. Chen, J. Xia, N. Tao, Ionic Screening of Charged-Impurity Scattering in Graphene. *Nano lett.* **9**, 1621-1625, (2009).

58 B. Guo, Q. Liu, E. Chen, H. Zhu, L. Fang, J. R. Gong, Controllable N-Doping of Graphene. *Nano lett.* **10**, 4975-4980 (2010).

59 D. B. Farmer, R. Golizadeh-Mojarad, V. Perebeinos, Y.-M. Lin, G. S. Tulevski, J. C. Tsang, Ph. Avouris, Chemical dopi,ng and electron-hole conduction asymmetry in

graphene devices. *Nano lett.* **9**, 388-392, (2009).

60 A. Kasry, M. A. Kuroda, G. J. Martyna, G. S. Tulevski, A. A. Bol, Chemical Doping of Large-Area Stacked Graphene Films for Use as Transpatent Conducting Flectrodes. *ACS nano* **4**, 3839-3844, (2010).

61 Y. Shi, K. K. Kim, A. Reina, M. Hofmann, L.-J. Li, J. Kong, Work Function Engineering of Graphene Electrode Via Chemical Doping. *ACS nano* **4**, 2689-2694, (2010).

62 F. Gu¨nes¸ H.-J. Shin, C. Biswas, G. H. H, E. S. Kim, S. J. Chae, J.-Y. Choi, Y. H. Lee, Layer-by-Layer Doping of Few-Layer Graphene Film. *ACS nano* **4**, 4595-4600, (2010).

63 C. Coletti, C. Riedl, D. S. Lee, B. Krauss, L. Patthey, K. von Klitzing, J. H. Smet, U. Starke1, Charge neutrality and band-gap tuning of epitaxial graphene on SiC by molecular doping. *Phys. Rev. B* **81**,235401, (2010).

64 W. Chen, S. Chen, D. C. Qi, X. Y. Gao, A. T. S. Wee, Surface Transfer p-Type Doping of Epitaxial Graphene. *J. Am. Chem. Soc.* **129**, 10418-10422, (2007).

65 I. Gierz, C. Riedl, U. Starke, C. R. Ast, K. Kern, Atomic hole doping of graphene. *Nano lett.* **8**, 4603-4607, (2008).

66 X. Wang, X. Li, L. Zhang, Y. Yoon, Peter. K. Weber, H. Wang, J. Guo, H. Dai, N-doping of graphene through electrothermal reactions with ammonia. *Science* **324**, 768-771, (2009).

67 S. Ryu, M. Y. Han, J. Maultzsch, T. F. Heinz, P. Kim, M. L. Steigerwald, L. E. Brus, Reversible basal plane hydrogenation of graphene. *Nano lett.* **8**, 4597-4602, (2008).

68 M. J. Loboda, C. M. Grove, R. F. Schneider, Properties of a-SiOx: H thin films deposited hydrogen silsesquioxane resins. *J. Electrochem. Soc.* **145**, 2861-2866,

(1998).

69 K. Brenner, R. Muralia, Single step, complementary doping of graphene. *Appl. Phys. Lett.* **96**, 063104, (2010).

70 H.-J. Lee, E. K. Lin, H. Wang, W.-l. Wu, W. Chen, E. S. Moyer, Structural comparison of hydrogen silsesquioxane based porous low-k thin films prepared with varying process conditions. *Chem. Mater.* **14**, 1845-1852, (2002).

71 Ph. Avouris, Z. Chen, V. Perebeinos, Carbon-based electronics. *Nature nanotechnol.* **2**, 605-615, (2007).

72 A. K. Geim, K. S. Novoselov, The rise of graphene. *Nature mater.* **6**, 183-191, (2007).

73 K. S. Novoselov, V. I. Fal`ko, L. Colombo, P. R. Gellert, M. G. Schwab, K. Kim, A roadmap for graphene. *Nature* **490**, 192-200, (2012).

74 S. V. Morozov, K. S. Novoselov, M. I. Katsnelson, F. Schedin, D. C. Elias, J. A. Jaszczak, A. K. Geim, Giant Intrinsic Carrier Mobilities in Graphene and Its Bilayer. *Phys. Rev. Lett.* **100**, 016602 (2008).

75 X. Du, I. Skachko, A. Barker, E. Y. Andrel, Approaching ballistic transport in suspended graphene. *Nature nanotechnol.* **3**, 491-495, (2008).

76 X. Du, I. Skachko, F. Duerr, A. Luican, E. Y. Andrei1, Fractional quantum Hall effect and insulating phase of Dirac electrons in graphene. *Nature* **462**, 192-195, (2009).

77 K. I. Bolotin, F. Ghahari, M. D. Shulman, H. L. Stormer, P. Kim, Observation of the fractional quantum Hall effect in graphene. *Nature* **462**, 196-199, (2009).

78 C. Lee, X. Wei, J. W. Kysar, J. Hone, Measurement of the elastic properties and intrinsic strength of monolayer graphene. *Science* **321**, 385-388, (2008).

79 M. Y. Han, B. O¨zyilmaz, Y. Zhang, P. Kim, Energy Band-Gap Engineering of Graphene Nanoribbons. *Phys. Rev. Lett.* **98**, 206805 (2007).

80 Z. Chen, Y.-M. Lin, M. J. Rooks, Ph. Avouris, Graphene nano-ribbon electronics. *Physica E: Low-dimensional Systems and Nanostructures* **40**, 228-232, (2007).

81 X. Li, X. Wang, L. Zhang, S. Lee, H. Dai, Chemically derived, ultrasmooth graphene nanoribbon semiconductors. *Science* **319**, 1229-1232, (2008).

82 X. Wang, Y. Ouyang, X. Li, H. Wang, J. Guo, H. Dai, Room-Temperature All-Semiconducting Sub-10-nm Graphene Nanoribbon Field-Effect Transistors. *Phys. Rev. Lett.* **100**, 206803 (2008).

83 T. Ohta, A. Bostwick, T. Seyller, K. Horn, E. Rotenberg, Controlling the electronic structure of bilayer graphene. *Science* **313**, 951-954, (2006).

84 E. V. Castro, K. S. Novoselov, S. V. Morozov, N. M. R. Peres, J. M. B. Lopes dos Santos, J. Nilsson, F. Guinea, A. K. Geim, A. H. Castro Neto, Biased Bilayer Graphene: Semiconductor with a Gap Tunable by the Electric Field Effect. *Phys. Rev. Lett.* **99**, 216802 (2007).

85 Y. Zhang, T.-T. Tang, C. Girit, Z. Hao, M. C. Martin, A. Zettl, M. F. Crommie, Y. Ron Shen, F. Wang, Direct observation of a widely tunable bandgap in bilayer graphene. *Nature* **459**, 820-823, (2009).

86 J. Bai1, X. Zhong, S. Jiang, Y. Huang, X. Duan, Graphene nanomesh. *Nature nanotechnol.* **5**, 190-194, (2010).

87 X. Dong, D. Fu, W. Fang, Y. Shi, P. Chen, L.-J. Li, Doping single-layer graphene with aromatic molecules. *Small* **5**, 1422-1426, (2009).

88 Z. Yan, J. Yao, Z. Sun, Y. Zhu, J. M. Tour, Controlled ambipolar-to-unipolar conversion in graphene field-effect transistors through surface coating with poly(ethylene imine)/poly(ethylene glycol) films. *Small* **8**, 59-62, (2012).

89 J.-H. Chen, C. Jang, S. Adam, M. S. Fuhrer, E. D. Williams, M. Ishigami,

Charged-impurity scattering in graphene. *Nature Physics* 4, 377-381, (2008).

90 P. Zhao, A. Kumamoto, S. Kim, X. Chen, B. Hou, S. Chiashi, E. Einarsson, Y. Ikuhara, S. Maruyama, Self-Limiting Chemical Vapor Deposition Growth of Monolayer Graphene from Ethanol. *J. Phys. Chem. C* 117, 10755-10763, (2013).

91 X. Li, W. Cai, J. An, S. Kim, J. Nah, D. Yang, R. Piner, A. Velamakanni, I. Jung, E. Tutuc, S. K. Banerjee, L. Colombo, R. S. Ruoff, Large-area synthesis of high-quality and uniform graphene films on copper foils. *Science* 324, 1312-1314, (2009).

92 X. Li, C. W. Magnuson, A. Venugopal, R. M. Tromp, J. B. Hannon, E. M. Vogel, L. Colombo, R. S. Ruoff, Large-area graphene single crystals grown by low-pressure chemical vapor deposition of methane on copper. *J. Am. Chem. Soc.* 133, 2816-2819, (2011).

93 X. Li, C. W. Magnuson, A. Venugopal, J. An, J. W. Suk, B. Han, M. Borysiak, W. Cai, A. Velamakanni, Y. Zhu, L. Fu, E. M. Vogel, E. Voelkl, L. Colombo, R. S. Ruoff, Graphene films with large domain size by a two-step chemical vapor deposition process. *Nano lett.* 10, 4328-4334, (2010).

94 X. Peng, G. Horowitz, D. Fichou, F. Garnier, All-organic thin-film transistors made of alpha-sexithienyl semiconducting and various polymeric insulating layers. *Appl. Phys. Lett.* 57, 2013-2015, (1990).

95 M. L. Swiggers, G. Xia, J. D. Slinker, A. A. Gorodetsky, G. G. Malliaras, R. L. Headrick, Brian T. Weslowski, R. N. Shashidhar, C. S. Dulceya, Orientation of pentacene films using surface alignment layers and its influence on thin-film transistor characteristics. *Appl. Phys. Lett.* 79, 1300, (2001).

96 P. Blake, P. D. Brimicombe, R. R. Nair, T. J. Booth, D. Jiang, F. Schedin, L. A. Ponomarenko, S. V. Morozov, H. F. Gleeson, E. W. Hill, A. K. Geim, K. S. Novoselov,

Graphene-based liquid crystal device. *Nano Lett.* **8**, 1704-1708, (2008).

97 I. Meric, C. R. Dean, A. F. Young, N. Baklitskaya, N. J. Tremblay, C. Nuckolls, P. Kim, K. L. Shepard, Channel length scaling in graphene field-effect transistors studied with pulsed current-voltage measurements. *Nano lett.* **11**, 1093-1097, (2011).

98 S. Aikawa, E. Einarsson, T. Thurakitseree, S. Chiashi, E. Nishikawa, S. Maruyama Deformable transparent all-carbon-nanotube transistors. *Appl. Phys. Lett.* **100**, 063502, (2012).

99 E. S. Snow, P. M. campbell, M. G. Ancona, J. P. Novak, High-mobility carbon-nanotube thin-film transistors on a polymeric substrate. *Appl. Phys. Lett.* **86**, 033105, (2005).

100 I. Meric, M. Y. Han, A. F. Young, B. Ozyilmaz, P. Kim, K. L. Shepard, Current saturation in zero-bandgap, top-gated graphene field-effect transistors. *Nature nanotechnol.* **3**, 654-659, (2008).

101 V. Perebeinos, Ph. Avouris, Inelastic scattering and current saturation in graphene. *Phys. Rev. B* **81**, 195442 ,(2010).

102 A. C. Ferrari, J. C. Meyer, V. Scardaci, C. Casiraghi, M. Lazzeri, F. Mauri, S. Piscanec, D. Jiang, K. S. Novoselov, S. Roth, A. K. Geim, Raman Spectrum of Graphene and Graphene Layers. *Phys. Rev. Lett.* **97**, 187401 (2006).

103 S. Pisana, M. Lazzeri, C. Casiraghi, K. S. Novoselov, A. K. Geim, A. C. Ferrari, F. Mauri, Breakdown of the adiabatic Born-Oppenheimer approximation in graphene. *Nature materials* **6**, 198-201, (2007).

104 A. Das, S. Pisana, B. Chakraborty, S. Piscanec, S. K. Saha, U. V. Waghmare, K. S. Novoselov, H. R. Krishnamurthy, A. K. Geim, A. C. Ferrari, A. K. Sood, Monitoring dopants by Raman scattering in an electrochemically top-gated graphene transistor.

Nature nanotechnol. **3**, 210-215, (2008).

105 J. R. Williams, L. DiCarlo, C. M. Marcus, Quantum Hall effect in a gate-controlled p-n junction of graphene. *Science* **317**, 638-641, (2007).

106 N. Rouhi, D. Jain, P. J. Burke, High-performance semiconducting nanotube inks: progress and prospects. *ACS nano* **5**, 8471-8487, (2011).

107 A. Javey, J. Guo, D. B. Farmer, Q. Wang, E. Yenilmez, R. G. Gordon, M. Lundstrom, H. Dai, Self-aligned ballistic molecular transistors and electrically parallel nanotube arrays. *Nano lett.* **4**, 1319-1322, (2004).

108 R. V. Seidel, A. P. Graham, J. Kretz, B. Rajasekharan, G. S. Duesberg, M. Liebau, E. Unger, F. Kreupl, W. Hoenlein, Sub-20nm short channel carbon nanotube transistors. *Nano lett.* **5**, 147-150, (2005).

109 A. Javey, J. Guo, D. B. Farmer, Q. Wang, D. Wang, R. G. Gordon, M. Lundstrom, H. Dai, Carbon Nanotube Field-Effect Transistors With Integrated Ohmic Contacts and High-k Gate Dielectrics. *Nano lett.* **4**, 447-450, (2004).

110 A. Bachtold, P. Hadley, T. Nakanishi, C. Dekker, Logic circuits with carbon nanotube transistors. *Science* **294**, 1317-1320, (2001).

111 S. Rosenblatt, H. Lin, V. Sazonova, S. Tiwari, P. L. McEuenb, Mixing at 50 GHz using a single-walled carbon nanotube transistor. *Appl. Phys. Lett.* **87**, 153111, (2005).

112 Z. Chen, J. Appenzeller, Y.-M. Lin,. J. Sippel-Oakley, A. G. Rinzler, J. Tang, S. J. Wind, P. M. Solomon, Ph. Avouris, An integrated logic circuit assembled on a single carbon nanaotube. *Science* **311**, 1735, (2006).

113 S. Heinze, J. Tersoff, R. Martel, V. Derycke, J. Appenzeller, Ph. Avouris, Carbon Nanotubes as Schottky Barrier Transistors. *Phys. Rev. Lett.* **89**, 106801 (2002).

114 V. Derycke, R. Martel, J. Appenzeller, Ph. Avouris, Controlling doping and carrier injection in carbon nanotube transistors. *Appl. Phys. Lett.* **80**, 2773, (2002).

115 S. M. Kim, J. H. Jang, K. K. Kim, H. K. Park, J. J. Bae, W. J. Yu, I. H. Lee, G. Kim, D. D. Loc, U. J. Kim, E.-H. Lee, H.-J. Shin, J.-Y. Choi, Y. H. Lee, Reduction-Controlled Viologen in Bisolvent as an Environmentally Stable n-Type Dopant for Carbon Nanotubes. *J. Am. Chem. Soc.* **131**, 327–331, (2009).

116 W. Kim, A. Javey, O. Vermesh, Q. Wang, Y. Li, H. Dai, Hysteresis caused by water molecules in carbonn nanotube field effect transistors. *Nano lett.* **3**, 193-198, (2003).

117 R. Czerw, M. Terrones, J.-C. Charlier, X. Blase, B. Foley, R. Kamalakaran, N. Grobert, H. Terrones, D. Tekleab, P. M. Ajayan, W. Blau, M. Ru2hle, and D. L. Carroll, Identification of Electron Donor States in N-Doped Carbon Nanotubes. *Nano lett.* **1**, 457-460, (2001).

118 M. Zhao, Y. Xia, J. P. Lewis, R. Zhang, First-principles calculations for nitrogen-containing single-walled carbon nanotubes. *Journal of Applied Physics* **94**, 2398, (2003).

119 T. Thurakitseree, C. Kramberger, P. Zhao, S. Aikawa, S. Harish, S. Chiashi, E. Einarsson, S. Maruyama, Diameter-controlled and nitrogen-doped vertically aligned single-walled carbon nanotubes. *Carbon* **50**, 2635-2640, (2012).

120 K. S. Kim, Y. Zhao, H. Jang, S. Y. Lee, J. M. Kim, K. S. Kim, J.-H. Ahn, P. Kim, J.-Y. Choi, B. H. Hong, Large-scale pattern growth of graphene films for stretchable transparent electrodes. *Nature* **457**, 706-710, (2009).

121 A. Reina, X. Jia, J. Ho, D. Nezich, H. Son, V. Bulovic, M. S. Dresselhaus, J. Kong, Large area, few-layer graphene films on arbitrary substrates by chemical vapor deposition. *Nano lett.* **9**, 30-35, (2009).

122 S. Bae, H. Kim, Y. Lee, X. Xu, J.-S. Park, Y. Zheng, J. Balakrishnan, T. Lei, H. R. Kim, Y. I. Song, Y.-J. Kim, K. S. Kim, B. O¨zyilmaz, J.-H. Ahn, B. H. Hong, S. Iijima, Roll-to-Roll Production of 30-Inch Graphene Films for Transparent Electrodes. *Nature nanotechnol.* **5**, 574-578, (2010).

123 D.-m. Sun, M. Y. Timmermans, Y. Tian, A. G. Nasibulin, E. I. Kauppinen, S. Kishimoto, T. Mizutani, Y. Ohno, Flexible high-performance carbon nanotube integrated circuits. *Nature nanotechnol.* **6**, 156-161, (2011).

124 J. D. Caldwell, T. J. Anderson, J. C. Culbertson, G. G. Jernigan, K. D. Hobart, F. J. Kub, M. J. Tadjer, J. L. Tedesco, J. K. Hite, M. A. Mastro, R. L. Myers-Ward, C. R. Eddy, Jr., P. M. Campbell, D. Kurt Gaskill, Technique for the dry transfer of epitaxial graphene onto. *ACS nano* **4**, 1108-1114, (2010).

125 L. Jiao, B. Fan, X. Xian, Z. Wu, J. Zhang, Z. Liu, Nanostructures with Poly(methyl methacrylate)-Mediated Nanotransfer. *J. Am. Chem. Soc.* **130**, 12612–12613, (2008).

126 J. Jiang, R. Saito, G. G. Samsonidze, S. G. Chou, A. Jorio, G. Dresselhaus, M. S. Dresselhaus, Electron-phonon matrix elements in single-wall carbon nanotubes. *Phys. Rev. B* **72**, 235408, (2005).

127 A. Jorio, R. Saito, J. H. Hafner, C. M. Lieber, M. Hunter, T. McClure, G. Dresselhaus, M. S. Dresselhaus, Structural (n,m) Determination of Isolated Single-Wall Carbon Nanotubes by Resonant Raman Scattering. *Phys. Rev. Lett.* **86**, 1118-1121, (2001).

128 A. Jorio, A. G. Souza Filho, G. Dresselhaus, M. S. Dresselhaus, A. K. Swan, M. S. U ¨ nlu¨, B. B. Goldberg, M. A. Pimenta, J. H. Hafner, C. M. Lieber, R. Saito, G-band resonant Raman study of 62 isolated single-wall carbon nanotubes. *Phys. Rev. B* **65**,155412 (2002).

129 R. Saito, A. Jorio, J. H. Hafner, C. M. Lieber, M. Hunter, T. McClure, G. Dresselhaus,

and M. S. Dresselhaus, Chirality-dependent G-band Raman intensity of carbon nanotubes. *Phys. Rev. B* **64**, 085312 (2001).

130 R. B. Weisman, S. M. Bachilo, Dependence of Optical Transition Energies on Structure for SWCNT in Aqueous Suspension: An Empirical Katuaura Plot. *Nano lett.* **3**, 1235-1238, (2003).

131 A. M. Rao, P. C. Eklund, Shunji Bandow, A. Thess, R. E. Smalley, Evidence for charge transfer in doped carbon nanotube bundles from Raman scattering, *Nature* **388**, 257-259, (1997).

132 D. K. Schroder, Semiconductor material and device characterization. John Wiley & Sons, Inc., Hoboken, NJ, 2006_ Chapter 6.

133 B. W. Reed, M. Sarikaya, TEM/EELS analysis of heat - treated carbon nanotubes: experimental techniques. *J. Electron Microscopy* **51**, S97-S105, (2002).

134 H. Wang, R. Coˆte´, G. Faubert, D. Guay, J. P. Dodelet, Effect of the pre-treatment of carbon black supports on the activity of Fe-based electrocatalysts for the reduction of oxygen. *J. Phys. Chem. B* **103**, 2042-2049, (1999).

Acknowledgements

It was exactly three years ago when I accepted the offer to join PhD program at Tokyo. As a fresh graduate I did not know what was in store for me, PhD seemed too big a decision, all I had was just a vague belief that things will turn out to be good. In all these years that belief did not get shattered, but gradually turned into reality, of course, with the help of numerous people that crossed my way during this course. This section is dedicated to them.

First and foremost I want to thank my PhD supervisor, Prof. Shigeo Maruyama. Working with him has been a tremendously rewarding experience. His insightfulness in grasp of researches helped me in taking on multiple works. He taught me how good experimental is done and helped to make device fun for me with his efforts, passion, and motivation. I also really appreciate all his contributions of time, ideas, patience, and funding to make my PhD experience. You have been a wonderful advisor.

I would like to thank the members in my PhD defense committee for their time and attention: Prof. Jean-Jacques Delaunay, Prof. Junichiro Shiomi, Prof. Kosuke Nagashio, Lecturer Shohei Chiashi, as well as Prof. Shigeo Maruyama. Their comments and suggestions have made significant improvements to this thesis.

How could I forget my lab colleagues (past and present) with whom I spent most of my time during PhD. The group has been a good advisor and collaborator as well as friendships. Dr. Shinya Aikawa (National Institute for Materials Science, Japan) and Dr. Pei Zhao (University, China), I will always miss our long discussions and many comments about researches and life in general in lab and clean room. I also have had great pleasure to work with Prof. Junichiro Shiomi, Lecturer Shohei Chiashi, Erik Einarsson (University at Buffalo, USA) Dr. James Cannon, Dr. Takuma Shiga, Dr. Theerapol Thurakitseree, Taiki Inoue and the numerous Ph.D candidate, master, undergraduate, and exchange students who have

come through the lab. I am indebted to Mr. Makoto Watanabe, the technical staff in Maruyama Lab, who dealt with all of my experimental purchases and financial supporting that were essential for the fulfillment of this thesis, and Ms. Maiko Terao, the secretary, who took care of most of my academic affairs and helped me finished the graduate procedures.

I want to thank my S.M. supervisor, Prof. Young Hee Lee (Sungkyunkwan University, Korea). He taught research and many things to me from master course. He is my role model.

I would also like to thank the collaborators I worked or got helped from, Prof. Kazuhito Tsukagoshi (National Institute for Materials Science, Japan), Dr. Min Ho Park (Sungkyunkwan University, Korea), and Prof. Cheol Woong Yang (Sungkyunkwan University, Korea). I wish to thank the generous and insightful discussions and suggestions from Dr. Cheol-Min Yang (Korea Institute of Science and Technology), Prof. Keun Soo Kim (Sejong University), Dr. Seung Yol Jeong (Korea Electrotechnology Research Institute, Korea), Dr. Hee Jin Jeong (Korea Electrotechnology Research Institute, Korea). I also would like to thank my friend, Prof. Ki Kang Kim (Dongguk University, Korea).

Lastly, I wish to thank my family members: Joongkwang Kim and Soodan Hwang, my parents, for providing a loving and supportive environment for me in Tokyo. To them I dedicate this thesis.

Publication list in PhD course

Journal papers

1. **Sungjin Kim**, Theerapol Thurakitseree, Shinya Aikawa, Taiki Inoue, Shohei Chiashi, and Shigeo Maruyama, 'Transport characteristics of nitrogen-induced horizontally aligned single-walled carbon nanotubes', to be submitted.
2. **Sungjin Kim**, Pei Zhao, Shinya Aikawa, Erik Einarsson, Shohei Chiashi, Junichiro Shiomi, and Shigeo Maruyama, 'Highly stable n-doped graphene field-effect transistors with polymer films', to be submitted.
3. Pei Zhao, Bo Hou, Xiao Chen, **Sungjin Kim**, Shohei Chiashi, Erik Einarsson, Shigeo Maruyama, 'Investigation of Non-Segregation Graphene Growth on Ni via Isotope Labeled Alcohol Catalytic Chemical Vapor Deposition', *Nanoscale*, **5**, 6530-6537, June. 2013.
4. Pei Zhao, Akihito Kumamoto, **Sungjin Kim**, Xiao Chen, Bo Hou, Shohei Chiashi, Erik Einarsson, Yuichi Ikuhara, and Shigeo Maruyama, 'Self-Limiting Chemical Vapor Deposition Growth of Monolayer Graphene from Ethanol', *J. Phys. Chem. C*, **117**, 10755-10763, Apr. 2013.
5. Kwanghyun Yoo, Yusuke Takei, **Sungjin Kim**, Shohei Chiashi, Shigeo Maruyama, Kiyoshi Matsumoto, Isao Shimoyama, 'Direct physical exfoliation of few-layer graphene from graphite grown on a nickel foil using polydimethylsiloxane with tunable elasticity and adhesion', *Nanotechnology*, **24**, 205302, Apr. 2013.

Conference Contributions

1. **S. Kim.** et al., 4th A3 Symposium on Emerging Materials: Nanomaterials for Energy and Electronics,
   November 2013, Jeju, Korea.

2. **S. Kim.** *et al.*, The 5th International conference on Recent Progress in Graphene Research,
   September 2013, Tokyo, Japan.
3. **S. Kim.** *et al.*, 2012 MRS fall meeting,
   November 2012, Boston, USA.
4. **S. Kim.** *et al.*, The 2nd International Symposium on Terahertz Nanosience,,
   July 2012, Okinawa,Japan.
5. **S. Kim.** *et al.*, International Symposium of Carbon Nanotube Nanoelectronics,
   June 2012, Nagoya, Japan.
6. **S. Kim.** *et al.*, International Microprocesses and Nanotechnology Conference,
   November 2011, Kyoto, Japan.
7. **S. Kim.** *et al.*, The 42nd Fullerenes-Nanotubes-Graphene General Symposiu,
   March 2012, Tokyo, Japan.